Development of the Readout Electronics for the Beam Loss Monitors of the LHC

Juni, 2002

Werner Friesenbichler

Eidesstattliche Erklärung

Titel der Diplomarbeit:

Development of the Readout Electronics for the Beam Loss Monitors of the LHC

Diplomarbeit

Eingereicht von:	Werner Friesenbichler
Vertiefung:	Mikro- und Feinwerktechnik
am	**Fachhochschul-Studiengang** **Präzisions-, System- und Informationstechnik**
Begutachter:	DI Helmut Frais-Kölbl
Wiener Neustadt, am:	Juni, 2002

Ich versichere,
dass ich die Diplomarbeit selbständig verfasst, andere als die angegebenen Quellen und Hilfsmittel nicht benutzt und mich auch sonst keiner unerlaubten Hilfe bedient habe und diese Diplomarbeit bisher weder im In- und Ausland in irgendeiner Form als Prüfungsarbeit vorgelegt habe.

Datum

Unterschrift

Kurzzusammenfassung:

Der Large Hadron Collider (LHC) des europäischen Laboratoriums für Teilchenphysik (CERN) wird der größte Teilchenbeschleuniger der Welt sein. Er benötigt eine große Anzahl von Einrichtungen für seinen Betrieb. Eine dieser Einrichtungen sind die Beam Loss Monitore, welche die Teilchenverluste messen. Sollten diese Verluste eine bestimmte Grenze überschreiten, muss der Strahl ausgekoppelt werden, ansonsten könnten die supraleitenden Magnete beschädigt werden. Zu diesem Zweck sind Ionisationskammern außerhalb des Kryostat installiert, um die Teilchenverluste in einen elektrischen Strom zu transformieren. Eine Eingangsstufe mit großem Messbereich wurde entwickelt, um diesen Strom zu messen. Die Schaltung besteht aus einem Strom-Frequenz Wandler, der nach dem Prinzip des Ladungsausgleichs arbeitet. Seine Ausgangsfrequenz wird mit Zählern ausgewertet und die Daten werden seriell vom Tunnel and die Oberfläche übertragen, wo letztlich die Auswertung vorgenommen wird. Die Datenübertragung leidet unter der langen Verkabelungsdistanz von bis zu 2 km. Die Verwendung von Manchester Code und Leitungsequalizern ermöglicht eine Datenrate von 2 Mbit/s über ein herkömmliches Twisted Pair Kabel. Die Probleme bei der Übertragung führten zu einer detaillierten Analyse von Leitungen im Frequenz- und Zeitbereich.

Schlagworte: Beam Loss Monitor, Strom-Frequenz Wandler, Übertragungsleitungen, Kabelequalizer, Datenübertragung

Abstract:

The Large Hadron Collider (LHC) of the European Laboratory for Particle Physics will be the largest particle accelerator in the world. It requires a large number of installations for its operation. One of these installations are the beam loss monitors which measure the particle losses. If these losses exceed a certain level, the beam must be extracted, otherwise the superconducting magnets could be damaged. For this reason, ionization chambers are installed outside the cryostat to transform the losses into an electric current. A wide dynamic range front end was developed to measure this current. The circuit consists of a current-to-frequency converter that works on the principle of balanced charge. Its output frequency is evaluated by counters and the data is serially transmitted from the tunnel to the surface, where the final data processing is performed. The data transmission suffers from the long cabling distance of up to 2 km. Using Manchester Code and line equalizers enables a data rate of 2 Mbit/s over a common twisted pair cable. This transmission problems lead to a detailed analysis of transmission lines in the frequency and time domain.

Keywords: Beam Loss Monitor, Current-to-Frequency Converter, Transmission Lines, Cable Equalizer, Data Transmission

Contents

1 Introduction 1

2 The Large Hadron Collider 3

- 2.1 Project Overview 3
- 2.2 Machine Specification 5
- 2.3 Machine Protection 7
- 2.4 Magnet Quench Process 7
- 2.5 Quench Levels 9

3 Beam Loss Monitors 10

- 3.1 Detector Location 10
- 3.2 The Ionization Chamber 11
  - 3.2.1 Calculation of the chamber signal amplitude 12
  - 3.2.2 Transient response of the chamber 13
- 3.3 Structure of the BLM Readout Chain 15

4 Analog Front End 17

- 4.1 Signal Specifications 17
- 4.2 Design Considerations 17
  - 4.2.1 Direct monitoring techniques 18
  - 4.2.2 Integrating techniques 21
- 4.3 Current-to-Frequency Converter 23
  - 4.3.1 Functional principle 23
  - 4.3.2 Circuit design 24
  - 4.3.3 Error calculation 36
- 4.4 Tests and Calibration 44

5 Data Transmission **49**

5.1 Data Transmission Cable 49

5.2 Transmission Line Theory 52

5.2.1 Skin effect 57

5.2.2 Dielectric loss 59

5.3 Transient Simulation of Lossy Transmission Lines 60

5.3.1 Analysis in the frequency domain 60

5.3.2 Analysis in the time domain 62

5.4 Signal Transmission Techniques 73

5.4.1 Data encoding and multiplexing 74

5.4.2 Line driver / receiver 79

5.4.3 Signal equalization 81

5.4.4 Synchronization 87

6 Summary **90**

Acknowledgements **92**

List of Abbreviations **93**

List of Figures **94**

List of Tables **97**

References **98**

A Schematics **100**

B Mathematica Files **106**

B.1 Calculation of line parameters 106

B.2 Transfer function approximation 107

B.3 Cable attenuation with dielectric loss 108

B.4 Calculation of the impulse / step response 110

B.5 Line equalizer 114

B.6 Calculation of a square wave / Manchester encoded signal 118

C GAL Files 122

C.1 Encoder 122

C.2 Synchronizer 124

1 Introduction

The urge for discovering the structure of matter and to explain our own origin is the business of many research centres all over the world. However, one of these centres impresses not only by its size but also because of the variety of discoveries, which have been made there in the last decades – the European Laboratory for Particle Physics, CERN[1]. The facility was funded in 1954 near Geneva, Switzerland and is run by 20 European member states. It constitutes the largest research centre for particle physics in the world. About 6500 scientists from 500 different universities use the equipment of CERN and all over the world there might be thousands of people who are in collaboration. One of the major tasks of CERN is the search for the structure of matter. The widely established Standard Model has been verified down to its very details but still lots of questions remain. The most famous actual project of CERN is the construction of the Large Hadron Collider (LHC). A particle accelerator with unprecedented energies, which will be installed in the tunnel of CERN's former Large Electron Positron Collider having a circumference of 27 km. The installation is scheduled to run in 2007.

In order to operate such a sophisticated machine, thousands of instruments are needed. This thesis describes the development of the readout electronics of one of these instruments – the beam loss monitors (BLM). First, a general introduction in the aim and the specifications of the LHC is given in chapter 2. The machine protection is an important point of the project. One critical source of error is the particle loss that can't be avoided. This loss could trigger a quench, i.e. it drives a superconducting magnet into normal conduction. In such a case, the quenched magnet has to be turned off immediately. The result is a long off-time of the LHC, since the magnet must be cooled down again to reach the superconducting state and a serious damage can't be excluded. Therefore, the particle losses must be observed continuously and the beam has to be dumped (= extracted safely) before the losses reach the quench level. This task is accomplished by the beam loss monitors as described in chapter 3. The monitors are formed by

---

[1] Conseil Européen pour la Recherche Nucléaire.

ionization chambers that produce an electric current equivalent to the particle loss. In order to evaluate the beam loss signal, the quench level equivalent chamber current must be determined. It is measured by an analog front end, which has to cover a dynamic range of nearly 140 dB. The data evaluation can't be done in the tunnel thus the measured loss signal must be transmitted to the surface, where the final data processing is performed. The thesis describes the development of the whole readout chain, which ends in a digital signal at the surface that is used for the final data evaluation. Chapter 4 deals with the development of the analog front end, which measures the chamber current. A current-to-frequency converter was designed to transform the chamber current into a proportional frequency. It is shown that this type of electronics provides excellent linearity over the desired dynamic range. The whole circuit design is presented.

The second big part of this thesis is concerned with data transmission. Because of radiation in the tunnel, the evaluation of the front end signal has to be performed in a surface building. This leads to long cabling distances of up to 2 km between the front end in the tunnel and the dump controller on the surface, which processes the data. Several discussions on the signal transmission over lossy cables were made and lead to a detailed treatment of this topic in chapter 5. After a short introduction in transmission line theory, the two main contributors to signal distortion – skin effect and dielectric loss – are examined thoroughly. The data will be transmitted in Manchester Code, which increases the maximum data rate and simplifies the error detection, too. Six channels are multiplexed to make the data transmission more economic. A unique frame alignment word marks the beginning of each frame, which contains the data of the beam loss channels. However, the long distance needs line equalizers to guarantee a reliable signal restoration. The results from the transient analysis of the cable were used to design the equalizer and to simulate its performance. The last topic is the synchronization of the data stream after the long cable to the local clock at the receiver. A counter algorithm was implemented in a GAL to produce a synchronized, Manchester encoded data stream, which is the input for the following dump controller. Finally, this controller will evaluate the losses and decide whether the beam must be dumped or not.

2 The Large Hadron Collider

2.1 Project Overview

Since the beginning of particle physics many models have been formed to explain the structure of matter. Nowadays, the so called Standard Model has been established which uses four forces to explain the interactions between particles. These forces are

- *gravity*, which explains e.g. the force between macroscopic objects,
- the *electromagnetic force*, which keeps the electrons on their track around the atomic nucleus,
- the *weak force*, which is responsible for the radioactive β-radiation and
- the *strong force*, which keeps the atomic nucleus together.

The paradox of all these forces is, that the first found gravity force by Isaac Newton personates one of the big mysteries and uncertainties that remain. The Standard Model assigns every force a particle which is the carrier of the force. The *photon* is responsible for the transmission of the electromagnetic force, the *W* and *Z boson* carry the weak force and the *gluon* transfers the strong force. The gravity force, however, doesn't really fit into this model. According the quantum field theory, a carrying particle named *graviton* has been created but its existence couldn't be proved yet. Another important question that couldn't be answered yet is: "Why do elementary particles have mass, and why are their masses different?". It is commonly known, that protons are almost 2000 times heavier than electrons but the reason for that mass difference is not obvious. Much more impressive is the fact that photons have no mass while W bosons, for example, have a mass of 80 GeV/c^2.[2]

To explain the different masses of particles, a theory called 'Higgs mechanism' was formed. According to that theory, all particles interact with a Higgs field. The stronger the interaction, the higher the mass of the particle. In addition, the Higgs field is related to a new particle – the Higgs boson. The present theory assumes that the Higgs boson must have a mass of more

---

[2] According Einstein's famous equation $E = mc^2$, mass can be also expressed in terms of equivalent energy.

than 100 GeV/c^2 and less than 200 GeV/c^2. However, the present particle accelerators could not provide sufficient energy to detect it [Har-00].

In order to perform further examinations on the Standard Model and to detect the Higgs boson, if it exists, a new particle accelerator with unprecedented energies is currently built at CERN – the Large Hadron Collider (LHC)[3]. It will collide two counter-rotating proton beams with an energy of 7 TeV each at four intersection points, called ATLAS, ALICE, CMS and LHC-B. In addition, the LHC will also collide heavy Pb-ion with a center-of-mass energy of more than 1000 TeV. The installation is hosted in the 27 km circumference tunnel of CERN's former Large Electron Positron Collider (LEP). Figure 2.1 shows the layout of the LHC. The beams are injected left and right of the ATLAS experiment. The location of the dump, cleaning and acceleration equipment (RF) is also indicated at the perimeter.

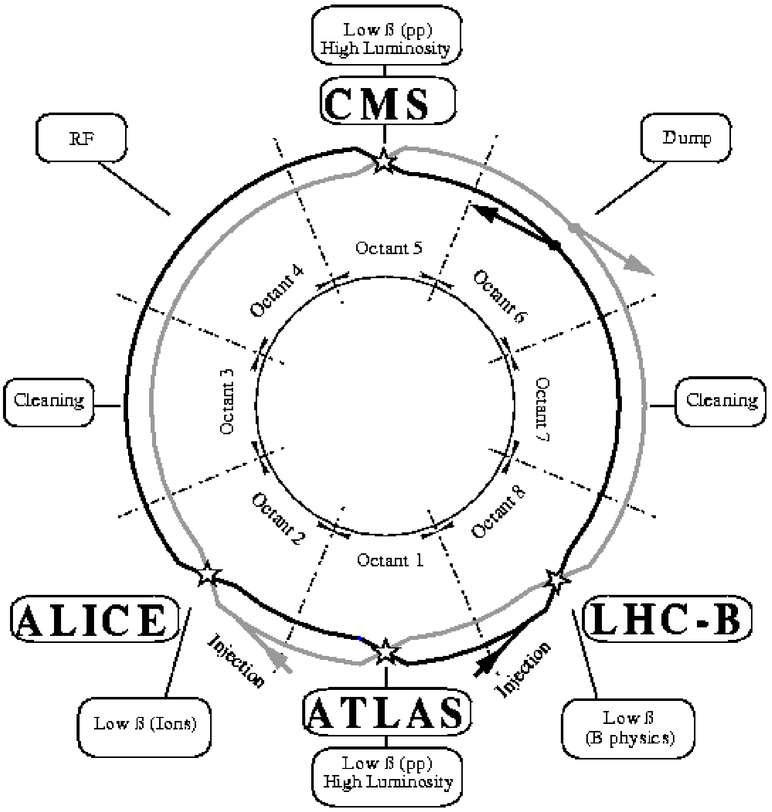

Fig. 2.1 Schematic view of the two beams of the LHC.

To generate these high beam energies, superconducting magnets with flux densities up to 8.4 T are used to keep the beams on their track. The magnets are manufactured out of classical NbTi superconductors and are cooled down to 1.9 K with superfluid helium to permit the

---

[3] All information concerning the LHC, as not otherwise cited, was taken from [LHC-95].

operation current of 11.5 kA (dipole magnet). In addition to the beam bending dipole magnets, quadrupole magnets that focus the beam constitute the main part of the LHC magnet system. Moreover, sextupole, octupole and decapole magnets are deployed to sustain orbit stability. The total number of magnets exceeds 8000. The cross-section of an LHC dipole magnet is illustrated in Fig. 2.2. The left picture shows the beam tube, which is surrounded of the crescent-shaped coil and the collars. In the right picture, a detailed view of the coil assembly is presented. This construction is typical for a superconducting magnet.

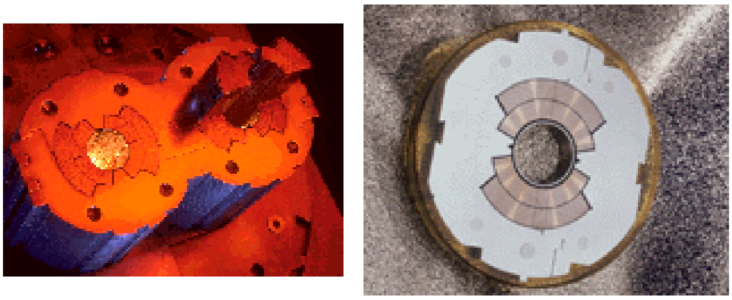

Fig. 2.2 Cross-section of an LHC dipolemagnet. Left: The two vacuum tubes surrounded by the coils and the collars. Right: Detailed view of the vacuum coil and the collar assembly.

2.2 Machine Specifications

The relevant specifications of the LHC for the beam loss system are summarized in Table 2.1. As stated in the previous chapter, the LHC will provide proton-proton collisions with a beam energy of 7 TeV each. In order to obtain this energy, the particle beam has to be accelerated from zero in several stages whereas the acceleration process involves almost all CERN accelerators (Linac, PSB, PS, SPS and LHC), see Figure 2.3.

Table 2.1 LHC parameters.

Parameter	**Value**
Energy	7.0 TeV
Dipole field	8.4 T
Injection energy	450 GeV
Bunch spacing	25 ns
Bunch length	0.3 ns
Particles per bunch	10^{11}
Stored beam energy	334 MJ
Beam life time	22 h

After running through the whole chain, the beam is finally injected from the SPS into the LHC with an energy of 450 GeV. The energy of the proton beams is increased by the field of the beam magnets. Simultaneously, radio-frequency cavities accelerate the protons, to keep the beam on a stable orbit. This process, which is called ramping, lasts about 20 minutes. The ramping affects the beam loss system because the different beam energies, beginning from 450 GeV up to 7 TeV, have to be treated differently (see section 2.5).

Another important issue is the structure of the beam itself. The beam particles are distributed around the ring in 2835 bunches with 10^{11} protons each and a length of $t = 0.3$ ns. The nominal time between the bunches is 25 ns with one exception: The time space after the last bunch is 3 μs. This gap in the beam timing is important for the beam dump action (see section 2.3). The revolution of the particles takes 89 μs ($\approx \frac{27\text{ km}}{3\times10^8\text{ m/s}}$).

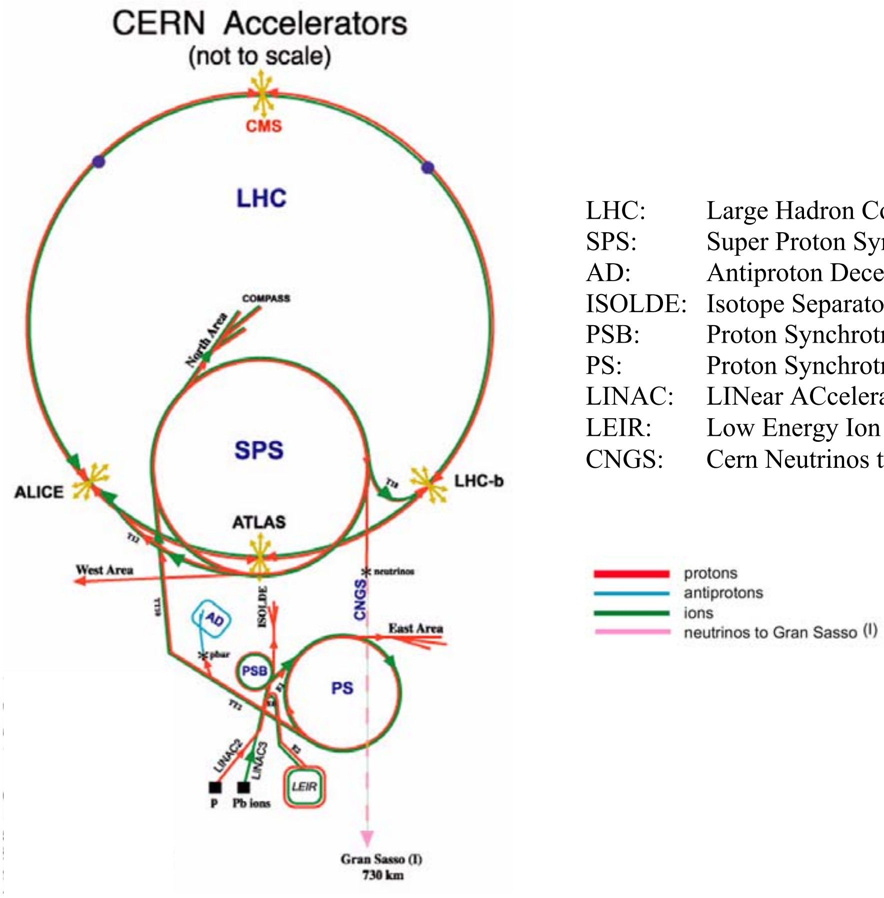

LHC:	Large Hadron Collider
SPS:	Super Proton Synchrotron
AD:	Antiproton Decelerator
ISOLDE:	Isotope Separator OnLine DEvice
PSB:	Proton Synchrotron Booster
PS:	Proton Synchrotron
LINAC:	LINear ACcelerator
LEIR:	Low Energy Ion Ring
CNGS:	Cern Neutrinos to Gran Sasso

Fig. 2.3 Overview of CERN's accelerator complex.

2.3 Machine Protection

The LHC is an accelerator which bursts one's bonds in terms of complexity as well as costs. To avoid any damage and to maximize the operation time is therefore the main goal.

The operation of the LHC requires a large variety of instrumentation for the circulation of the beams, as well as for the control and the protection of the accelerator. Therefore, a machine protection system has been developed to minimize the risk of serious damage. It contains two major interlock systems [Sch-01]:

- Powering Interlock system, which permits the powering of the magnet system and enables a safe power dissipation in case of failure.
- Beam Interlock system, which allows the beam to be injected and requests a dump if an unsafe condition arises.

These systems comprise several subsystems, such as quench protection, beam dump system, beam loss measurement, collimation system, access control, etc. The beam dump system should be briefly introduced because its properties lead to some restrictions for the beam loss system. As already noted, the beams have to be safely extracted in the case of failure but also if the luminosity[4] has degraded. This extraction is called dump (see Fig. 2.1). If a dump is requested, a kicker magnet steers the beam out of the accelerator ring to the dump block (3 x 3 x 14 m), which consists of a core of graphite that is surrounded by aluminium and iron. An important fact is the trigger of the kicker magnet. To avoid a spread-out of the beam particles due to the magnet's finite rise time, the 3 μs bunch gap in the beam structure is used. This leads to a remarkable point: Since the kicker magnets have to be synchronized to this gap, the beam can only be dumped exactly during this particular time. Therefore, the dump requesting system need only to have single turn resolution, affecting the design considerations of the readout electronics (see section 4.3.2).

This thesis focuses on the beam loss system and its technical realization. The main reason to implement such a system is the sensitivity of the superconducting magnets to any particle loss.

2.4 Magnet Quench Process

One possible malfunction emerges when a superconducting magnet becomes normal conducting, which is called *quench*. The reason for a quench is heat deposition in the superconducting magnet, which increases the coil temperature over a critical value. Heat can be deposited in the

---

[4] Accelerator Physics term which describes the probality of particle collisions in accelerators with colliding beams. It is typically stated in cm^{-2} s^{-1}.

coil of a magnet if beam particles leave their nominal orbit and hit the vacuum chamber wall of the beam tube[5]. This proton impact initiates a particle shower that is partially stopped in the windings of the superconducting coil. The result is a local increase in temperature. Several reasons for a particle loss can be found, such as

- beam-gas collisions between the beam protons and residual gas atoms,
- proton-proton collisions mainly at the four interaction points and
- particle losses due to machine imperfections.

Most of the particle losses are captured by blocks of solid copper, which are called collimators and absorbers, respectively. These collimators are moved towards the beam and capture any particles that are leaving the nominal orbit. Unfortunately, not all particle losses can be absorbed by collimators, especially lost particles due to beam-gas collisions touch the vacuum chamber and contribute to a temperature increase.

The magnets of the LHC are grouped together in eight sectors. All magnets of a sector are connected in series, thus if a magnet quenches the electromagnetic energy of the whole sector will be dissipated in the quenched magnet and destroying it. To protect the magnets, a quench protection based on the so called ”cold diode” concept has been implemented where only the energy of the quenched magnet itself will be dissipated as heat internally. If a quench occurs, the coil of a quenched magnet is bypassed with a diode and heaters are fired to warm up the whole coil uniformly. This drives a large volume of the quenched magnet normal conducting, which leads to a uniform energy dissipation and limits the maximum temperature rise as well as maximum internal voltages. Furthermore, high-energy dump resistors are switched in series to de-excite the remaining unquenched magnets and to prevent the quench from spreading to other magnets. In order to limit the voltage due to the large inductance of the magnets, this de-excitation can last up to 100 s for the large dipole magnets.

Although the quench protection system avoids major accidents, a quench leads to a long down time of at least 7 h. In addition, the risk of a magnet damage can’t be eliminated completely. In such a case, the LHC would be down for about four weeks [Sch-01]. Therefore, the particle losses have to be observed and the beam has to be dumped before a quench will occur. So monitors are installed outside the magnets to measure the protons that leave the nominal orbit.

---

[5] Beyond the energy release in the magnets due to beam losses, a quench can also be triggered by other events, e.g. conductor motions, electrical disturbances or hysteresis loss [Sie-01].

2.5 Quench Levels

In order to determine the quench levels of the LHC several investigations have been made [Jea-01]. Figure 2.4 shows the different quench levels at injection energy (450 GeV) and top energy (7 TeV), indicated in units of protons/m/s as function of the duration of the impact. The thermal conductivity of the surrounding helium flow determines the maximum loss rate at long time intervals. At short time intervals, the heat reserve of the cables, as well as the heat flow between the superconducting cables and the helium, tolerates much higher loss rates. The heat reserve of the helium determines the quench levels at intermediate time scales. As illustrated in the diagram, the proton loss rate extends over a range of six decades from 10^7 to 10^{13} protons/m/s and a time scale from 0.1 ms to 1000 s. The uncertainty is considered to be 50% [Gsch-01].

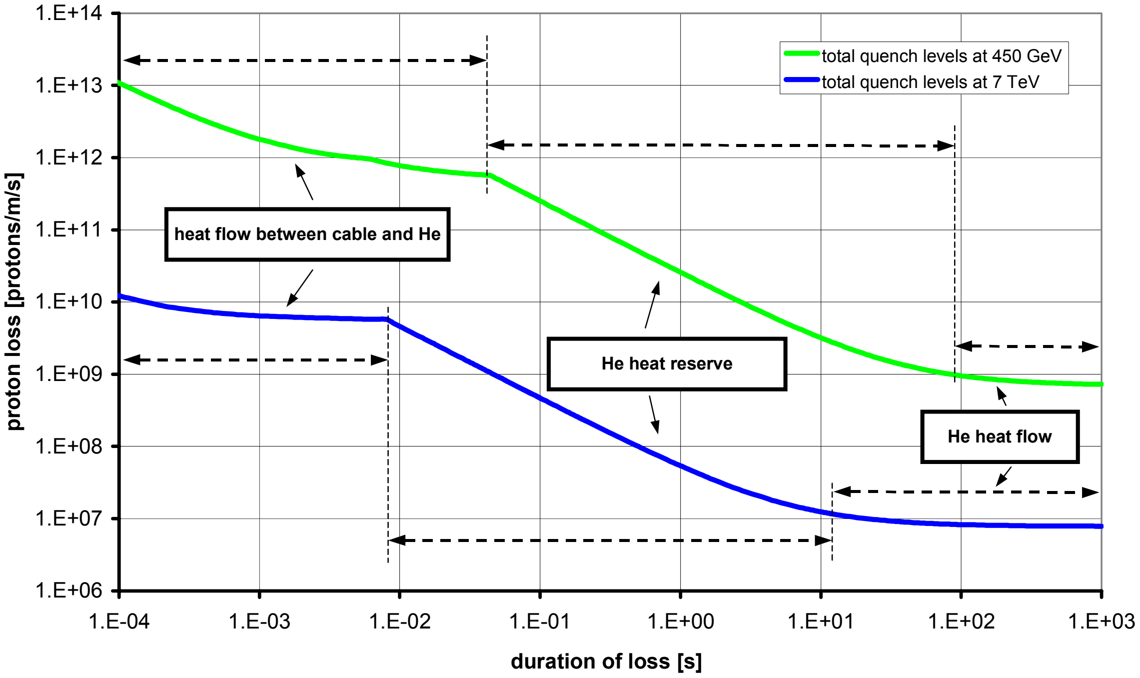

Fig. 2.4 Different quench levels for 450 GeV and 7 TeV [Gsch-01].

This quench levels could lead to severe malfunctions and destroy the magnets. Therefore, the beam must be dumped if the losses exceed 50% of the quench level [Jea-01].

3 Beam Loss Monitors

The risk of a quench or damage, makes the observation of the particle losses inescapable. In order to measure these losses, beam loss monitors are installed. Several studies and measurements on different types of beam loss monitors have been made [Bos-97], [Bos-98]. Finally, the ionization chamber remains of all the considered types [Gsch-01].

3.1 Detector Location

To detect the beam loss outside the cryostat, the created particle shower has to be calculated. In addition to the shower process, the different geometries and magnetic field configurations have to be considered. The aim of these computations is to determine the required number of beam loss monitors as well as their proper location. The placement of the beam loss monitors around the magnets is presented in Fig. 3.1. The top view shows a quadrupole (MQP) in the center and two adjacent dipoles (MD). The intended locations of the monitors are marked with the red points. Thus six monitors (three for each beam) outside the cryostat of the quadrupole magnets in the arc cells are needed to diagnose the expected beam loss completely [Gsch-01]. The total number of beam loss monitors is about 3000 [Jea-01].

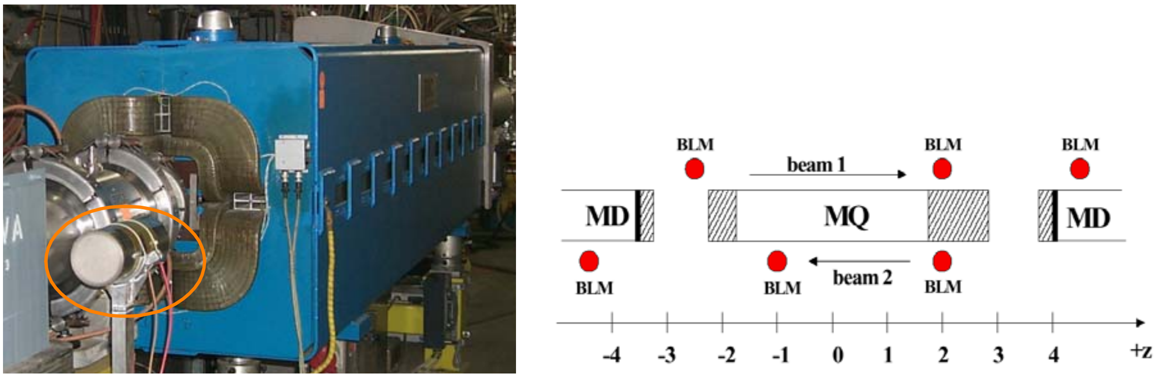

Fig. 3.1 BLM location at the quadrupoles. Left: Picture of the ionization chamber mounted in the SPS (pre-accelerator of the LHC) Right: Top view of the considered chamber location at the quadrupoles (MQ) and dipoles (MD), respectively.

Since the beam loss monitors are installed outside the cryostat, the primary beam loss must be calculated from the shower particles traversing the ionization chamber. The unit which is used to express the actual particle losses is the averaged number of expected shower particles per lost beam proton and cm^2, which is referred to as minimum ionizing particles (MIPs)[6]. Because the MIPs/p/cm^2 do not only depend on the beam energy but also on the monitor location as well as magnet configuration, a minium and a maximum value for the MIPs/p/cm^2 is specified. These numbers are needed to calculate the output signal of the ionization chamber (see section 3.2.1). Table 3.1 lists the expected shower particle density at injection and top energy.

Table 3.1 Simulated shower particles per lost proton and cm^2

	MIPs/p/cm^2	
Beam energy	Min	Max
450 GeV	$5{\cdot}10^{-4}$	$3{\cdot}10^{-3}$
7 TeV	$8{\cdot}10^{-3}$	$4{\cdot}10^{-2}$

3.2 The Ionization Chamber

The ionization chamber is the signal source for the beam loss electronics. It converts the particle shower caused by mislead protons into an electric current. The amplitude is proportional to the loss rate. As shown in the left part of Fig. 3.2, the chamber consists of a metal cylinder that is filled with N_2. The right part illustrates the structure inside the cylinder. Several metal plates connected in parallel where the distance between each plate is about 6 mm. A high electric voltage of 800 V is applied to the plates. The parallel connection increases the total output current but also the capacity, which plays a certain role in the performance of the circuit.

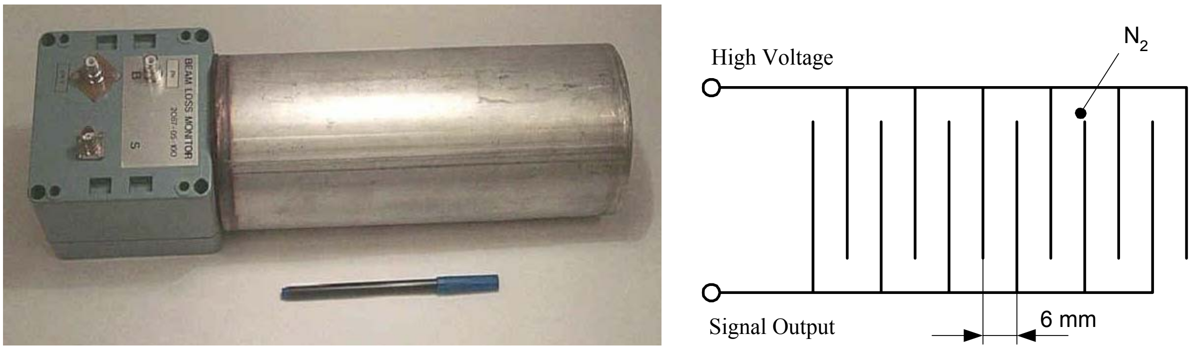

Fig. 3.2 Picture of an SPS-type ionization chamber (left) and schematic structure inside the cylinder (right).

Figure 3.3 shows the electrical connection of the chamber including the preamplifier of the front

---

[6] The MIP specifies the minimum energy that a particle releases moving in a certain medium.

end electronics. The bias voltage is applied via an RC-network ($R = 10$ MΩ, $C = 0.15$ μF) that protects the high voltage power supply against short circuits and ensures a stable bias voltage. Shower particles generate electron/ion pairs that result in an electric current at the output terminals, see next section.

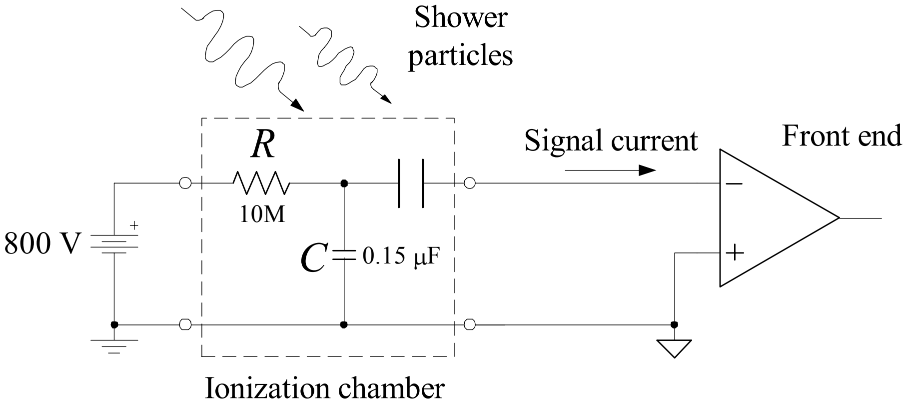

Fig. 3.3 Electrical connection of the ionization chamber.

3.2.1 Calculation of the chamber signal amplitude

The function of the chamber is based on the principle of ionization. If a particle crosses the space between two plates, it generates – depending mainly on the gas composition and gas pressure – electron-ion pairs. For N_2 at normal pressure the about 56 charges are generated per cm [Gru-93]. Due to the high voltage between the plates these charges are separated. The negative charged electron is accelerated towards the positive plate while the positive charged N_2 ion is attracted by the negative one. This charge separation results in an electric current that can be measured at the outside connectors. The amplitude of this current depends on several facts, such as

- the number of incoming particles,
- the volume of the chamber,
- the length of the particle trace in between the electrodes,
- the gas composition and
- the gas pressure.

A larger number of intruding particles generates more electron-ion pairs and thus increases the current. On the other side, the larger the volume, the more electron-ion pairs are generated on the particle's way through the chamber. In contrast, the bias voltage doesn't have a significant influence on the amplitude. Another important fact, which has to be taken into account, is the drift velocity of the two different charges.

Electrons have a high drift velocity, while ions have a much lower one. This leads to a fast response time of the chamber signal due to the fast electrons and a slow decaying tail due to the ions (see section 3.2.2) [Gru-93]. For the first investigation, an existing SPS chamber was used. This chamber has a surface of 30 cm^2 and a length of 30 cm. It is biased with 800 V and filled with N_2. According to [Gsch-01], one MIP produces 2000 electron/ion pairs. The signal amplitude of the ionization chamber can be calculated by

$$I_c = p \cdot MIPs \cdot S \cdot n \cdot e \tag{3.1}$$

where I_c is the chamber current, p the proton losses/s, *MIPs* the shower particles per proton and cm^2, S the chamber surface, $n = 2000$ the number of electron-ion pairs per MIP and $e = 1.6 \cdot 10^{-19}$ C the elementary charge.

With Eq. 3.1, the quench levels can now be expressed in ampere instead of protons/s to get a more handy description of the signals which have to be measured. Figure 3.4 shows the quench level equivalent chamber current. The duration of loss is marked on the horizontal and the chamber current is indicated on the vertical axis. One will notice four curves, which mark the maximum and minimum quench level at 450 GeV and 7 TeV. This comes from the different number of ionizing particles as stated in Table 3.1, which depends on the location of the magnet and its configuration. The one turn time is indicated as well as the maximum and minimum quench level. Hence the dynamic range lies between 600 pA for the minimum loss at 7 TeV and 300 μA for the maximum loss at 450 GeV. The last number emerges from the fact that the beam losses needn't be acquired faster than one turn.

3.2.2 Transient response of the chamber

The response time of the ionization chamber has a big influence on the design considerations for the following front end circuit. Figure 3.5 shows the setup for the measurement of the transient response time. The chamber was placed in the SPS and an LHC-type beam was shot on it to obtain a realistic measurement environment. To avoid the noise of preamplifiers, the chamber output was directly connected to the 50 Ω input of the scope. This low impedance connection also prevents the chamber capacity C_c from being charged and limiting the rise time.

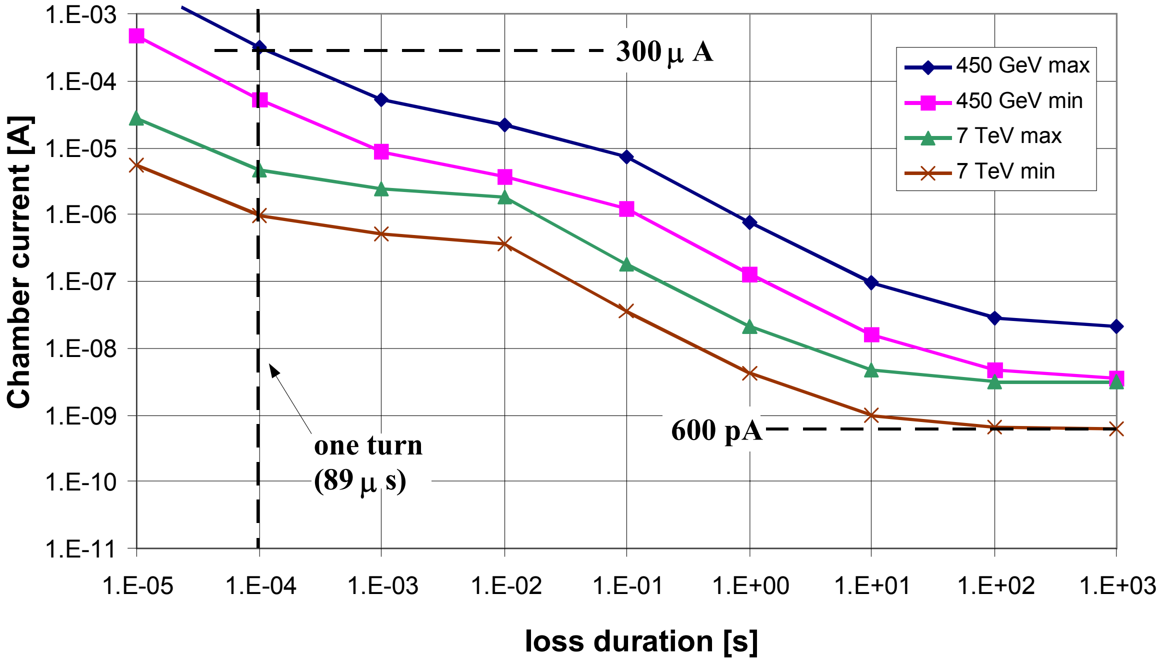

Fig. 3.4 Quench level equivalent chamber current at 450 GeV and 7 TeV as a function of the loss duration.

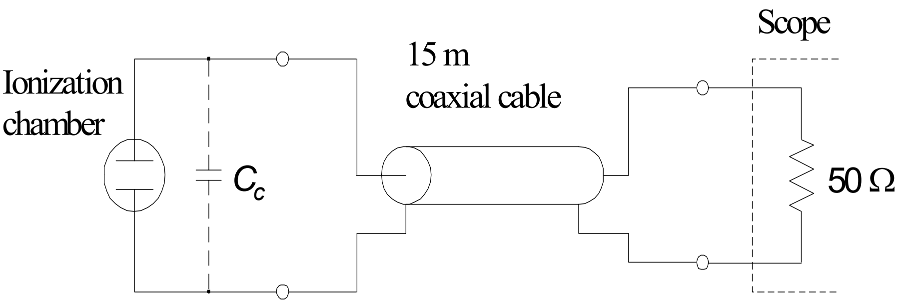

Fig. 3.5 Circuit for the transient response measurement of the ionization chamber.

The measured chamber response is presented in Fig. 3.6. According to the previous section, the charge separation shows two different effects with regard to the transient response of the chamber signal. The electrons, with their high drift velocity ($\sim$ 5 cm/μs), enable a fast rise time while the slower N_2 ions lead to a slow decaying tail as shown in Fig. 3.6 a). To measure the steep rise time, Fig. 3.6 b) magnifies this region and shows the chamber output signal compared to the beam intensity signal. This intensity measurement is done by observing the signal of the beam coupler, an installation that enables a real-time observation of the beam in the SPS. The picture shows no difference between the chamber response and the beam structure in time (except a small delay). Thus, the rise time of the ionization chamber was assumed to be less than 1 μs. In consequence, this fast rise time requires a cable termination, otherwise the fast edge would lead to reflections on the cable between the ionization chamber and the front end.

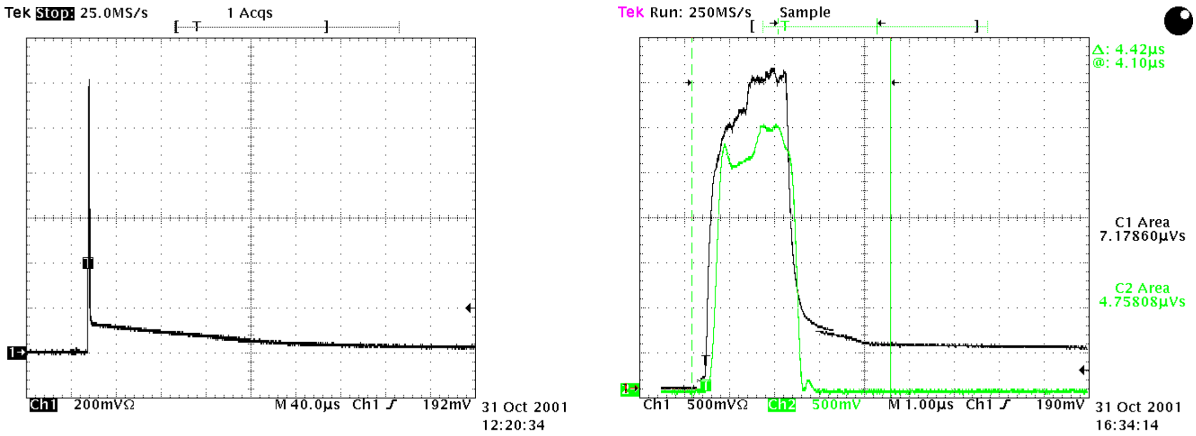

a) b)

Fig. 3.6 Measurements of the ionization chamber current versus time. The chamber is located in the SPS. a) The measurement duration of 400 μs emphasizes the fast electron signal (large peak) compared to the slow ion signal (long tail). b) Zoom at the electron signal (black) compared with the beam intensity signal.

3.3 Structure of the BLM Readout Chain

The intended BLM readout chain is illustrated in Fig. 3.7. As discussed in the previous sections, the ionization chamber delivers an electric current, which is proportional to the particle loss rate. The first evaluation of this signal is done by the analog front end. Due to radiation exposure in the accelerator tunnel, the cable length between the chamber and the front end can vary between several meters in the arcs of the tunnel, and up to 400 m in the straight sections. Moreover, up to 100 front end channels are installed on VME boards in a common rack. The increased radiation load in the tunnel necessitates a simple and robust design of the front end circuitry.

The final evaluation and the dump decision is made by the dump controller, which is installed in a crate located in a surface building. To optimize the design, each octant of the LHC circumference (Fig. 2.1) has its own crate in the center, where all dump controllers for the octant are installed. Thus the maximum cable length is about one half of an octant. Dividing the 27 km circumference by 16 and adding some hundred meters between the tunnel and the surface leads to a maximum cable length of up to 2 km (at special locations even 2.5 km) between the front ends at the far end of the octant and the dump controller. The nearest installations can be served with some hundred meters of cable. The dump controller itself calculates the beam losses for different loss durations and compares them with the appropriate treshold values. A warning or beam dump signal is generated if the tresholds are exceeded.

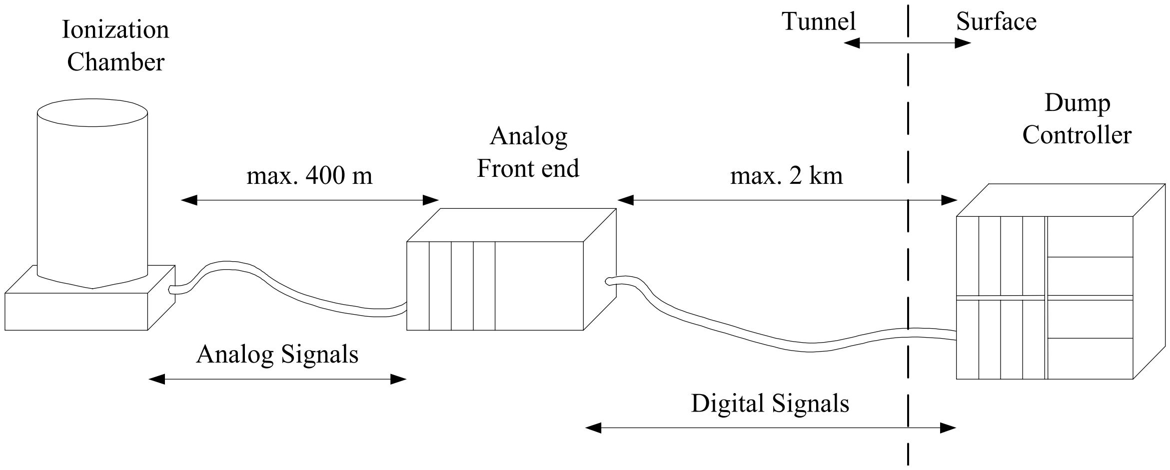

Fig. 3.7 Schematic of the beam loss monitor readout chain.

4 Analog Front End

4.1 Signal Specification

The requirements for the front end electronics have been derived in the previous chapter. As indicated in Fig. 3.4, the quench levels are varying between 600 pA and 300 μA. To ensure high sensitivity at low losses, the dynamic range must be extended at least one order of magnitude from 600 pA down to 60 pA. Thus the lower limit was set to 50 pA, which results in a dynamic range of 136 dB.

It is also shown that the loss duration has an impact on the quench levels. The integrated loss rate has to be acquired in an interval between 89 μs and 20 s. The minimum time limit is given by the fastest beam dump possibility after one revolution (= 89 μs) and the longest interval is set by the temperature measurement system of the He of the magnets. Simulation studies revealed that a quench could be predicted within an accuracy of ±50%. Consequently, the maximum allowable error of the readout electronics was set to ±10%. Table 4.1 summarizes the front end specifications.

Table 4.1 Front end specifiactions.

Parameter	Value
Input current	50 pA - 300 μA
Signal-to-noise ratio (SNR)	At least 6 dB
Acquisition rate	Min. each turn (= 89 μs), depending on the loss rate
Output signal	Not specified
Accuracy	±10%

4.2 Design Considerations

The usage of the ionization chamber leads to the measurement of a particle loss rate equivalent electric current. Several design considerations to acquire this current have been made.

Figure 4.1 shows an overview of the different methods that have been discussed. These measurement principles and the most suitable method for the beam loss system are discussed in the following section.

4.2.1 Direct monitoring techniques

These circuits provide an output signal that is proportional to the input current. A transimpedance amplifier, for example, transforms the input current into a proportional voltage. The output voltage can be sampled with an ADC at any desired frequency, which determines the evaluation time of the particle loss rate. Finally, the acquired loss rates are integrated numerically in a microcontroller or a DSP to determine the particle losses over time. Of course, direct monitoring techniques entail some drawbacks. The most significant point is the poor dynamic range that is directly related to the linear dependence of the output signal. It is not possible to achieve a dynamic range of more than approximately 60 dB without introducing large errors. Thus several gain stages have to be incorporated. Two circuits were tested that use two gain stages to provide more dynamic range:

1. The cascaded amplifier uses a transimpedance amplifier at the front end and a second high gain stage if further amplification is needed.
2. The switched gain transimpedance amplifier has two feedback paths that are automatically changed in dependence of the input signal amplitude.

Figure 4.2 a) shows a cascaded amplifier. At high chamber currents, the output signal of the transimpedance stage A_1 is appropriate to be digitized directly with an ADC that has sufficient resolution – at least 12 Bit. In the case of low losses, the output signal of the chamber is in the pA range and can't be sampled directly. Thus it has to be further amplified by the second stage A_2. This stage has a high gain of 1000. To decide which output signal will be evaluated, from the first or second stage, a comparator controls an analog multiplexer. The circuitry showed a simple implementation and stable operation conditions over a dynamic range of 140 dB. However, it has two major disadvantages.

1. The high gain of A_2 does not only amplify the signal but also the noise of the first stage. At small input signals this noise is too large. Therefore, a lowpass has to be switched at the output of A_2 that suppresses the noise but also reduces the signal bandwidth.
2. Beside the noise, the offset voltage of A_1 is amplified, too. This stage uses a JFET op amp, which generally has a low input bias current but a higher offset voltage. Hence the output offset voltage of A_2 can reach several hundred mV.

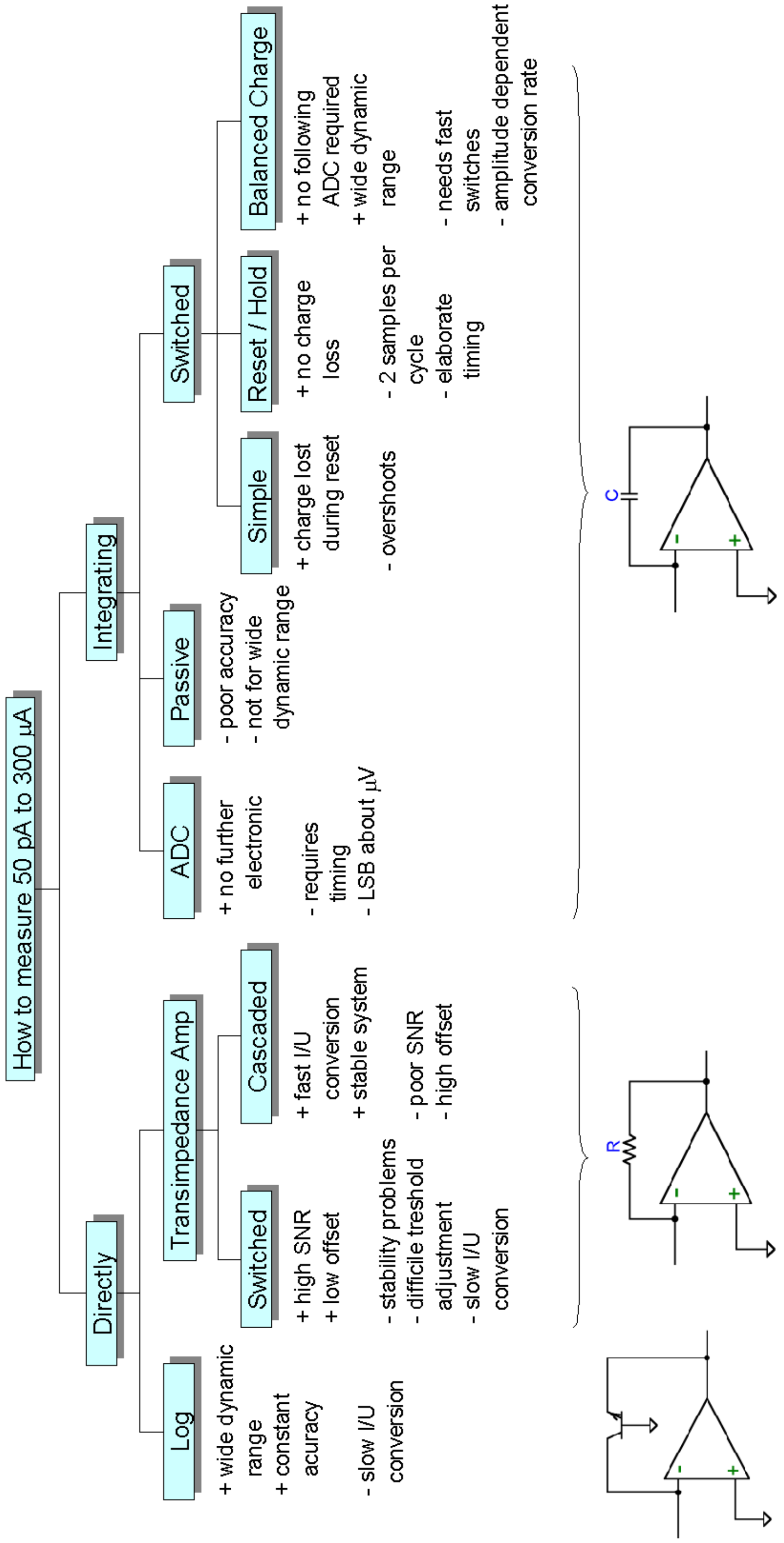

Fig. 4.1 Overview of the different techniques to measure electric current. The methods are divided into direct and integrating techniques.

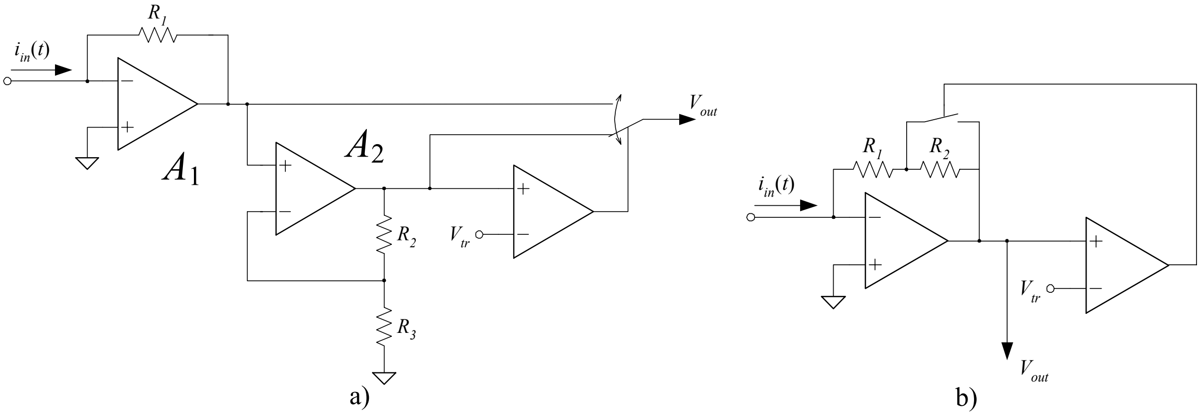

Fig. 4.2 Direct Monitoring Techniques: a) Cascaded amplifier. b) Switched gain transimpedance amplifier.

This drawbacks make the cascaded amplifier not usable for the beam loss front end. Another solution is the switched gain amplifier in Fig. 4.2 b). In this circuit, the feedback resistor is changed dependent on the actual chamber current. Since the output impedance of the ionization chamber is assumed to be infinity (or at least in the range of several GΩ), the DC voltage gain is one. Hence the output offset voltage can be neglected. The only error term arises from the input bias current that leads to a voltage drop over the feedback resistor. The gain is changed by observing the output signal with a comparator. If the input current exceeds a treshold, R_2 (high resistance) is shortened by a FET switch before the op amp saturates. Then the feedback resistance is determined only by R_1 (small resistance). At low input currents, the switch is opened again, so the feedback resistor equals the sum of R_1 and R_2. To avoid instability and oscillation, the comparator needs a certain hysteresis.

Unfortunately, this circuit suffers from input capacitance (chamber, cable), which has been neglected so far. This capacitance increases the gain at high frequencies and leads to overshoots when the gain is switched. The overshoots are critical, since they can retrigger the comparator and lead to oscillation. Thus capacitors are switched in parallel to R_1 and R_2, which limit the high-frequency gain but also reduce the signal bandwidth. However, even with this measures it was not possible to extend the dynamic range beyond 120 dB. In addition, both circuits in Fig. 4.2 are blind during the switching action – which is not advisable for an important security system as the beam loss monitors.

Another circuitry that is able to provide a gain of more than 120 dB would be a logarithmic amplifier. Several chips have been tested but none of them showed satisfying performance. The main problem with logarithmic amplifiers is their limited bandwidth, which depends on the amplitude of the input signal. A logarithmic amplifier uses the exponential relation between the collector current I_c and the base emitter voltage V_{BE} of a bipolar transistor. However, the dynamic impedance of a bipolar transistor reads $\frac{1}{g_m} = \frac{V_T}{I_{C0}}$, with the transconductance $g_m = \frac{\partial I_c}{\partial V_{BE}}$, the thermal voltage V_T and the collector bias current I_{C0}. At small collector currents (= signal currents), $\frac{1}{g_m}$ becomes larger and increases the gain. This reduces the bandwidth of the op amp if a constant gain-bandwidth product is assumed. Tests revealed that the bandwidth is too small to detect the particle losses accurately.

Since the front end will be installed in the tunnel, reliability, simplicity and radiation hardness have to be taken into account. Moreover, the data transmission between the front end location and the dump controller represents another challenge – not only in terms of feasibility but also in terms of costs. In addition, the large number of more than 3000 beam loss channels [Jea-01] entails a low cost, non-adjustable design, which finally lead to another solution.

4.2.2 Integrating techniques

Compared to direct monitoring this approach provides only the average loss rate, but offers unique properties in terms of dynamic range and SNR. The most simple way to realize such a circuit would be an ADC that offers a high dynamic range. Several components, especially for audio applications, have been found but none offered a sufficient low input current. The passive integrator was only added to complete the description in Fig. 4.1. It is not able to form a precise integrator for such a high dynamic range as for the beam loss system.

The switched integrator in Fig. 4.3 a) is a widely used circuit to measure small currents. An electric current charges the feedback capacitor of an op amp, so the output voltage equals the integral of the current over time. However, the output voltage is subjected to the same restrictions as with direct current monitoring. Thus only a dynamic range of 60 dB would be reached. This range can be extended, if a certain treshold voltage is introduced. If the output voltage hits the treshold within the time interval, the integrator will be reset. At the end of the integration interval, the actual output voltage is sampled as before, but now the number of reset actions within the interval are added to that value. As long as the reset time is much shorter than the integration time, where the voltage decreases from zero to the treshold V_{th}, the introduced error can be neglected. This procedure is shown in Fig. 4.3 a). The prototype circuit showed a good performance up to 100 dB. Above, the reset time lead to large errors of more than 40%.

The circuit in Fig. 4.3 b) improves the reset by using an additional hold switch at the op amp input. With this modification, no charge is lost during the reset. Before the integrator is reset,

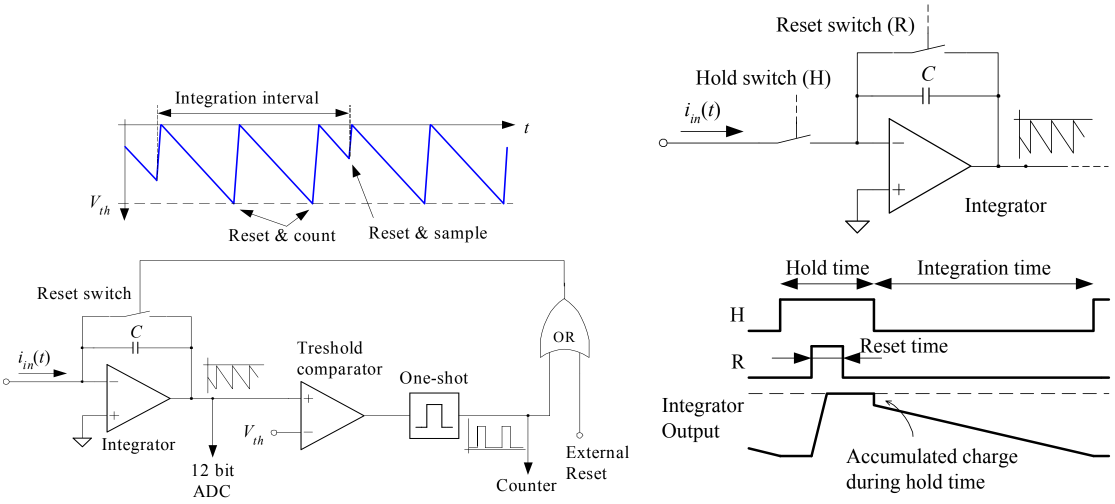

a) b)

Fig. 4.3 Principle of a switched integrator: a) Only with a reset switch, b) Improved circuit with additional hold switch.

the hold switch is opened. The integrator output is sampled by an ADC. During the hold mode, the signal current charges the input capacitance (chamber plus cable capacitance). After the reset is completed, the integrator output is sampled again and the hold switch is opened. The accumulated charge is transferred to the integration capacitor, resulting in a step voltage that corresponds the accumulated charge divided by the value of the integration capacitor. However, the disadvantage of this circuit is a more sophisticated timing and the need for two samples per integration period – which eliminates the offset voltage and charge injection error of the switches. Finally, this solution was dropped due to this drawbacks.

A different way of resetting an integrator is the charge-balanced method (see Fig. 4.4 in the next section). Instead of discharging the capacitor by shortening it with a low impedance switch, a reference current is induced. This approach has the advantage that the signal current can be integrated continuously. After a certain charge has been accumulated in the integration capacitor, the reference current, which has opposing polarity of the signal current, is added for a fixed time interval ΔT. Thus always the same amount of charge $Q_{ref} = I_{ref} \cdot \Delta T$ is pulled out. The whole process of charging and discharging the capacitor is in equilibrium. Hence the periodicity of inducing the reference current depends on the amplitude of the signal current and can be measured as an output frequency. This method enables a high dynamic range of more than 140 dB. Moreover, no ADC is needed – as in the previous circuits – and the timing for the reference current switch is simple. The output signal of the charge-balanced converter is a frequency, which simplifies the further data transmission. After weighing the pros and cons of each proposal, the solution with a charge-balanced current-to-frequency converter (CFC) was chosen. It will be presented in more details.

4.3 Current-to-Frequency Converter

4.3.1 Functional principle

The basic principle of the CFC is shown in Fig. 4.4 a), while the detailed schematic is presented in Fig. A.1. It consists of an integrator, whose capacitor is charged by the signal current and discharged by a fixed reference current. The concept of a CFC was successfully developed by [Ree-96], [Ree-99]. The authors investigations are based on the work of [Sha-70].

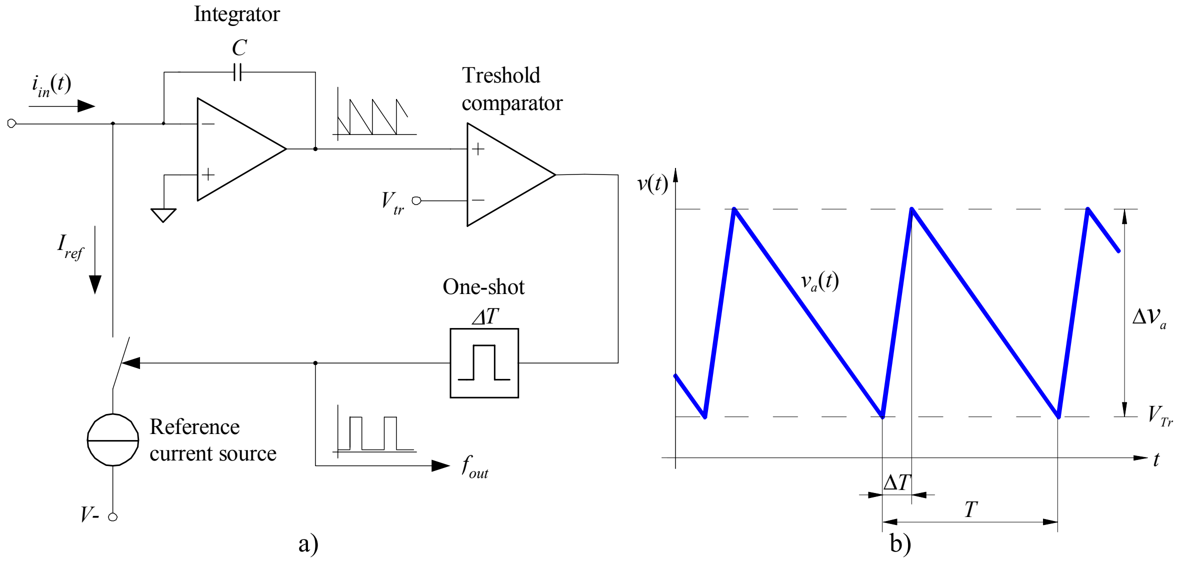

Fig. 4.4 Principle of the charge balanced current-to-frequency converter. a) Basic schematic. b) Output voltage of the integrator with a signal current near to the maximum value.

Figure 4.4 b) depicts a typical analog output voltage of the CFC with a constant input current that is almost at the maximum value of the operating range. If a positive input current is assumed, the output voltage ramps negative. After reaching a treshold voltage V_{Tr}, the one-shot connects the reference current I_{ref} to the summing node for a fixed time interval ΔT. As the reference current has the opposite polarity and is larger than the signal current, the integrator output is driven back. After I_{ref} is disconnected, the output ramps down again until it hits the treshold. Assuming an ideal op amp, with no input current and no offset voltage, a fixed charge $Q_{ref} = I_{ref} \cdot \Delta T$ is induced into the summing node of the op amp during the reset period ΔT. Since the treshold voltage as well as the integration capacitor have fixed values, Q_{ref} equals the accumulated charge due to the signal current Q_{in} during one period T:

$$Q_{in} = \int_{T} i_{in}(t)dt = Q_{ref} \tag{4.1}$$

where $i_{in}(t)$ is the signal current. The number of resets per time equals a frequency that is proportional to the average input current during one period. In order to generate this more handy expression, the integral in Eq. 4.1 is substituted by the average current $\overline{i_{in}} \cdot T$, while Q_{ref} is replaced by $I_{ref} \cdot \Delta T$:

$$\overline{i_{in}} \cdot T = I_{ref} \cdot \Delta T \tag{4.2}$$

thus the output frequency can be obtained by

$$f = \frac{\overline{i_{in}}}{I_{ref} \cdot \Delta T}. \tag{4.3}$$

The value of the integration capacitor C doesn't occur in Eq. 4.3 and thus has no influence on the output frequency. However, it has to be selected carefully because it determines the amplitude of the integrator output voltage but also the susceptibility to noise and to the charge injection from the current switch.

4.3.2 Circuit design

First of all, the operating range in terms of input current must be determined. The CFC was designed in such a way to produce an output frequency with a duty cycle of 50% at the maximum input current[7]. In addition, the front end must be able to acquire the different losses faster than the corresponding dump interval. In section 2.5, the dump level was set to 50% of the quench level. Consequently, the dump levels are a much better design criteria. Figure 4.5 depicts the maximum dump level at 450 GeV and the minimum dump level at 7 TeV. The first CFC design criteria is the maximum current that can be measured without overloading the CFC. It is marked in the diagram with a circle. Fortunately, this point is less severe – any losses above this level would anyway lead to a beam dump, so the losses needn't to be measured up to the quench level. Therefore, the maximum current is set just above the dump level to 200 μA. The reference current must be 400 μA to establish the 50% duty cycle at the maximum input current. However, the maximum current could be exceeded particularly by short spikes (see Fig. 4.6). To handle these spikes, a passive pre-integrator was designed that integrates the chamber current over a short time. This permits a higher effective dynamic range. Moreover, the pre-integrator also enables a proper termination of the chamber cable.

The second design criteria is the maximum frequency. Although, the losses needn't to be acquired faster than 89 μs, they must be determined faster than the corresponding dump level

---

[7] From now on, the term 'maximum current' has to be understood as that current where the duty cycle equals 50%.

to react before the magnet would quench. The diagram in Fig. 4.5 shows the one integration time of the CFC. This curve equals the period of the output frequency and is nothing but the acquisition time of the CFC. To ensure the functionality, the curve must stay below the dump level at any time. Otherwise, the dump level would be reached before the CFC could measure it. Therefore, the most critical point is the minimum one-turn dump level at 7 TeV, which is emphasized with a circle. It leads to a maximum frequency of 5 MHz.

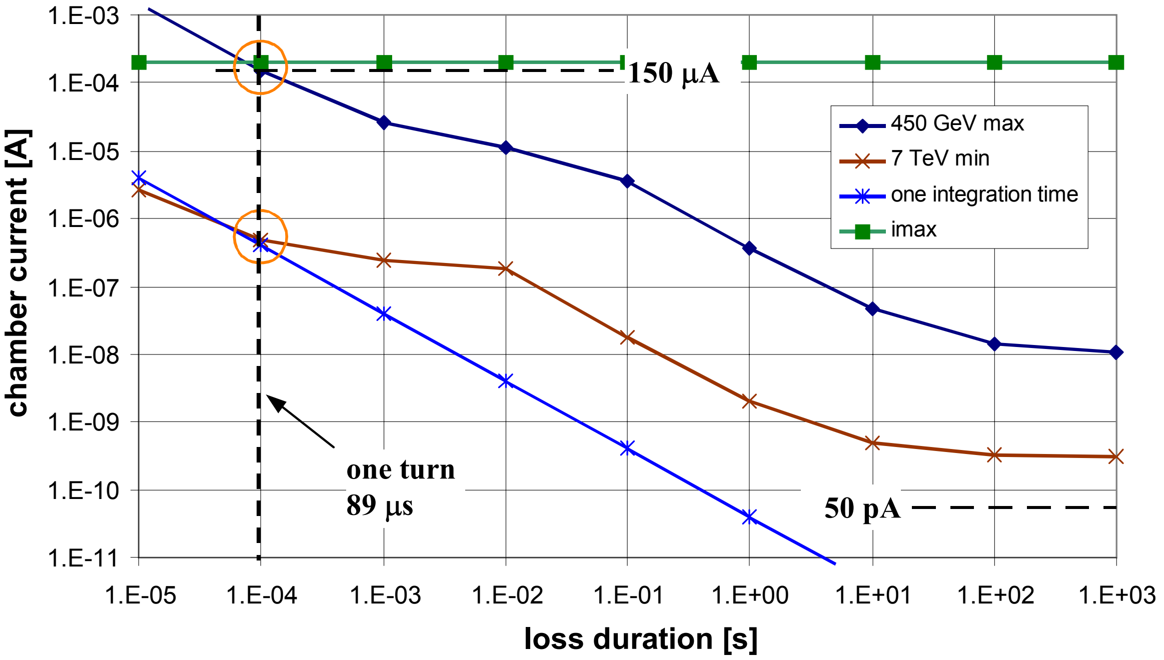

Fig. 4.5 CFC characteristic and nominal maximum chamber current compared with the dump levels. The maximum current is illustrated by the horizontal green line. It corresponds to a duty cycle of 50%. The blue curve shows the one integration time of the CFC. It must stay below the dump levels.

As already noted, the large number of 3000 beam loss monitors entails a non-adjustable circuit. The electronics should be a plug-and-play type, which can be replaced quickly without tedious calibration. Thus trimmers, to correct offset voltages or to set the time delay of the one-shot, should be avoided. In addition, the design must be robust and simple. To make the design process more transparent, the circuit in Fig. A.1 is grouped into the following functional units:

- Pre-integrator
- Analog integrator
- Treshold comparator
- One-shot
- Reference current source
- Current switch

PSpice was used throughout the design process to optimize the circuit elements. Then a prototype circuit board was created. The components were placed above a solid ground plane and their supply pins were bypassed with capacitors (typical value 100 nF). The connections were made as short as possible and the whole circuit board was placed in a metal housing for shielding. However, for some components no PSpice model was available (NE 521N, 74HCT123) and the real layout of the circuit can't be taken into account, too. Nevertheless, the simulation schematic in Fig. A.2 shows a very similar performance compared to the measured signals of the prototype circuit.

Before presenting the design of the different functional groups mentioned above, the main specifications of the CFC are summarized in Table 4.2. They constitute the guideline for the whole circuit design.

Table 4.2 Main specifications of the CFC.

Parameter	Value
Nominal maximum input current	200 μA
Reference current	400 μA
Minimum input current within the accuracy	50 pA
Output frequency at max. input current	5 MHz
Duty cycle at max. input current	50%

Pre-Integrator

The front end is designed for a maximum input current of 200 μA. But one has to distinguish between the long-term input current and the short-term pulse current. It can't be excluded, that the maximum input current will be exceeded. The circuit has to preserve its functionality even with short pulses above the maximum current and should not been driven into overload or saturation. According to Fig. 4.6 a), a passive RC-filter, consisting of R_2 and C_2, is connected to the op amp's input. In the case of an input current step, the output current of the RC-filter $i_{out}(t)$ will follow an exponential function and reaches the final step value after approximately $5 \cdot R_2C_2$. The capacitor C_3 in Fig. A.1 is neglected, since it doesn't have an influence on the pre-integrator. In order to obtain the desired one-turn resolution, the time constant has been set to 10% of the revolution time leading to $\tau = 8.9$ μs and to a total rise time of $5 \cdot \tau = 44.5$ μs, which equals half a turn. At short pulses with a pulse length $t_p < \tau$, the output current can be approximated by linear functions. Here the RC-filter behaves like an integrator. This fact is illustrated in Fig. 4.6 b) – short spikes, exceeding the maximum current, are integrated.

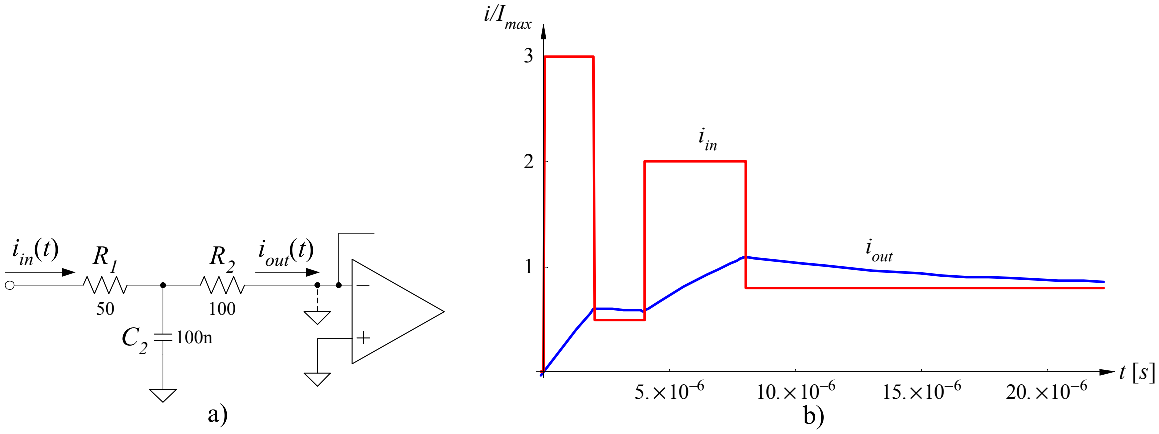

a) b)

Fig. 4.6 Pre-integrator: a) Circuit. b) Typical waveform.

Analog integrator

As mentioned above, the analog integrator is designed for a maximum nominal output frequency of 5 MHz at a duty cycle of 50%. In order to meet these specifications, an op amp has to be chosen which incorporates both, negligible input bias current and high bandwidth. The first requirement emerges since any input current of the op amp would add up to the signal current and fudge the result. The second requirement arises from the maximum output frequency and the fact that an op amp doesn't form an ideal integrator but comprises a time delay proportional to its bandwidth (see section 4.3.3). Any additional time delay reduces the stability of the CFC, which is nothing but a feedback loop. To form the analog integrator, the Burr Brown OPA627 was selected. It is used for low current, transimpedance amplifiers and shows excellent properties as listed in Table 4.3[8].

Table 4.3 Specifiactions of the OPA627.

Parameter	**Value (typ)**
Offset voltage	130 μV
Input bias current	2 pA
Noise density	4.8 nV/$\sqrt{\text{Hz}}$
Open-loop gain	116 dB
Gain-bandwidth product	16 MHz
Output voltage	±12.3 V
Differential input impedance	10^{13} Ω ‖ 8 pF
Slew rate	55 V/μs

---

[8] A complete description is given in the Burr Brown datasheet OPA627/OPA637.

The circuit in Fig. 4.7 mainly consists of IC_1 and the integration capacitor C_1. If an ideal op amp is assumed, the output voltage $v_o(t)$ of the integrator equals

$$V_o(s) = -\frac{I_{out}(s)}{sC_1} \rightarrow v_o(t) = -\frac{1}{C_1}\int i_{out}(t)\,dt. \tag{4.4}$$

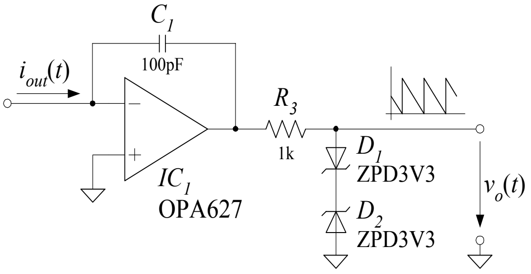

Fig. 4.7 Analog integrator of the CFC.

Although C_1 doesn't occur in Eq. 4.3 it determines the amplitude of the output voltage of the integrator. A higher output voltage swing results in more noise immunity[9] but also in a larger charge injection due to the reset switch. In addition, the finite bandwidth of the op amp and its slew rate limit the output signal rise. A good compromise seems to be a value of $C_1 = 100$ pF. In order to reduce the capacitor leakage to a minium, a polystyrene or polypropylene capacitor should be used (see section 4.3.3). At the maximum current the output signal amplitude is

$$v_o = \frac{(I_{ref} - I_{\max}) \cdot \Delta T}{C_1} = \frac{200\ \mu\text{A} \cdot 100\ \text{ns}}{100\ \text{pF}} = 0.2\ \text{V}. \tag{4.5}$$

This value doubles at low input currents to 0.4 V. The slew rate limits the output voltage ramp. At small input currents, the output voltage changes with $\frac{0.4\ \text{V}}{100\ \text{ns}} = 4$ V/μs, which is much below the slew rate of the OPA627. At overload, the clipping diodes D_1 and D_2 (3.3 V Zener diode) limit the output voltage of the integrator to ±4 V and protect the treshold comparator from overvoltage. The resistor R_3 limits the output current of the op amp to approximately 10 mA in such a case.

Treshold Comparator

The treshold comparator IC_2 triggers the one-shot IC_3 (see Fig. 4.9) in order to reset the integrator. Its output voltage V_B is connected to the input B of the one-shot. Figure 4.8 illustrates the comparator circuit. As already mentioned, any delay in the circuit must be avoided. Therefore, a high speed comparator, the NE521N, was selected. It has a propagation time of only 8 ns. However, it has to be supplied with ±5 V and the input voltage must be limited to

---

[9] This must be considered carefully, since a smaller value of C_1 also increases the noise gain.

that level, too. The comparator uses a positive hysteresis ΔV to avoid oscillation at low input currents and to establish a clean trigger signal for the one-shot. One can calculate ΔV from

$$\Delta V = \beta(V_{BH} - V_{BL}) \tag{4.6}$$

where $V_{BH} = 5$ V, $V_{BL} \approx 0$ V are the output voltages V_B in the high and low state respectively, and β equals the feedback factor

$$\beta = \frac{\Delta V}{V_{BH} - V_{BL}} = \frac{R_4}{R_4 + R_5}. \tag{4.7}$$

The upper and lower treshold of the comparator, V_u and V_l, can be determined by

$$V_u = V_{BH} \cdot \beta \tag{4.8a}$$

$$V_l = V_{BL} \cdot \beta. \tag{4.8b}$$

A hysteresis of $\Delta V = 50$ mV was chosen, which leads to a feedback factor of $\beta = \frac{0.05\,\mathrm{V}}{5\,\mathrm{V}} = 0.01$. The corresponding resistors are calculated with Eq. 4.7. Values of $R_4 = 1$ kΩ and $R_5 = 100$ kΩ lead to $\beta = 0.099 \approx 0.01$. Thus one obtains $V_u = 50$ mV as the upper treshold, while the lower one is $V_l \approx 0$ V. The small capacitor C_4 in parallel to R_4 increases the switching speed and stabilizes the comparator operation. A value of $C_4 = 10$ pF was selected.

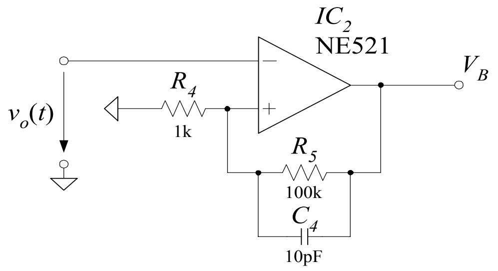

Fig. 4.8 Treshold comparator.

One-shot

The one-shot generates the fixed time ΔT to reset the integrator and turns the reference current ON and OFF. For the first stage of prototyping, the asynchronous monostable 74HCT123 in Fig. 4.9 was chosen. It is triggered by a rising edge at B. The pulse width is set by R_6 and C_5. To generate the maximum output frequency of 5 MHz with a duty cycle of 50%, a pulse width of $t_w = 100$ ns is needed. At these short pulse widths, no analytic expression is given by the manufacturers, but t_w can be taken out of Fig. 4.10[10]. The diagram yields to $R_6 = 5.2$ kΩ

---

[10] See the datasheet of the 74HCT123 for a detailed description.

and $C_5 = 10$ pF for a pulse width of 100 ns. Actually, the most accurate result was found with $R_6 = 5.6$ kΩ.

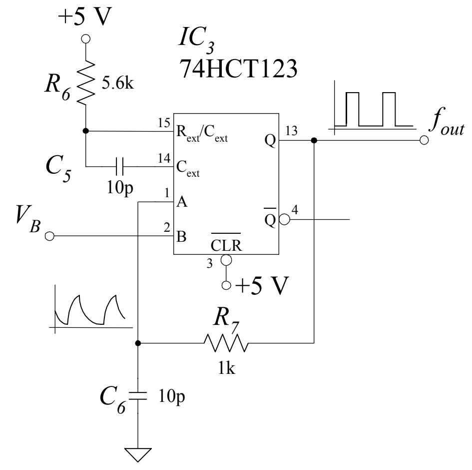

Trigger	A	B	Q	$\overline{Q}$
pos. Edge	Lo	↑	⎍	⊔
neg. Edge	↓	Hi	⎍	⊔

Fig. 4.9 One-shot circuit.

The one-shot is also essential for the proper operation in case of an overload. Although an input filter (= pre-integrator) is used to integrate fast spikes that exceed the maximum input current, a complete suppression can't be guaranteed. At overload, the CFC will not work correctly anymore, however, it should return to proper operation if the overload disappears. In addition, the overload situation should be signaled for the appropriate treatment of the CFC output signal.

The circuit in Fig. 4.9 is able to handle overload situations because of the feedback from Q to A. In the initial state, Q (= A) is low and the one-shot is triggered with a positive edge at B. Once triggered, Q goes high, which changes the trigger mode to negative edges. At normal operation, the comparator signal V_B is already low when Q falls back to low and the one-shot isn't retriggered. However, in the case of overload, the comparator signal is still high and the one-shot is immediately fired again. It will oscillate in the astable mode until B goes low again.

To limit the output frequency at overload to approximately 6 MHz, Q is not directly connected to A but via a lowpass formed by R_7 and C_6. This will simplify the further readout system because any frequency above 5 MHz signals an overload. The maximum output frequency of 6 MHz needs a minimum time delay of $t_d = \frac{1}{6\times10^6\ \mathrm{Hz}} - 100\ \mathrm{ns} \approx 66$ ns in the feedback loop. A direct connection between Q and A produced a delay of 42 ns. Hence the lowpass must generate an additional delay of 24 ns. If Q goes low, the voltage at A will follow the exponential characteristic

$$V_A = V_{QH} \cdot e^{-\frac{t}{R_7 C_6}} \tag{4.9}$$

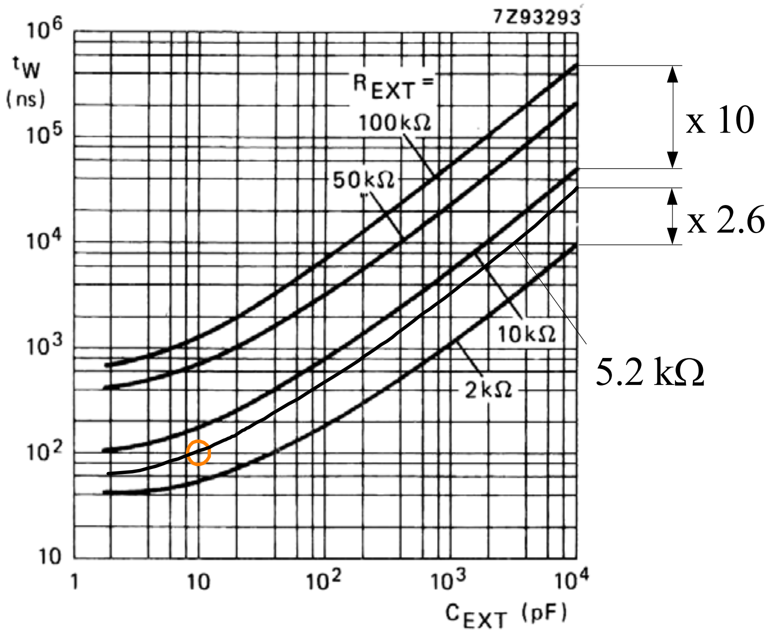

Fig. 4.10 Typical output pulse width at capacitor values below 10 nF for different timing resistors (Philips Datasheet 74HCT123).

where V_{QH} is the high level of Q. The one-shot will be triggered if V_A reaches the treshold of the low level input voltage, which is about 0.8 V for the HCT logic family. If $V_A = 0.8$ V and $V_{QH} = 5$ V are inserted in Eq. 4.9, the time constant equals $R_7C_6 \approx 13$ ns. Finally, $R_7 = 1$ kΩ and $C_6 = 10$ pF were chosen, which lead to accurate results.

There is one point that should be emphasized to avoid a misunderstanding of the overload status. If the signal current exceeds a certain level, the reference charge $Q_{ref} = I_{ref} \cdot \Delta T$ is not sufficient to reset the integrator. Hence the output voltage of the integrator stays below 0 V and doesn't reset the comparator either. However, the one-shot works in astable mode and will continue to generate output pulses, each equal to Q_{ref}. One may consider an overload to be harmless, regarding a longer time period: If the overload disappears again, the one-shot will drive the integrator output voltage back to 0 V and the total charges are equal. The PSpice simulation in Fig. 4.11 shows such a situation.

As shown in the picture, the output voltage of the integrator is driven down. After the overload has disappeared, the one-shot is still working in the astable mode and drives the integrator output back. Over the whole time period, the measured charge equals the charge generated by the input current. This works fine, until the op amp saturates. In this case, the charge balance can't be maintained anymore and the error increases dramatically.

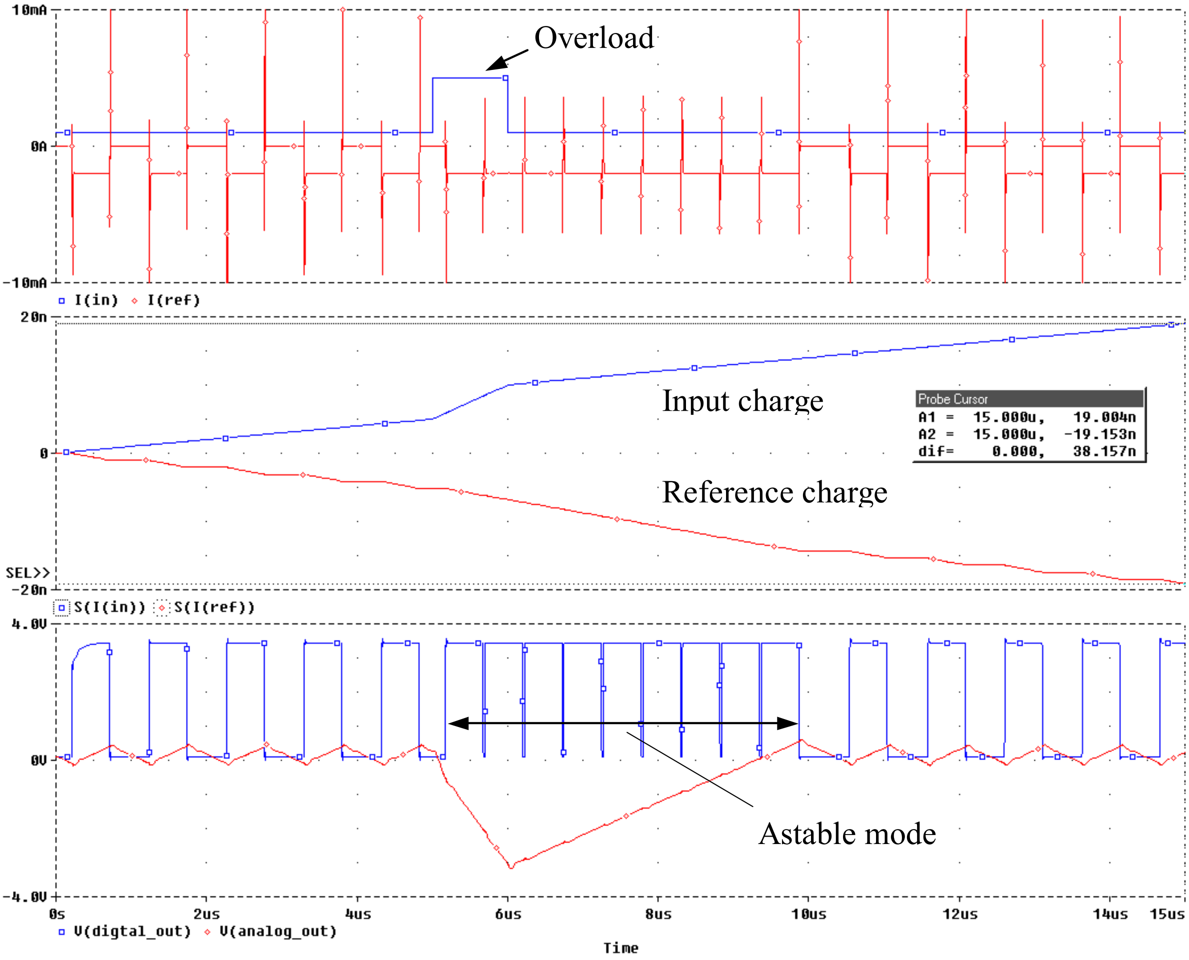

Fig. 4.11 PSpice simulation of an overload situation. The top waveforms show the signal current I(in) and the reference current I(ref). In the middle, the input charge and the total reference charge are calculated. They are identical at the end of the time scale. The bottom waveforms show the analog output voltage of the integrator and the output of the one-shot (digital_out, without the lowpass for the additional delay).

Reference Current Source

The reference current I_{ref} discharges the integration capacitor C_1 during the reset. According to Table 4.2, the reference current is $I_{ref} = 400\ \mu$A. For the first stage of prototyping, the simple transistor circuit in Fig. 4.12 was designed. To calculate the bias point the emitter potential was set to $V_E = -5$ V, which ensures a high temperature stability. Since the emitter current is about the collector current ($= I_{ref}$), the emitter resistance is obtained by

$$R_{10} = \frac{V_E - V_-}{I_{ref}} = \frac{-5 + 15}{400 \cdot 10^{-6}} = 25\ \text{k}\Omega. \tag{4.10}$$

The closest standard value of 24 kΩ was selected. The base voltage V_B results from the emitter potential V_E plus the 0.6 V base-emitter voltage drop of a common silicon transistor, which leads to

$$V_B = V_- + I_{ref}R_{10} + 0.6\ \text{V} = -15 + 0.4 \cdot 24 + 0.6 = -4.8\ \text{V}. \tag{4.11}$$

This voltage must be established by the base voltage divider R_8, R_9. For an accurate calculation, one has to consider the base current, which is $I_B = \frac{I_{ref}}{h_{FE}} = 1.6\ \mu\text{A}$. Here the minimum small signal gain of the BC 184, $h_{FE} = 250$, was assumed. A current I_D in the voltage divider that is much bigger than I_B, e.g. 100 μA, makes V_B independent of I_B. The resistor values can be calculated with

$$R_8 \approx \frac{V_+ - V_B}{I_D} = \frac{5 + 4.8}{100 \cdot 10^{-6}} = 98\ \text{k}\Omega, \tag{4.12a}$$

$$R_9 = \frac{V_B - V_-}{I_D} = \frac{-4.8 + 15}{100 \cdot 10^{-6}} = 102\ \text{k}\Omega. \tag{4.12b}$$

The standard values $R_8 = 91\ \text{k}\Omega$ and $R_9 = 100\ \text{k}\Omega$ were selected. For a constant current source, the selection of the transistor type is not that critical as for a high-frequency amplifier. It should have a high differential current gain h_{FE} in order to provide a high output impedance. Because the maximum load is the ON-resistance of the JFET Q_2 or Q_3, which is $R_{on} \approx 250\ \Omega$, the output impedance need not to be very large either. Thus the BC 184 was taken because it is a standard component at CERN.

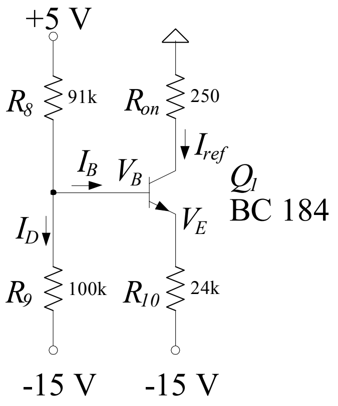

Fig. 4.12 Reference current source.

Current Switch

The current source is turned ON and OFF by the series-shunt switch in Fig. 4.13. For a better understanding, the on-resistance of the JFETs are illustrated. To build up the switch, the p-channel JFET J176 was used. It has a pinch off voltage of max. 4 V and can directly be driven by the outputs Q and $\overline{Q}$ of the one-shot IC_3. In comparison, n-channel JFETs have shorter transition times but also need a level converter to produce a negative gate voltage. The J176 has a total response time of 25 ns, which also depends on the drain current. If the CFC integrates only the signal current, the series switch Q_2 is opened, while the shunt switch Q_3 conducts I_{ref} to ground. The voltage V_{in} can be calculated by $R_{on} \cdot I_{ref} = 100$ mV. Since the drain of Q_2 (out) is connected to the summing point of the op amp, which corresponds to virtual ground, the total voltage drop over drain and source of Q_2 is very small, about 100 mV. Thus the drain-source leakage current can be neglected. The much more serious shortcoming is the charge injection of the JFET and the gate-source leakage current (see section 4.3.3). If the comparator triggers a reset, the JFETs are driven complementary. Q_3 opens and I_{ref} is induced via the closed Q_2 into the summing point of the op amp. Again, the voltage drop over the closed switch is about 100 mV, not loading the current source considerably.

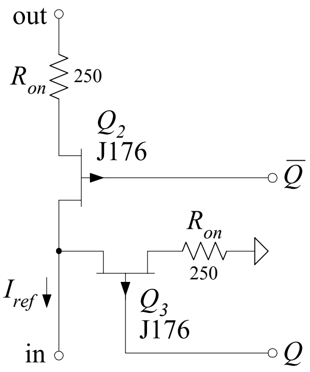

Fig. 4.13 Current switch.

CFC readout system

In order to complete the front end design, a way to transmit the output frequency must be foreseen. The signal transmission itself will be discussed in section 5.4 thus only the basic considerations subjected to the front end design are presented. The main obstacle in the data transmission is the long cable together with the high CFC output frequency. It has been shown, that the high maximum frequency of the CFC necessitates from the low dump levels at 7 TeV (see Fig. 3.4), which results in short output pulses of 100 ns length. But transmitting short pulses over a long cable is tricky. The low bandwidth of the cable leads to pulse distortion and intersymbol interference. One way to overcome this problem would be the usage of harmonic, DC-free pulses but even with that technique pulse overlapping will occur. Moreover, the cable attenuation at 5MHz is so high, that it would be hard to extract the weak signal from noise. Consequently, such a data transmission would not be very reliable. One may consider external noise sources that generate spikes in the transmitted signal. It could not be avoided that such an induced pulse will be recognized as a valid data pulse and lead to errors.

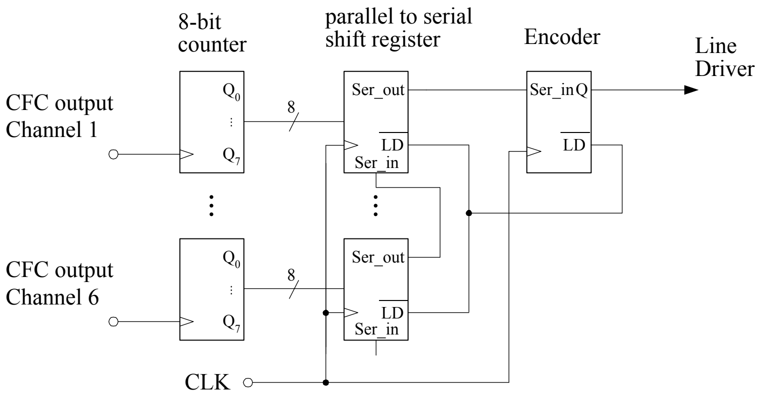

Fig. 4.14 Evaluation of the CFC output frequency with a counter-register pair. Cascading six channels leads to a multiplexed serial data stream.

Therefore, the CFC output frequency is converted into a digital number as shown in Fig. 4.14. A counter is placed on the CFC board to count the output pulses continuously. It is read out every 40 μs to provide at least two acquisitions per turn. The counter value is loaded into a parallel-to-serial shift register. Six front end channels are connected in series to form a multiplexed serial data stream. This way has several advantages:

- The required bandwidth for the data transmission is reduced. The losses need not be acquired faster than with single turn resolution (see Table 4.1). Hence there is no need for a 5 MHz acquisition rate that would only waste valuable bandwidth.
- The multiplexed data transmission means lower cable costs and less installation effort.
- If the data is transmitted digitally, it is easy to implement an error detection and correction respectively. Smart encoding paired with checksums increases the reliability of the whole beam loss system.

Of course, it must be mentioned that such a system entails problems, too. The front end is installed in the LHC tunnel, where a certain level of radioactivity will be present. Digital logic in such an environment can lead to severe problems. Radiation affects the performance of an electronic component in several ways. The examination of radiation effects isn't discussed because the electronics in the tunnel will be located in less radioactive zones. However, it should be emphasized that this fact must be verified in the further design process. In general, digital logic is less susceptible to external influence because of its high SNR due to the discrete signal levels. But if it is affected, the results could be devastating. If a bit toggles due to radiation, the error is 100%. At analog circuitry, one may observe an increased leakage current or less gain – which constitutes a continuous degradation of performance that can be surveilled.

4.3.3 Error calculation

To ensure the maximum specified error of $\pm 10\%$ for the beam loss detection, the error of the front end has to be calculated and verified. Equation 4.3 is written down again to examine the possible sources of error:

$$f = \frac{\overline{i_{in}}}{I_{ref} \cdot \Delta T} = \frac{\int_T i_{in}(t)\, dt}{I_{ref} \cdot \Delta T} \tag{4.13}$$

According to that equation, the accuracy of the output frequency is affected by four variables:

1. The input current $i_{in}(t)$, which is affected by leakage currents.
2. The reference current I_{ref} depends mostly on the accuracy of external components.
3. The reference time ΔT is set by external components but also varies among different chips.
4. The exact integration of $i_{in}(t)$ can only be performed by an ideal op amp – that doesn't exist.

One important part of the CFC is not stated in the above list – the current switch. In Eq. 4.3 this switch is assumed to be ideal. However, a JFET can't be turned ON and OFF infinite fast, especially at low drain currents. Moreover, it doesn't isolate the controlling gate voltage from its output and input terminals. Whenever the current switch is operated, the gate voltage is coupled to the drain and source, which is called charge injection. This nonideal behavior must taken into account:

5. Switching speed and charge injection of the current switch.

Of course, noise is a source of error that must be considered, too. Measurements in the laboratory as well PSpice simulations showed an rms noise voltage of approximately 500 μV, which corresponds to a peak-peak value of approximately 3 mV. The amplitude of this noise is not critical but it introduces a jitter. However, at low output frequencies this error is negligible, while at high output frequencies, the values are averaged over 40 μs. Thus the noise of the circuitry itself is neglected.

A much more serious noise source is the pickup of external signals by the cable between the ionization chamber and the front end. Measurements in the laboratory showed a clear superposed signal of 50 Hz. The influence of this interference depends on the front end frequency. It will vanish if this frequency is a factor of 50 Hz. However, the frequency of the CFC is not discrete thus noise suppression by multiples of the noise frequency can't be achieved. The laboratory measurements are performed in a complete different environment than in the tunnel, where the electronics will be installed. In the laboratory, many devices are operated in the nearby of the front end test circuit. It is assumed that there is more interference from adjacent devices than in the tunnel. In contrast, the radiation exposure in the tunnel will be much higher. This exposure influences the accuracy of almost all components of the front end. However, no investigations have been made in that direction. First of all, the location of the front end in the tunnel is assumed to be very low radiated and second this topic would need excessive test, which would go beyond the subject of this thesis. Thus radiation influence is not taken into account. Moreover, changes in the supply voltage are also neglected as well as the influence of the ambient temperature, since it is assumed to be constant at 25 °C.

1. Leakage currents

The leakage currents are summarized in Fig. 4.15. They comprise

- The bias current i_b of the op amp,
- the leakage current i_{off} of the JFET current switch,
- leakage currents i_l due to the board layout, the cable and the capacitors of the pre-integrator, and
- the leakage current i_c due to the parasitic conductivity of the integration capacitor.

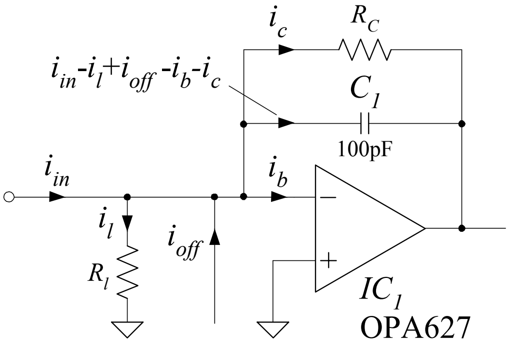

Fig. 4.15 Leakage currents of the CFC.

The influence of the offset voltage V_{os} can be neglected, since the impedance at the inverting input of the op amp (output impedance of the ionization chamber, input impedance of the op amp, parasitic impedance of the layout) is very high. The measurement of all these different leakage currents is rather tricky but the task can be simplified if only the total leakage current has to be measured. To determine this current, the CFC is operated with no input source and with the reference current source switched OFF[11]. Then the output voltage of the integrator is measured over 20 s as shown in Fig. 4.16.

---

[11] The leakage current i_c can't be considered with this method but it is much smaller than the other error terms.

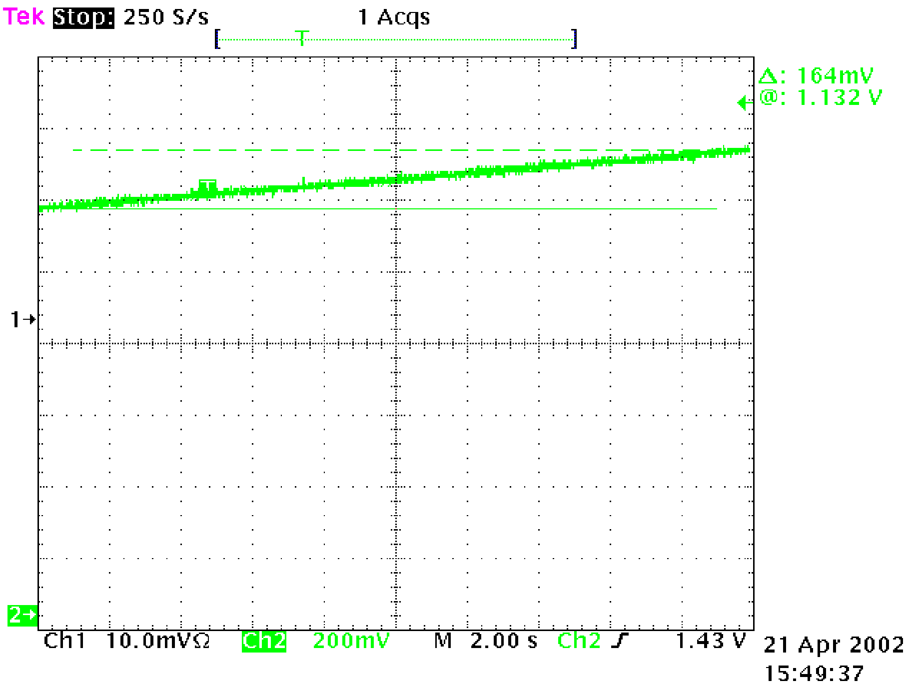

Fig. 4.16 Output voltage of the analog integrator due to the total leakage current.

The picture shows a change in voltage of 164 mV over 20 s. In order to calculate the leakage current, the exact value of C_1 must be verified. A measurement showed a capacitance of 99.6 pF, leading to a total leakage current of

$$i_{leak} = C_1 \frac{\Delta v}{\Delta t} = 99.6 \cdot 10^{-12} \frac{0.164}{20} = 0.82 \text{ pA}. \tag{4.14}$$

Thus the leakage current is very small. Moreover, some other answers can be found from Fig. 4.16. The characteristic is linear, so the influence of the parasitic resistor R_c seems to be negligible, too. This is also confirmed by the fact that the output voltage saturates at +4 V, which is set by the clipping circuit. The resistor R_c forms a lowpass with C_1 limiting the ideal behavior of the integrator. At low frequencies, the circuit works as a lowpass with a cut-off frequency of $\frac{1}{2\pi R_c C_1}$. Since no typical lowpass behavior was observed, R_c can be neglected. With Eq. 4.14, the error due to the leakage current is

$$e_{leak} = \frac{-i_{leak}}{i_{\min}} \cdot 100\% = \frac{-0.82}{50} \cdot 100\% = -1.6\% \tag{4.15}$$

where $i_{\min}$ was set to 50 pA for the worst case. The error is negative because the leakage current reduces the signal current.

2. Reference current

The accuracy of the reference current is mainly a factor of the external components in Fig. 4.12. To calculate the error, the Monte Carlo analysis in PSpice was used. The resistors are selected from the E24 series, having a tolerance of $\pm 5\%$. After 30 Monte Carlo runs, the output current is likely to have an accuracy of

$$e_{I_{ref}} = \pm 7\%. \tag{4.16}$$

3. Reference time

Since the supply voltage as well as the ambient temperature are assumed to be constant, the main sources of error are the external components. In addition, the 74HCT123 shows a certain distribution in accuracy itself. If several chips are compared, using the same external RC-combination and having the same supply voltage and temperature, a typical variation in the pulse width of $\pm 4\%$ can be observed. Figure 4.10 is drawn again in Fig. 4.17 to estimate the influence of the external components R_6 and C_5 on the accuracy. The characteristic is linearized at 10 pF. However, a constant slope in a double logarithmic plot corresponds to a certain exponent. Thus the linearized curve is of the function $y \propto x^a$ with the slope equal to a. From the diagram, the linearized function is calculated as $y \propto x^{0.4}$. If the capacitor has a tolerance of $\pm 10\%$, its influence on the pulse width is only $1.1^{0.4} = 1.04$, thus $\pm 4\%$. The tolerance of the resistor is $\pm 5\%$ since the curves are parallel and have the same proportionality. To combine all three tolerances, the variation of the monostable and the tolerance of the external components, the mean square error was used[12]. It is assumed that the different parameters are independent of each other and influence ΔT multiplicative. So the error is

$$e_{\Delta T} = \sqrt{0.04^2 + 0.04^2 + 0.05^2} = \pm 7.5\%. \tag{4.17}$$

4. Nonideal op amp parameters

The finite gain and bandwidth of a real op amp leads to an output voltage of

$$V_o(s) = -\frac{I_{in}(s)}{sC_1} \cdot \frac{1}{1 + \frac{1}{\beta A}} \tag{4.18}$$

---

[12] According to a Gaussian error distribution.

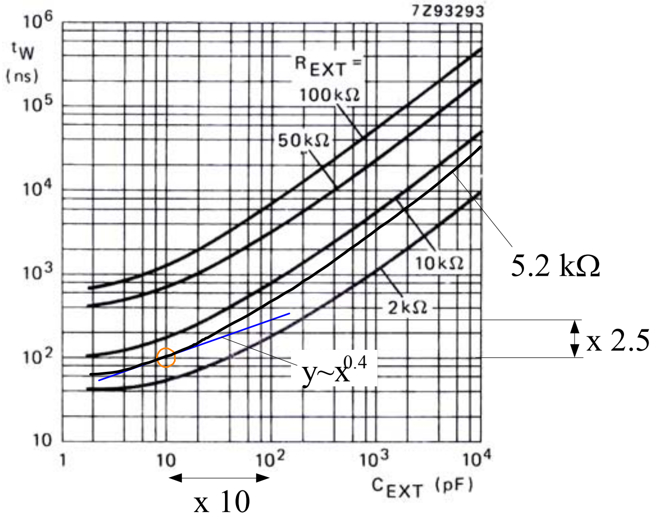

Fig. 4.17 The error due to the external components is estimated by linearizing the pulse width characteristic, which equals $y = x^{0.4}$.

where β is the feedback factor and A the open loop gain of the op amp. The feedback factor can be obtained by

$$\beta = \frac{R_p}{R_p + \frac{1}{sC_1}} \tag{4.19}$$

where R_p equals the parallel connection of the output impedance of the ionization chamber R_c and the differential input impedance of the op amp R_{id}. The other series resistances at the op amp input (cable resistance and input resistance of the pre-integrator) are neglected, since their values are much smaller compared to R_c. It is difficult to determine the input impedance, thus a value of $R_p = 10$ GΩ was assumed in the a worst case. The open loop gain of the op amp is approximated by the single pole transfer function

$$A = \frac{A_0}{1 + s\frac{A_0}{\omega_g}} \tag{4.20}$$

with the DC open loop gain A_0 and the gain-bandwidth product ω_g. If Eq. 4.19 and Eq. 4.20 are inserted into Eq. 4.18, the output voltage is

$$V_o(s) = -\frac{1}{sC_1} \cdot \frac{1}{1 + \frac{1}{A_0} + \frac{1}{\omega_g R_p C_1} + \frac{1}{sR_pC_1A_0} + \frac{s}{\omega_g}} \cdot I_{in}(s). \tag{4.21}$$

and for $A_0 \gg 1$, further simplifies to

$$V_o(s) = -\frac{1}{sC_1} \cdot \frac{1}{1 + \frac{1}{sR_pC_1A_0} + \frac{s}{\omega_g}} \cdot I_{in}(s) \tag{4.22}$$

by neglecting the small constant terms in the denominator. Equation 4.22 is now evaluated for low and high frequencies, respectively. At high frequencies, one obtains

$$V_o(s) = -\frac{1}{sC_1} \cdot \frac{1}{1 + \frac{s}{\omega_g}} \cdot I_{in}(s) \qquad \text{for } s >> \frac{1}{sR_pC_1A_0}. \tag{4.23}$$

Finally, the step response can be found by substituting $I_{in}(s) = \frac{I_{in}}{s}$ and calculating the inverse Laplace transform with the help of partial fractions:

$$v_o(t) = -\frac{I_{in}}{C_1}(t - \frac{1}{\omega_g} + \frac{1}{\omega_g}e^{-\omega_g t}). \tag{4.24}$$

At short time intervals, Eq. 4.24 shows a nonlinearity due to the term $\frac{1}{\omega_g}$. The step response was calculated for an input current of 100 μA and is shown in Fig. 4.18 a). The bandwidth $\omega_g = 2\pi\, 16$ MHz of the OPA627 leads to a the time delay of $t_d = \frac{1}{2\pi 16 \times 10^6} \approx 10$ ns. This delay does not necessary introduce a nonlinearity at high operation frequencies, as claimed by [Sha-70], but it degrades the stability of the circuit by increasing the loop delay. According to the calculation of [Sha-70], the error at 5 MHz must be $\frac{10\,\text{ns}}{100\,\text{ns}} = 10\%$ – which is by far not the case (see section 4.4). An integration cycle of the CFC shows two step functions at the op amp input, the first before and the second after the reset. The calculated delay emerges at both, thus canceling each other as long as $t_d \ll \Delta T$ – which is the case if a fast op amp, such as the OPA627 is used. An error would only occur, if t_d isn't much smaller than ΔT. In such a case, the two delays wouldn't cancel each other anymore. Thus no error is assumed due to this nonideal behavior.

Evaluating Eq. 4.22 at low frequencies leads to

$$V_o(s) = -\frac{1}{sC_1} \cdot \frac{1}{1 + \frac{1}{sR_pC_1A_0}} \cdot I_{in}(s) \qquad \text{for } s << \omega_g \tag{4.25}$$

while the step response is

$$v_o(t) = -I_{in}R_pA_0 \cdot (1 - e^{-\frac{t}{R_pC_1A_0}}). \tag{4.26}$$

The output voltage shows an exponential characteristic that saturates at $-I_{in}R_pA_0$. Because the term $R_pC_1A_0$ in the exponent is rather large, the exponential decay will be observed only at very long time intervals. For a better illustration, Eq. 4.26 is expressed in a series expansion[13] at $t = 0$ aborting after the second addend of the series:

$$v_o(t) = -\frac{I_{in}}{C_1} \cdot (t - \frac{t^2}{2R_pC_1A_0}) = -\frac{I_{in}}{C_1}t \cdot (1 - \frac{t}{2R_pC_1A_0}). \tag{4.27}$$

---

[13] The Taylor series of $f(x)$ at $x = x_0$ is $f(x) = f(x_0) + f'(x)(x - x_0) + f''(x)\frac{(x-x_0)^2}{2!} + ... + f^{(n)}\frac{(x-x_0)^n}{n!}$.

The equation shows the ideal transfer function $v_o(t) = -\frac{I_{in}}{C_1}t$ and a nonlinear term of $-\frac{t}{2R_pC_1A_0}$, which leads to a diversion of the characteristic at long time intervals as indicated in Fig. 4.18 b). The specified values lead to an error of

$$-\frac{t}{2R_pC_1A_0} = -\frac{t}{2\cdot 10^{10}\,\Omega\cdot 100\text{ pF}\cdot 10^{\frac{116\text{ dB}}{20}}} = -t\cdot 7.92\cdot 10^{-7}\,1/\text{s}. \tag{4.28}$$

Over an integration period of 10 s, which is eight times longer than the maximum expected integration time, the error would be $-7.92\times 10^{-6} = -0.0008\%$. Hence the low frequency error is neglected.

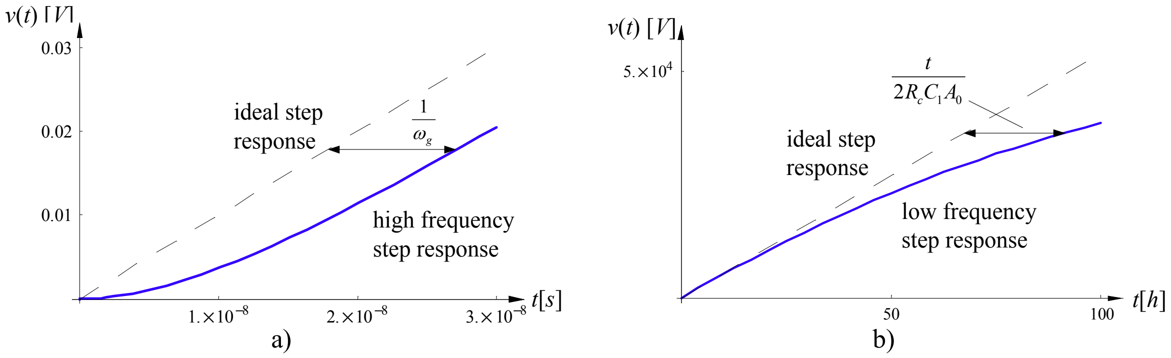

Fig. 4.18 Nonideal integration: a) Step response at short time intervals. b) Deviation from the ideal step response after long time intervals.

5. Switching speed and charge injection

The turn ON and OFF time of the current switch means another error term, especially if they are not the same. Normally, the turn OFF time of a JFET is longer than the turn ON time. However, the datasheet of the J176 specifies the same value for both. Thus this difference is neglected.

The charge injection of the current switch is presented in Fig. 4.19. If the reference current is switched ON and OFF, respectively, the gate voltage of Q_1 is mainly coupled via the parasitic capacitance C_{GD} between gate and drain into the summing node of the op amp. This assumes that the charge injections due to the parasitic capacitances between the other terminals cancel each other. Since the reference current is switched ON and OFF during one integration cycle, the corresponding charge injections Q_{GD} should cancel each other, too. This would be right, if C_{GD} is constant. However, it is not but varying with the voltage across the junction of the JFET. At zero bias (switch turned ON), the capacitance is a maximum and if the junction is reverse biased (switch turned OFF), it is a minimum. The datasheet of the J176 specifies $C_{iss} = 20$ pF at $V_{GS} = 0$ V and $C_{iss} = 10$ pF at $V_{GS} = 5$ V. For this calculation, C_{iss} is divided into two equal capacitors C_{GD} and C_{GS} leading to a drain-gate capacitance of $C_{GD} = 5$ pF10 pF. This difference would result in a charge injection unequal to zero and lead to a constant error in the output frequency.

However, several other aspects have also to be taken into account, such as the finite switching speed of the JFETs. Q_1 and Q_2 are driven complementary but for sure they are not switching exactly at the same time. In addition, the parasitic capacitance between drain and source must not be forgotten, too. These facts make it rather difficult to estimate the charge injection error. Therefore, this error term was measured by adjusting I_{ref} and ΔT to their nominal values and measuring the output frequency at signal currents much larger than the estimated leakage current. These measurements lead to an error due to charge injection of approximately

$$e_{\text{Charge}} = +2\%. \tag{4.29}$$

The right picture in Fig. 4.19 b) shows the analog output voltage of the integrator. The top waveform depicts the spikes due to the charge injection at the beginning and the end of ΔT. To suppress these spikes, the capacitor C_3 is connected to the inverting input of the op amp. It works as a fast charge storage. The injected charge is quickly accumulated by C_3 (and also by the pre-integrator capacitor C_2, see Fig. 4.6) and slowly transferred to C_1. The bottom waveform shows the same signal as above but with C_3 connected.

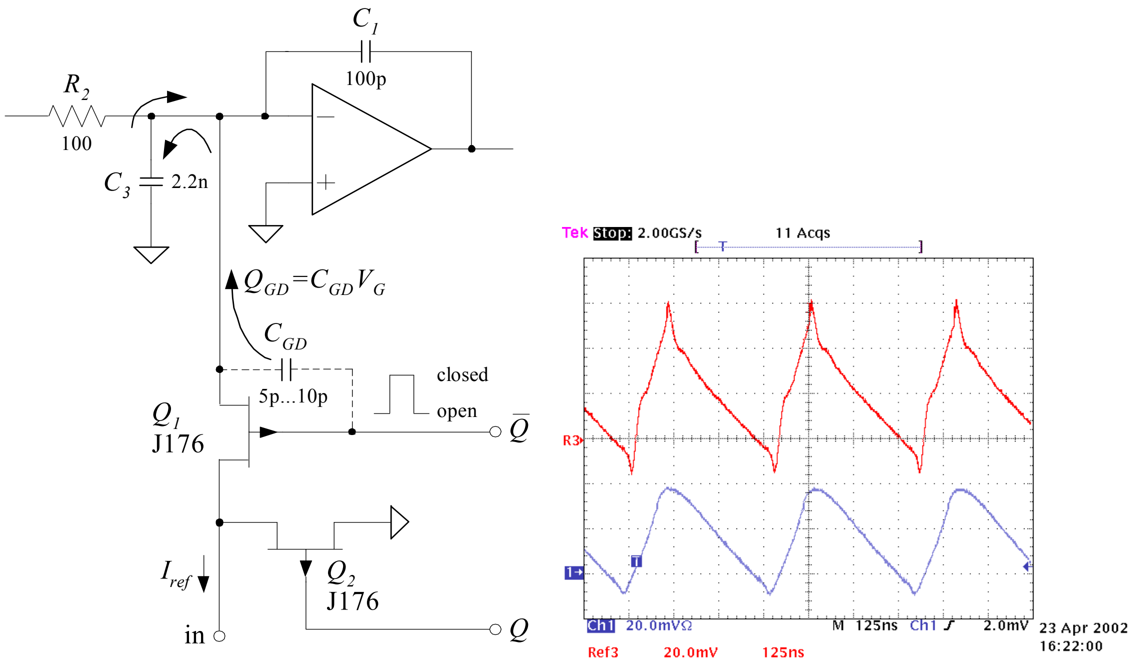

Fig. 4.19 Charge injection of the current switch. Left: Supression of the charge injection spike with the help of C_3. First, the injected charge is first stored in C_3 and afterwards slowly transfered to C_1. Right: Comparison of the integrator output voltage without (top) and with C_3 (bottom).

The above calculations revealed two different types of errors: Errors that are a function of the signal current (leakage current, op amp non-linearity) and errors, which are independent of the signal current (reference current, reference time and charge injection). The latter ones might be larger but can be easily taken into account by calibration. To sum up these constant errors, the mean square value is calculated:

$$e = \sqrt{e_{I_{ref}}^2 + e_{\Delta T}^2 + e_{\text{Charge}}^2} = -10.06\% \ldots +10.45\%. \tag{4.30}$$

This error can be reduced by using components with a smaller tolerance or more accurate circuits, such as a synchronous monostable to generate ΔT or an op amp current source to create I_{ref}.

4.4 Tests and Calibration

A precise current source (Keithley 6450) was used to generate currents between 50 pA and 500 μA to cover the whole dynamic range and to test the overload behavior. The analog output of the integrator was visualized on the scope (TDS744), while the output frequency was measured with a counter (Keithley 776/R). Figure 4.20 a) shows the analog output voltage of the CFC at an input current of 200 μA (top) and at 100 μA (bottom), each with the corresponding analog output voltage of the integrator (blue) and the digital output signal of the one-shot (green). At the maximum current of 200 μA, the integrator isn't reset every cycle because of the loop delay and the capacitors C_2 and C_3. After the reset is triggered, not only the injected charge but also a part of the reference charge is transferred to these capacitors. Thus the output voltage doesn't always reach the comparator treshold and the one-shot is retriggered, which leads to a small error of approximately -1.5% at high frequencies. At 100 μA (bottom) the signals clearly show the reset interval where the integrator is driven back.

In Fig. 4.20 b), the integrator output voltage at 1 μA (top) and 50 pA (bottom) is presented. The waveform at 1 μA illustrates the charge storage of C_2 and C_3. After the reset is accomplished, the stored charge is slowly transferred to C_1 leading to the curved characteristic. At 50 pA these discharge interval is too short to be observed, thus the output voltage shows a clear ramp. However, a 50 Hz interference signal is superposed, which will result in jitter. It is believed that this interference is generated by the adjacent equipment in the laboratory but it must be envisaged in the future development process.

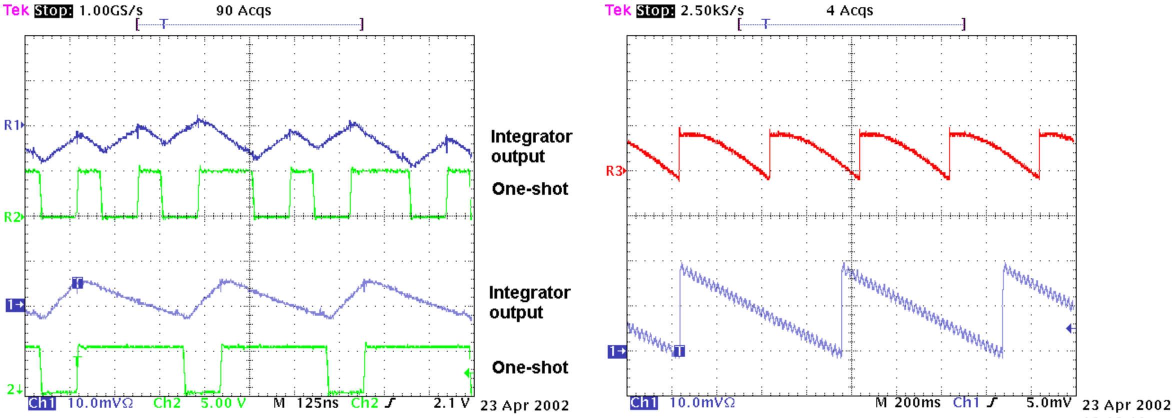

a) b)

Fig. 4.20 Analog output voltage of the integrator and the one-shot for a maximum current of 200 μA: a) Input current of 200 μA (top) and 100 μA (bottom). b) Integrator output at 1 μA (top), and at 50 pA (bottom) with a 50 Hz interference.

The dynamic behavior of the circuit was also tested. Figure 4.21 shows a square wave input current from 30 nA to 100 nA in the top waveform. Below, the corresponding analog output of the CFC is illustrated.

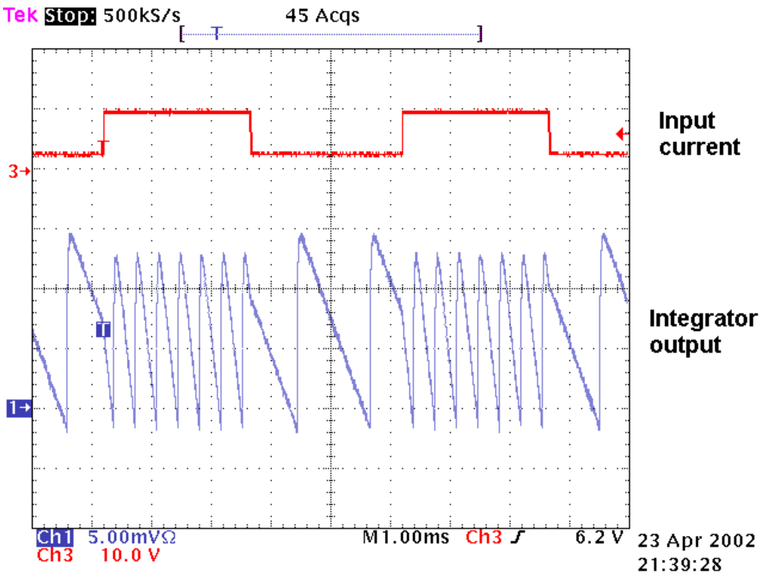

Fig. 4.21 Analog output of the CFC with a square wave input current from 30 nA to 100 nA.

Figure 4.20 and Fig. 4.21 show the output voltage according to the actual design specifications. However, the first prototype was designed for a maximum current of 1 mA because no measured data from the ionization chamber was available at that time. The circuit for a maximum current of 1 mA is the same as for $i_{\mathrm{max}} = 200\ \mu$A but the reference current is 2 mA and the capacitor C_3 is only 470 pF. Until now, no decision has been made what type of ionization chamber will be installed in the LHC. Discussions favor a bigger chamber than in the SPS, which will result in a larger signal current. Thus the maximum current is likely to occur between 200 μA and 1 mA. A larger current would further reduce the leakage error and yield to a higher linearity. Therefore, the presented CFC with $i_{\max} = 200$ μA can be seen as the worst case – however, it already shows a very good performance. Figure 4.22 illustrates the same output voltages as in Fig. 4.20 but for $i_{\max} = 1$ mA (the blue waveform in Fig. 4.22 shows the integrator output at 100 pA).

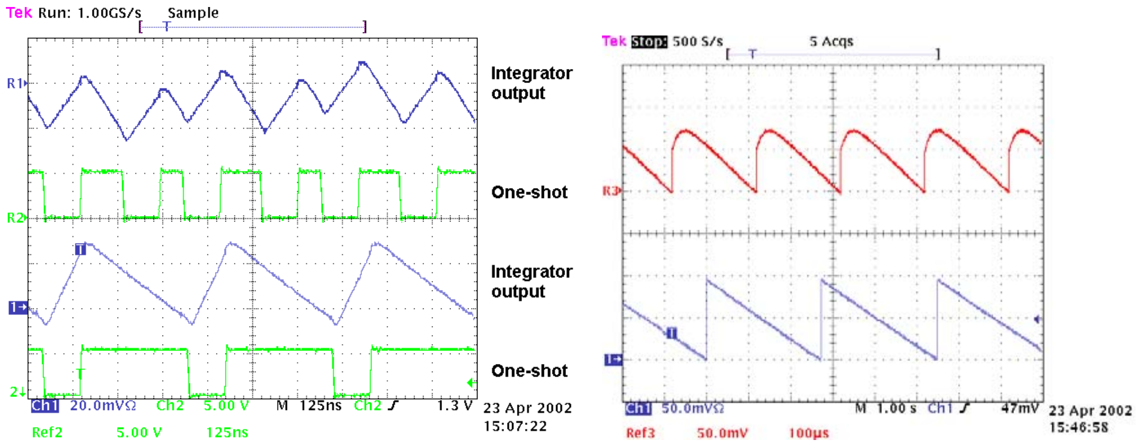

Fig. 4.22 Analog output voltage of the integrator and of the one-shot for a maximum current of 1 mA: a) Input current of 1 mA (top) and 500 μA (bottom). b) Integrator output at 1 μA (top) and 100 pA (bottom). The 50 Hz interference is too small to be observed.

The output frequency of the CFC was measured over the whole dynamic range and is presented in Fig. 4.23. The diagram compares the measured frequency (Frequency [Hz]) with the linearity error (Lin Error [%]). This error is specified by linearizing the measured curve at 5 kHz. The CFC shows a deviation from the linearized curve of less than ±0.5% over an input range of 500 pA to 100 μA. At low input currents, the error increases mainly because of the total leakage current. Above 100 μA, the one-shot works partly in the astable mode, which leads to a larger error. If the current exceeds 200 μA, the CFC is overloaded and becomes nonlinear. The maximum error within the dynamic range was only -2.62%, thus the CFC is well within the specified error margin of $\pm 10\%$. However, only the linear error is shown. The absolute error depends mainly on the actual value of I_{ref} and ΔT but is constant over the whole dynamic range. As already mentioned, it could be compensated with a calibration measurement. For the prototype circuit, the external components of the current source and the one-shot were optimized to measure 5 MHz at 200 μA input current.

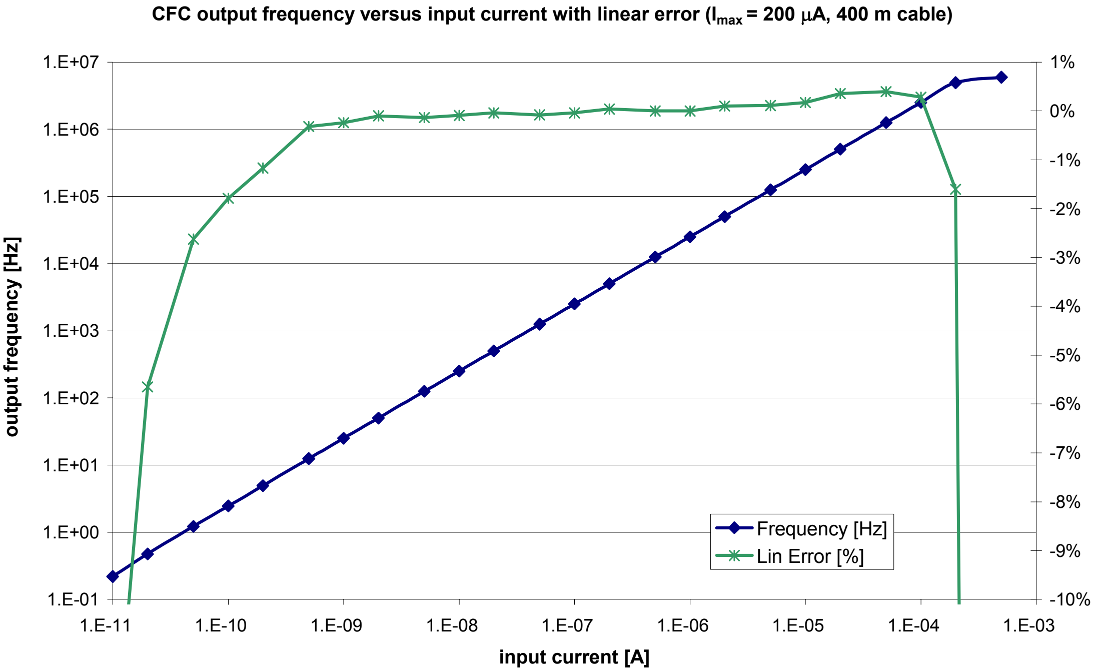

Maximum input current: 200 μA.

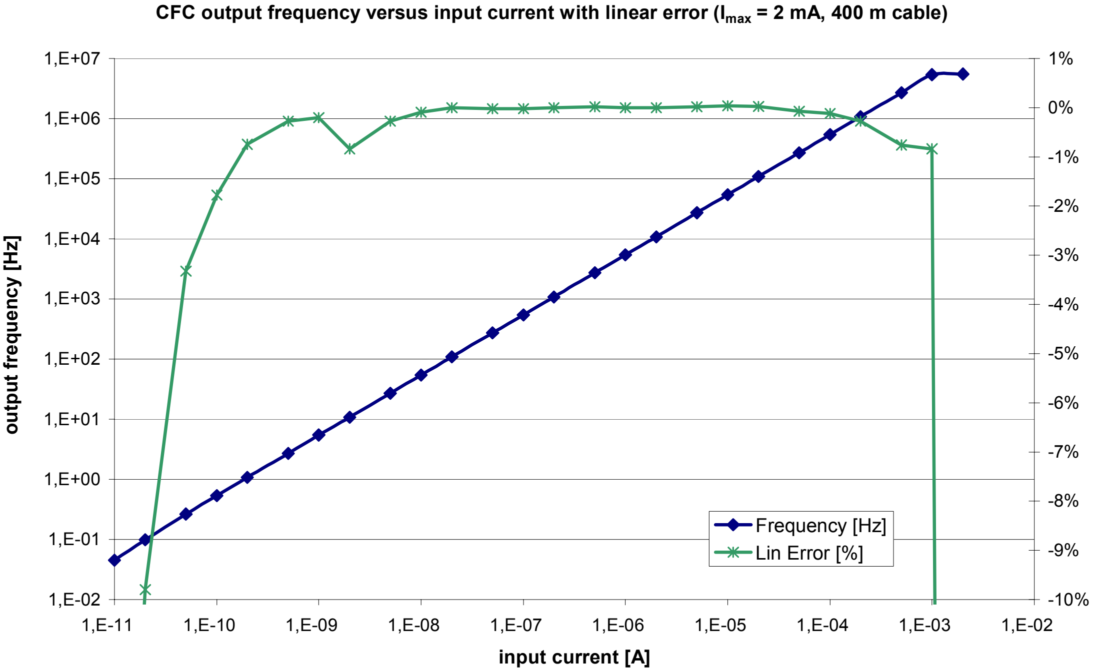

Maximum input current: 1 mA.

Fig. 4.23 CFC output frequency and linearity error versus input current for a maximum current of 200 μA (top) and 1 mA (bottom). Both pictures compare the measured frequency with the linearity error.

Most of the circuit development was done in the laboratory. As the first prototype design was finished, the SPS was already shut down for the annual maintenance. Nevertheless, a basic functional test could be performed. For this purpose, the SPS beam dump was used as a particle source. Because of the many dump actions during the SPS operation, the beam dump emits radioactive radiation, which is normally beyond the harmless dose. During the shutdown, this radiation decays – and can be measured with an ionization chamber. So the front end was connected to an ionization chamber, which was mounted underneath the beam dump. Figure 4.24 shows the measured waveform. At that time, the electronics was designed for a maximum frequency of 1 MHz at a maximum input current of 1 mA. The period of the output frequency was 14.6 s, thus the input current equals

$$i_{in} = \frac{i_{\max}}{f_{\max} T} = \frac{10^{-3}}{10^{6} \cdot 14.6} = 68.5 \text{ pA}$$

To compare this value, the signal of the adjacent SPS beam loss monitor was evaluated. This monitor delivered a current of 62.5 pA. The difference in the measured current is because of the local distance of the two chambers of about 5 m.

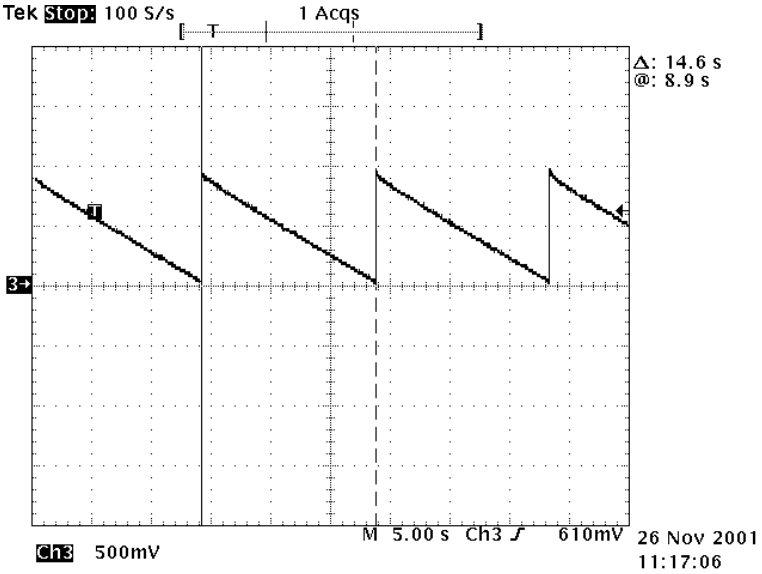

Fig. 4.24 Measurement of the remanent beam dump radiation with 200 m of cable between the chamber and the front end.

A point, which has not been mentioned yet, is the calibration of the beam loss system. As noted above, the CFC shows an excellent linearity over the desired dynamic range but the can have a certain offset according to Eq. 4.30 of up to $\pm 10\%$. T1his offset must be determined in advance to profit from the high relative accuracy. One could imagine, a calibration cycle when the LHC is down. This will ensure the accuracy and functionality of the front end. Several errors must be envisaged. However, no investigations have been made in that direction so far, but it must be considered in the future design process.

5 Data Transmission

As described in section 3.3, the evaluation of the particle loss and the beam dump decision must be done outside the tunnel, on the surface. Therefore, the front end output signal has to be transmitted over a distance of up to 2 km (few exceptional locations with even longer distances are not considered; special techniques will be applied in these cases). If a signal is transmitted over a lossy cable, it will be distorted, which limits the maximum data rate. Since cables are expensive and often not available in small quantities for testing, a calculation of the signal distortion is very useful. Usually, cables are specified in the frequency domain, thus the transient behavior must be derived. Beside the cable attenuation, the maximum data rate also depends on the appropriate signal encoding. First, the properties of the data transmission cable are examined.

5.1 Data Transmission Cable

There are several aspects, which affect the selection of a data cable, such as maximum data rate, length, environmental impacts and cable costs. These costs constitute the major part of the beam loss system due to the long cabling distances. Thus, a low-cost solution is aspired. Moreover, it would be convenient if a CERN standard cable could be used, since it is already specified and certified for the laying in the accelerator tunnel.

In order to transmit the beam loss signals from the tunnel to the dump controller on the surface, the CERN standard cable NG18 was proposed. It is used for transmitting data over long distances and consists of nine twisted pair wires with a common shielding. The few properties of the NG18, which have been found in the CERN catalogue, are listed in Table 5.1.

The cable is not specified very well, so measurements were performed to determine the line parameters (see section 5.2). An RLC meter (Philips PM 6303) was used to measure the series resistance R', inductance L' and capacitance C' of a one meter long piece of NG18. The

Table 5.1 Parameters of the CERN multiwire cable NG18.

Parameter	**Value**
Cross section	1 mm^2, 32 strands of ∅0.2 mm
DC resistance at 20°C	18.4 Ω/km
Insulation resistance	min. 20MΩ/km

measurement of R' and L' is done with the ends of the twisted pair shortened, while C' has to be determined with the ends open. The results of the measurement are presented in Fig. 5.1.

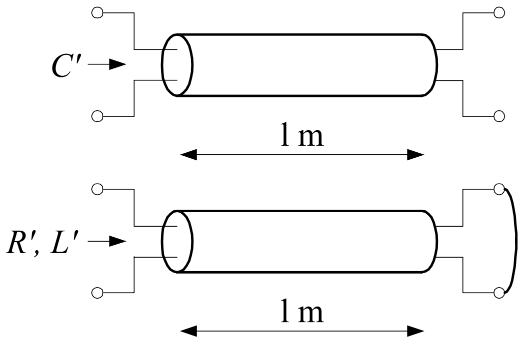

Parameter	**Value**
R'	37 mΩ/m
L'	0.653 μH/m
C'	53 pF/m

Fig. 5.1 Measurement of the line parameters R', L' and C'.

Consequently, the characteristic impedance is derived (see section 5.2)

$$Z_0 = \sqrt{\frac{L'}{C'}} = \sqrt{\frac{0.653 \cdot 10^{-6}}{53 \cdot 10^{-12}}} = 111\ \Omega \approx 110\ \Omega. \tag{5.1}$$

To perform measurements with long cabling distances in the laboratory, two coils of 100 m NG18 were connected in series. The pairs were looped to increase the length. With nine pairs of wire, the maximum length is $9 \cdot 200$ m = 1800 m. The attenuation versus frequency was measured using a single coil of 100 m to avoid any influence due to the connections and adjacent wires. Measurements with other length showed small deviations, however, the influence of the looping is considered to be small. Figure 5.2 shows the measurement setup. A function generator (Philips PM 5193) produces a sine wave, which is transformed into a differential signal by the EL2141 line driver. The positive and negative output of the driver are each connected to 56 Ω resistors to provide a source termination. The far end of the cable is terminated with its characteristic impedance of 110 Ω. The differential voltage at the far end is measured with two probes, connected to each terminal and their signal difference is evaluated. The measurement setup creates realistic circumstances, i.e. none of the two wires is grounded and the proposed driver for the signal transmission is considered, too. The EL2141 driver has a gain of two and the bandwidth is 100 MHz at that gain. Thus no error due to the finite risetime of the driver is assumed.

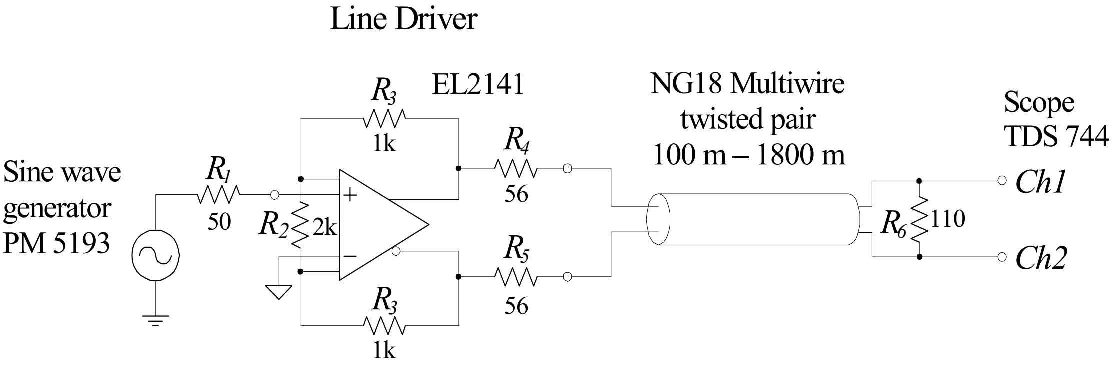

Fig. 5.2 Measurement of the cable attenuation.

The attenuation versus frequency at a length of 1 km for different types of cables is plotted in Fig. 5.3. The intended NG18, a VH4 and a Category 5 Ethernet cable are compared. The characteristic of the VH4 and Category 5 cable has been taken out of a catalogue. One will observe a flat curve up to 100 kHz where the attenuation is solely due to the cable resistance (= DC attenuation). Above 100 kHz, the skin effect becomes significant and leads to a slow roll off. At higher frequencies, the dielectric loss has to be considered and the attenuation plot falls off more steeply (see section 5.2). The VH4 cable shows a much better characteristic than the other types. It is used for transmitting video signals and much more expensive than the NG18. The Category 5's characteristic becomes better at high frequencies, but its cross-section is much smaller compared with the other cables, thus the DC attenuation is too high. Table 5.2 lists the attenuation at different cable length for the NG18. At longer cables, the attenuation can't be determined up to the maximum measurement frequency of 10 MHz. However, the table shows that the attenuation goes (almost) linear with the length, thus it is easy to calculate the attenuation at any desired length.

A major restriction using twisted pair cables is their relative high attenuation compared to coaxial cables. This attenuation alone would not be dramatic, since as long as the signal stays above the noise level it could be amplified to restore it. The real cause which limits the data rate over a cable, or restricts the maximum cable length to a certain limit, is the distortion of the signal. It is caused by the frequency dependent attenuation and phase velocity, respectively. A simulation of the frequency dependent losses as well as the calculation of the transient response is valuable.

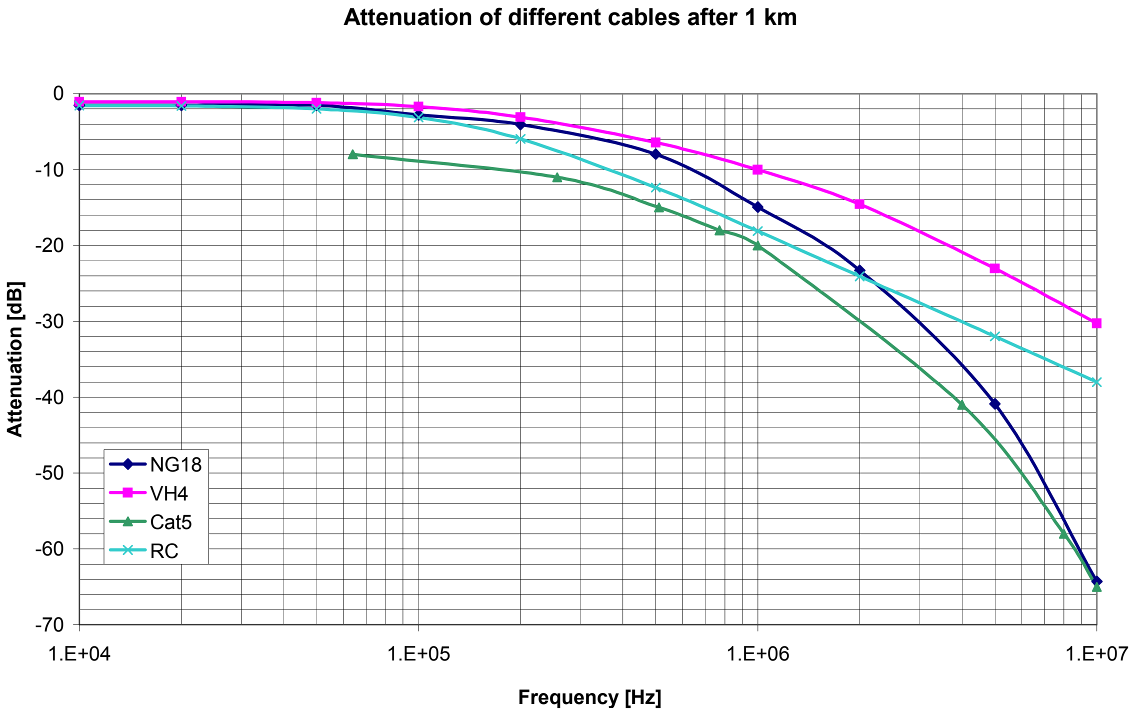

Fig. 5.3 Attenuation of different types of cables versus frequency.

Table 5.2 Attenuation of the NG18 at different cable lengths.

		Attenuation [dB]			
No.	f [Hz]	100 m	200 m	1000 m	1800 m
1	$1\cdot10^3$	-0.15	-0.41	-1.61	-2.67
2	$10\cdot10^3$	-0.15	-0.41	-1.67	-2.77
3	$20\cdot10^3$	-0.15	-0.41	-1.79	-3..08
4	$50\cdot10^3$	-0.15	-0.51	-2.44	-4.55
5	$100\cdot10^3$	-0.28	-0.66	-3.69	-6.74
6	$200\cdot10^3$	-0.41	-0.82	-5.19	-9.75
7	$500\cdot10^3$	-0.80	-1.55	-8.89	-16.55
8	$1\cdot10^6$	-1.49	-2.87	-14.71	-26.43
9	$2\cdot10^6$	-2.33	-4.63	-22.90	
10	$5\cdot10^6$	-4.09	-8.11		
11	$10\cdot10^6$	-6.43	-12.24		

5.2 Transmission Line Theory

Several books on that subject are available and this section will not cover all the topics. Nevertheless, a basic understanding how signals travel down a line is necessary to determine the maximum data rate of a data transmission system and to optimize the signal restoration. As not otherwise cited, the following formulas and theorems have been taken out of [Gar-87].

If the length of an electric connection can't be assumed much shorter than the wavelength of the signal on that line, the connection has to be treated as a distributed system. The question is, what is "much shorter" and how can we compare the length of a line to the wavelength, if the signal contains a broad spectrum, such as digital pulses. A (possible) answer is given by [Joh-89]. First, the length of a rising edge l_r is calculated by

$$l_r = t_r \cdot c \tag{5.2}$$

where t_r is the rise time of the signal and c the velocity of wave propagation on the line. This velocity is related to the dielectric permittivity ε and magnetic permeability μ with

$$c = \frac{1}{\sqrt{\mu\varepsilon}}. \tag{5.3}$$

Concerning cables, a typical value for c would be $2 \cdot 10^8$ m/s, which corresponds to a delay of $t_d = 5$ ns/m. Whenever the line is longer than one sixth of the length of the rising edge, the system has to be considered as distributed:

$$\text{Distributed system: } l \geq \frac{l_r}{6}. \tag{5.4}$$

In that case, electromagnetic wave propagation, which obeys Maxwell's equations, must be taken into account. These equations have to satisfy the boundary conditions and lead to a set of solutions called the modes of propagation. Consequently, an electromagnetic wave travels down a line in different modes affecting each other. A complete mathematical description is very tedious and often only solvable for special geometries. Fortunately, the geometry of a transmission line can support one propagation mode that dominates over the others. Only this dominant mode will be considered. The preferred mode of propagation is the transverse electromagnetic mode (TEM), which occurs in two metallic conductors surrounded by an isotropic and homogenous medium (air or dielectric). In this case, the longitudinal component of the magnetic and electric field vanishes. The TEM mode can be assumed to occur also at insulated wires and microstrip lines, where it is called Quasi-TEM. It leads to the well known equivalent circuit of an infinitesimal short piece of wire in Fig. 5.4, which is used to derive the transmission line equations.

This circuit describes a symmetric transmission line, such as an ideal twisted pair. The lumped model is only valid for $dz \to 0$. Often transmission lines are treated as lumped circuits using the above circuit and setting $dz = l_{ges}$, the total length of the transmission line. This simplification leads to incorrect results. A transmission line is often considered to be capacitive

– actually it is not but represents rather a resistive load at high frequencies. The capacitive model is only justified for short, unterminated connections, if the wavelength of the frequency on the line is much greater than its length.

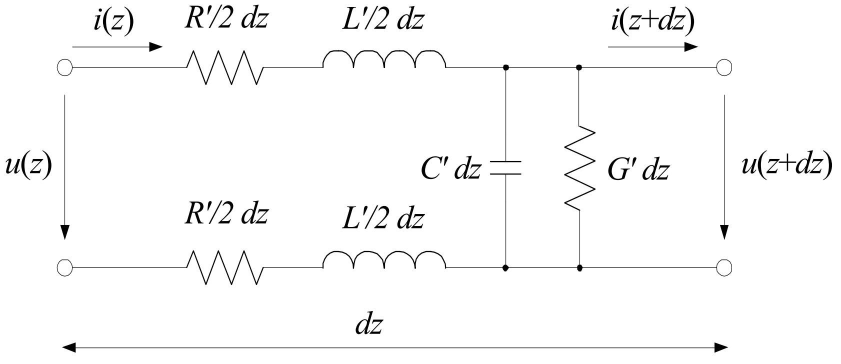

Fig. 5.4 Equivalent circuit for an infinitesimal short symmetric transmission line.

Parameter	Unit	Description
R'	Ω/m	series resistance models the ohmic losses
L'	H/m	inductivity of the line
C'	F/m	capacity between signal and return path
G'	S/m	parallel conductivity for the dielectric losses

If Kirchoff's law is applied on the circuit in Fig. 5.4 and sinusoidal excitation is used, one obtains two partial differential equations

$$\frac{\partial \underline{V}}{\partial z} = -(R' + j\omega L') \cdot \underline{I} \tag{5.5a}$$

$$\frac{\partial \underline{I}}{\partial z} = -(G' + j\omega C') \cdot \underline{V} \tag{5.5b}$$

with the complex amplitudes $\underline{V}$ and $\underline{I}$. These equations result in two traveling waves, one in the forward V_+ and one in the reverse direction V_-

$$V(z) = V_+ e^{-\gamma z} + V_- e^{\gamma z} \tag{5.6}$$

with the propagation constant γ

$$\gamma = \alpha + j\beta = \sqrt{(R' + j\omega L')(G' + j\omega C')}. \tag{5.7}$$

The real part α describes the attenuation of the wave and the imaginary part β the phase, which is related to the phase velocity v by

$$v = \frac{\omega}{\beta}. \tag{5.8}$$

This is an important fact considering the distortion of signals. For a distortion free transmission, v must be constant. Otherwise, the Fourier components of the signal have a certain phase difference to each other – which causes distortion. To make v constant, β must be a linear function of ω or the signal spectrum must be reduced to a single frequency (sine waves).

The relation between the voltage $V(z)$ and the current $I(z)$ on the line is described by the characteristic impedance Z_0:

$$Z_0 = \sqrt{\frac{R' + j\omega L'}{G' + j\omega C'}}. \tag{5.9}$$

In general, this impedance is complex. However, at high frequencies as well as for low loss lines with $R' \ll \omega L'$ and $G' \ll \omega C'$, the characteristic impedance becomes real and simplifies to

$$Z_0 = \sqrt{\frac{L'}{C'}}. \tag{5.10}$$

It is an important parameter of any transmission line. If the line is terminated with its characteristic impedance, no reflections will occur. In such a case, it behaves like an infinite long line. For a terminated transmission line, Eq. 5.6 can be rewritten considering only the forward traveling wave V_+:

$$V(z) = V_+ e^{-\gamma z} = V_+ e^{-\alpha z} e^{-j\beta z}. \tag{5.11}$$

In the further treatment of this topic, a matched transmission line is assumed. Moreover, the influence of external sources of error, such as noise or crosstalk, is neglected, too. Several special cases are examined to derive the time domain behavior of a terminated transmission line

a) Loss less line: R’ = 0, G’ = 0

In this case, the attenuation α and phase β simplify to

$$\alpha = 0 \tag{5.12a}$$

$$\beta = \omega\sqrt{L'C'} \tag{5.12b}$$

leading to a wave propagation of

$$V(z) = V_0 e^{-j\omega\sqrt{L'C'}z} \tag{5.13}$$

where V_0 is the voltage at the beginning of the line. Considering the rules of Fourier transform, the expression $e^{-j\omega\sqrt{L'C'}z} \propto e^{-j\omega T}$ in the frequency domain corresponds to a delay T in the time domain. Thus the voltage at any point on the line $V(z)$ is nothing but the voltage at the beginning V_0 delayed by T. The signal will neither be distorted nor attenuated.

b) Low loss line at high frequencies: R' $<<\omega$L', G' $<<\omega$C'

Here, the losses are considered to be small and independent of frequency. The attenuation α and phase β can be expressed by

$$\alpha = \frac{R'}{2Z_0} + \frac{G'Z_0}{2} \tag{5.14a}$$

$$\beta = \omega\sqrt{L'C'}. \tag{5.14b}$$

In comparison to the loss less case, the attenuation α is not zero but β remains the same value. Thus the signal amplitude decreases with the line length but the signal will not be distorted.

c) Transmission line at low frequencies: R' $>>\omega$L', G' $<<\omega$C'

At low frequencies, the series resistance R' exceeds the inductive term $\omega L'$. This behavior can be observed at telephone lines where the spectrum is placed around 3.4 kHz. The real and imaginary part of γ are the same:

$$\alpha = \beta = \sqrt{\frac{\omega R'C'}{2}}. \tag{5.15}$$

This leads to both, signal attenuation and distortion. β is not a linear function of ω anymore and the velocity of propagation is now frequency dependent. Hence any signal, which contains low-frequency parts in its spectrum will be distorted.

d) Low loss line: R(ω)' $<<\omega$L', G(ω)' $<<\omega$C'

The constant attenuation at high frequencies in Eq. 5.14a is only an ideal assumption. In reality, the skin effect and the frequency dependence of the dielectric loss have to be taken into account. Like at low frequencies, these effects lead to signal distortion and are examined in more details.

5.2.1 Skin effect

Until now, the line resistance has been considered to be constant. Thus the attenuation factor α would be constant, too. However, real transmission lines show a clear dependence of the attenuation versus frequency. One reason is the skin effect that increases the conductor resistance at higher frequencies.

At high frequencies, electric current flows only in the outer part of a conductor. The reason is the penetration depth of the electric field that decreases with rising frequency. Consequently, the effective area of the conductor is decreased – which increases its resistance. The skin effect is nothing but the solution of Maxwell's equations in a conductor. It entails a lot of mathematics, so only the results of the calculation according to [Sim-89] are presented. The impedance of a cylindric conductor can be described by

$$Z = R + j\omega L_i = \frac{E(r_0)l}{\hat{I}} \tag{5.16}$$

where the impedance is composed of a resistance R and an inner inductance L_i. It is calculated by dividing the voltage along the conductor $E(r_0)l$ by the amplitude of the electric current $\hat{I}$ passing the conductor. $E(r_0)$ denotes the electric field, which is a function of the conductor radius r_0. The result is a rather complicated function

$$Z = \frac{pl}{2\pi r_0 \sigma} \frac{J_0(pr_0)}{J_1(pr_0)} \tag{5.17}$$

where σ is the conductivity of the material, l is the length of the conductor, while $J_0(pr_0)$ and $J_1(pr_0)$ are the Bessel functions zero and first order, respectively. To describe the parameter p, the skin depth δ is introduced. It marks the depth, where the current density has fallen to $1/e \approx 37\%$ from its value on the surface:

$$\delta = \sqrt{\frac{2}{\omega\mu\sigma}}. \tag{5.18}$$

The equation shows that δ is a pure material parameter and decreases with $\sqrt{\omega}$. It contains the magnetic permeability μ and the conductivity σ. Finally, p is related to δ by

$$p = \frac{1+j}{\delta}. \tag{5.19}$$

Let's calculate the impedance described in Eq. 5.17 for high and low frequencies, respectively. The approximation at low frequencies leads to

$$R_{ac} \;=\; R_{dc} = \frac{l}{{r_0}^2 \pi \sigma} \tag{5.20}$$

$$\omega L_i = 0 \tag{5.21}$$

thus the real part R_{ac} (the index 'ac' indicates that the skin effect is considered) corresponds to the DC resistance, while the imaginary term is zero. This is the result one would expect. At low frequencies, a conductor shows only a real impedance equal to its DC resistance. In contrast, the impedance of a conductor at high frequencies can be approximated by

$$R_{ac} = \omega L_i = R_{dc}\frac{r_0}{2\delta} = R_{dc}\frac{r_0}{2}\sqrt{\frac{\omega\mu\sigma}{2}}. \tag{5.22}$$

Thus both, the real and the imaginary part increase with $\sqrt{\omega}$. This is a very important fact and should be emphasized: Not only the resistance but also the inductive reactance increases. So the impedance can be written as

$$Z = R_{ac} + j\omega L_i = R_{dc}\frac{r_0}{2\delta}(1+j). \tag{5.23}$$

However, the simple high-frequency approximation is only valid for $r_0/\delta \gg 5$. Hence the skin depth must be much smaller than the wire radius. If only Eq. 5.22 is used, it would lead to a DC resistance of zero – which is false. In order to keep the calculation simple but to avoid an error, the DC value is combined with the high-frequency expression [Joh-89]:

$$R = \sqrt{{R_{dc}}^2 + {R_{ac}}^2}. \tag{5.24}$$

The resistance versus frequency is drawn in Fig. 5.5. It is scaled logarithmic for a better illustration. One can see that Eq. 5.24 constitutes a good approximation at both, low and high frequencies.

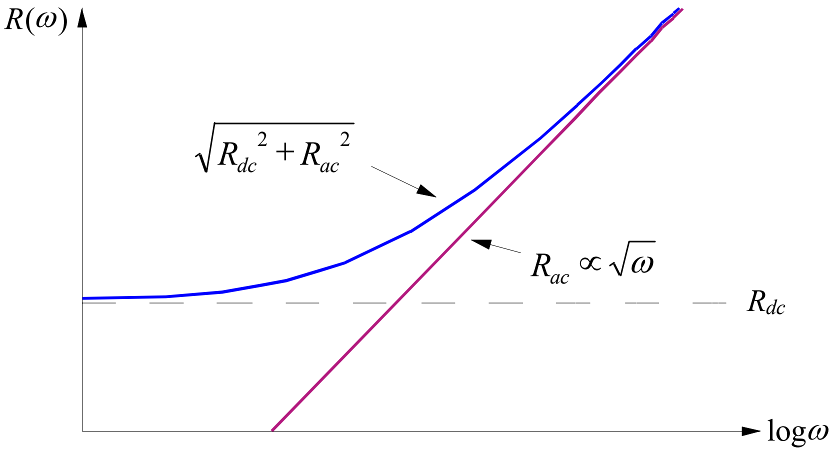

Fig. 5.5 Skin resistance versus frequency.

5.2.2 Dielectric loss

Beside the skin effect, the frequency dependence of the dielectric loss has to be considered. The dielectric loss is often neglected, since the skin effect is dominating. In order to verify this simplification, the attenuation of the transmission line has to be plotted versus frequency and compared with the attenuation only due to the skin effect. The description of the dielectric loss is more sophisticated than the skin effect because of the complex loss mechanisms. In general, it is taken into account by a parallel conductivity G. The first step is to introduce the complex permittivity $\underline{\varepsilon}$

$$\underline{\varepsilon} = \varepsilon' - j\varepsilon'' \tag{5.25}$$

where the real part ε' represents the permittivity of the ideal dielectric and the imaginary part ε'' describes the losses [Sim-89]. Eq. 5.25 is rearranged and leads to

$$\underline{\varepsilon} = \varepsilon'(1 - j\frac{\varepsilon''}{\varepsilon'}) = \varepsilon'(1 - j\tan\delta) \tag{5.26}$$

with the loss angle $\tan\delta$. The capacitance of a transmission line is proportional to $\underline{\varepsilon}$

$$C(\varepsilon) \propto \varepsilon'(1 - j\tan\delta) \tag{5.27}$$

thus the admittance $Y = j\omega C(\varepsilon)$ can be written as

$$Y = j\omega C_0 + \omega C_0 \tan\delta \tag{5.28}$$

where C_0 is the capacity due to the ideal dielectric ε'. The second term in Eq. 5.28 describes the conductance $G(\omega)$, which is now frequency dependent. In a first assumption, the loss angle $\tan\delta$ is assumed to be constant over the interesting range of frequency [Wup-96], [Rie-70]

$$G(\omega) = \omega C_0 \tan\delta = G_{ac} \tag{5.29}$$

which leads to a linear function of ω. The skin effect and the dielectric loss are inserted into Eq. 5.14 and length related units (indicated by an apostrophe) are used:

$$\alpha = \frac{R'_{ac}(\sqrt{\omega})}{2Z_0} + \frac{G'_{ac}(\omega)Z_0}{2} \tag{5.30a}$$

$$\beta = R'_{ac}(\sqrt{\omega}) + \omega\sqrt{L'C'} \tag{5.30b}$$

The dependence of R'_{ac} and G'_{ac} of the frequency ω are added in parentheses. The above equations will be used to describe the cable attenuation of the beam loss system. However, it is not guaranteed that they can be used to model the time domain behavior. The next section will show that this is not the case and a better solution will be derived.

5.3 Transient Simulation of Lossy Transmission Lines

In order to ensure the capability to transmit a high-frequency signal over a long cable, a time domain analysis is valuable. In opposite to the frequency domain, the time domain offers a better way to visualize distortion, time delay or the behavior at different ways of signal encoding. The time domain analysis starts with a characterization in the frequency domain from where the transient behavior will be derived by inverse Fourier and Laplace transform.

5.3.1 Analysis in the frequency domain

The measured attenuation in Fig. 5.3 is used to derive the frequency dependent series resistance (skin effect) and parallel conductance (dielectric loss). Although the series resistance can be calculated by Eq. 5.22, using the measured data leads to much better results. On the one hand, Eq. 5.22 is only a simplified description and the stranded construction of the wire leads to further uncertainties. The calculation is based on the derivation presented in the PSpice library TLINE.LIB. First the attenuation of a 1 km long NG18 was measured at two different frequencies and inserted into Eq. 5.22. Finally, a system of two algebraic equations with the unknown coefficients R_{ac} and G_{ac} has to be solved (see appendix B.1):

Frequency [Hz]	Attenuation [dB/km]	α [-]
$800 \cdot 10^3$	-11.56	0.264
$1.2 \cdot 10^6$	-15.58	0.166

$$R_{ac} = 6.393 \cdot 10^{-5}\ \Omega/\text{m} \cdot \sqrt{\omega}$$
$$G_{ac} = 2.381 \cdot 10^{-12}\ \text{S/m} \cdot \omega$$

The line resistance due to skin effect is calculated according to the theoretical model in Eq. 5.22. With $R_{dc} = 0.037\ \Omega$/m, $r_0 = 0.564$ mm, $\mu = 4\pi \cdot 10^{-7}$ H/m and $\sigma = 56$ S·m/mm^2, the AC resistance would be

$$R_{ac} = R_{dc}\frac{r_0}{2}\sqrt{\frac{\omega\mu\sigma}{2}} = 6.19 \cdot 10^{-5}\ \Omega/\text{m} \cdot \sqrt{\omega}$$

which shows nearly the same result as the derived AC resistance from the cable attenuation. The values R_{ac} and G_{ac} are now inserted in Eq. 5.11 and Eq. 5.30a to compare the calculated attenuation with the measured one for a 1 km long NG18. Figure 5.6 shows an excellent approximation at frequencies up to 2 MHz. Above, the measured and calculated curves differ. This is interesting, since the wave equation should fit the measured data better at high frequencies. Moreover, the calculated AC resistance due to the skin effect agrees very well with the theoretical model. Of course, this model is only an approximation and the stranded construction of the cable influences the skin effect, too. It is assumed that the problem lies in the model of the dielectric loss as it will be shown in the next section.

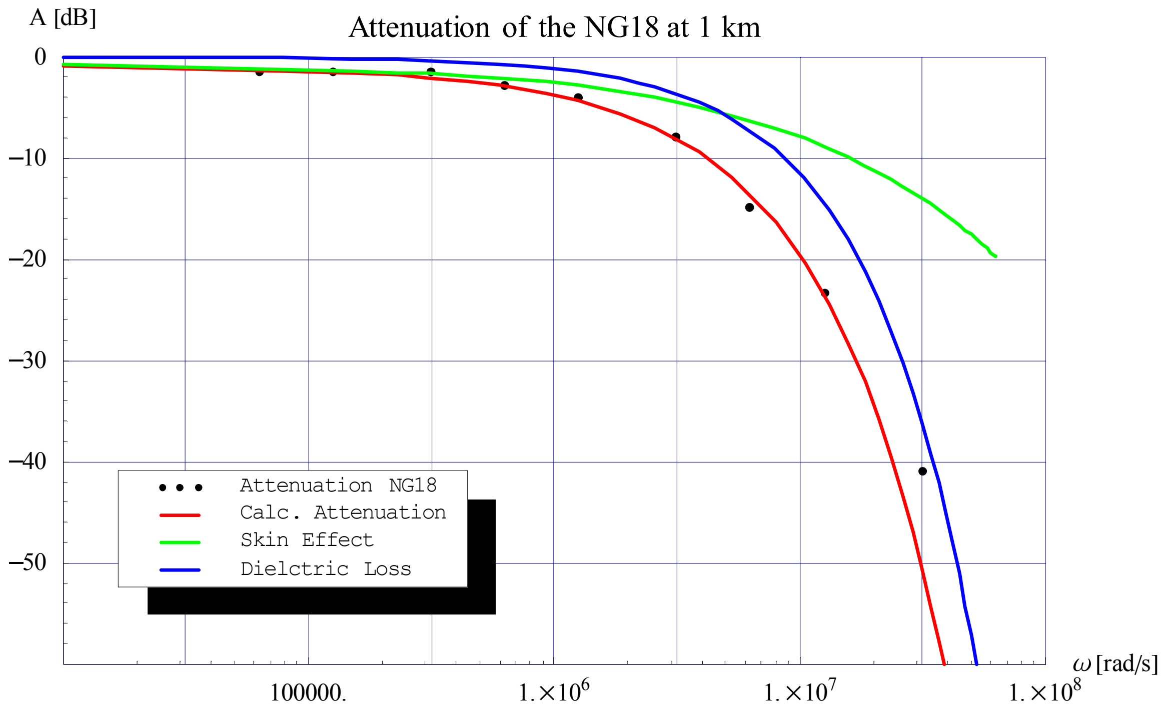

Fig. 5.6 Attenuation of the NG18 due to skin effect and dielectric loss compared with the total attenuation.

The question is now, what kind of information can be derived from the frequency characteristic. Obviously, it is easy to describe the time domain behavior of pure sinusoidal signals, since their spectrum exists only at one particular frequency and distortion doesn't occur. To calculate the rise time t_r of a step function the correlation between the cut-off frequency and the rise time of a lowpass first order is used [Wup-96]

$$t_r = \frac{2.2}{\omega_{3dB}} = \frac{0.35}{f_{3dB}} \tag{5.31}$$

where ω_{3dB} and f_{3dB} are the 3dB cut-off frequencies. The above equation only leads to exact results for a lowpass first order but also provides a good approximation for a higher order lowpass such as a cable. Let us calculate the rise time for a 1.8 km long NG18.

From Table 5.2 the DC attenuation at 1.8 km is 2.67dB. The attenuation has fallen by 3dB to 5.67dB at approximately 65 kHz, thus the rise time would be

$$t_r = \frac{0.35}{65 \cdot 10^3} = 5.38\ \mu\text{s}. \tag{5.32}$$

However, using the measured attenuation after 100 m to derive the attenuation after 1.8 km, leads to a 3dB cut-off frequency of approximately 110 kHz. Consequently the rise time is only 3.18 μs. This value agrees much better with the measured rise time (see section 5.4.3). Thus in the further analysis the attenuation after 100 m is used to derive the attenuation at any other length. To better the accuracy, a time domain analysis has to be performed.

5.3.2 Analysis in the time domain

The time domain gives a much better impression on the distortion of a signal than the frequency domain. Fortunately, both domains are related by the Fourier and Laplace transform: The transfer function $H(j\omega)$ in the frequency domain corresponds to the impulse response $h(t)$ in the time domain. To obtain the transient response $v_2(t)$ of a transmission line, due to an excitation function $v_1(t)$, the following steps are performed:

1. Calculate the cable transfer function $H(j\omega) = e^{-\gamma z}$
2. Multiply the Fourier transform of the excitation function $V_1(j\omega)$ with $H(j\omega)$
3. Compute the inverse Fourier transform to obtain $v_2(t) = \mathcal{F}^{-1}[V_1(j\omega) \cdot H(j\omega)]$

However, the (inverse) Fourier transform must be used carefully to avoid spurious results. A physical, real system distinguishes oneself by two major constraints:

1. The impulse response $h(t)$ must be real and
2. it must be causal, i.e. $h(t < 0) = 0$.

The first constraint emerges from the fact that a physical system must show a pure real response, while the second one claims that the system must not react before it is excited. It can be shown, that a real time function must have an Hermitian frequency spectrum, which can be described by a conjugate complex transfer function

$$H(j\omega) = H(-j\omega)^* \tag{5.33}$$

thus the frequency spectrum of a real signal must have an even real part and an odd imaginary part [Bra-86].

It is not always possible to compute the Fourier transform of a signal analytically. Therefore, a numerical method – the discrete Fourier transform – was used[14]. Since a numerical method

---

[14] In many mathematical programs, this method is implemented as a Fast Fourier Transform (FFT) – a special algorithm that is optmized for calculation speed.

is used, some peculiarities must be considered. First, the input data and the transfer function are sampled with a time interval t_s and a frequency f_s, respectively. According to the sampling theorem, the signal spectrum must be limited to $\frac{f_s}{2}$ (= Nyquist frequency) to avoid aliasing. Therefore, the Nyquist frequency has to be much higher than the maximum frequency of interest. The analytic Fourier transform is calculated over an interval of $-\infty \ldots +\infty$. In contrast, the interval of the discrete Fourier transform is $-\frac{f_s}{2} \ldots +\frac{f_s}{2}$, or $0 \ldots f_s$ if the periodicity of the sampled spectrum is considered [Bra-86]. The following calculations are listed in appendix B.4.

The transfer function has already been determined thus the input signal is examined. The measured input step in Fig. 5.7 shows a fast initial rise but a long, rising tail. The tail emerges from the fact that the cable can't be terminated exactly, since the characteristic impedance is not constant over the whole range of frequencies. At low frequencies – which are responsible for the tail – it is complex (see Eq. 5.9) and the mismatch leads to reflections. Moreover, the cable doesn't behave as a transmission line at low frequencies either. So the line capacitance is slowly charged, which also contributes to the tail. To model the real input step, it is approximated by a step function superposed by an exponential function:

$$V_1(s) = A_{DC}\left(\frac{1}{s} - \frac{k}{s+\tau}\right) \leftrightarrow v_1(t) = A_{DC}(1 - ke^{-t/\tau}) \tag{5.34}$$

where $A_{DC} = 1.85$ is the final amplitude of the input step, $k = 0.2$ the relative portion of the final amplitude that is described by the exponential function and $\tau = 8$ μs the time constant.

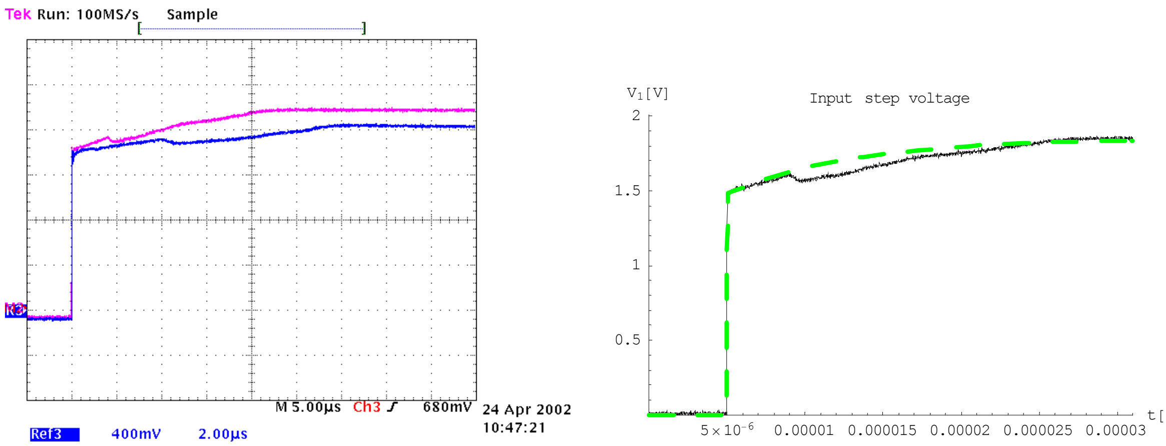

Fig. 5.7 Actual input step of the NG18. Left: Measured step voltage at 1 km (blue, 2 μs/div) and 1.8 km (magenta, 5 μs/div). Right: Model of the nonideal input step at a cable length of 1.8 km with a step function and a superposed exponential function.

Now the time domain response due to the real step function, described by Eq. 5.34 is computed. The transfer function $H(j\omega)$ is described by Eq. 5.11 with α and β according to Eq. 5.30.

It can be proven that the spectrum is not Hermitian, thus violating the first constraint. To make the real part even, G_{ac} is modified to

$$G_{ac} = |\omega|\, C'_0 \tan\delta \tag{5.35}$$

by using the modulus of ω in the dielectric loss. A Mathematica file was written to calculate the impulse and the step response. The input variables are the line parameters R'_{ac}, L', C', G'_{ac}, the length of the cable z and the sample frequency f_s. Figure 5.8 depicts the impulse response and the step response, for a 1.8 km long NG18. Both pictures show a noncausal behavior. The time delay of the line was calculated as $\frac{z}{\sqrt{L'C'}} = 10.62\ \mu$s, but the system reacts before the electromagnetic wave of the excitation reaches the end of the line.

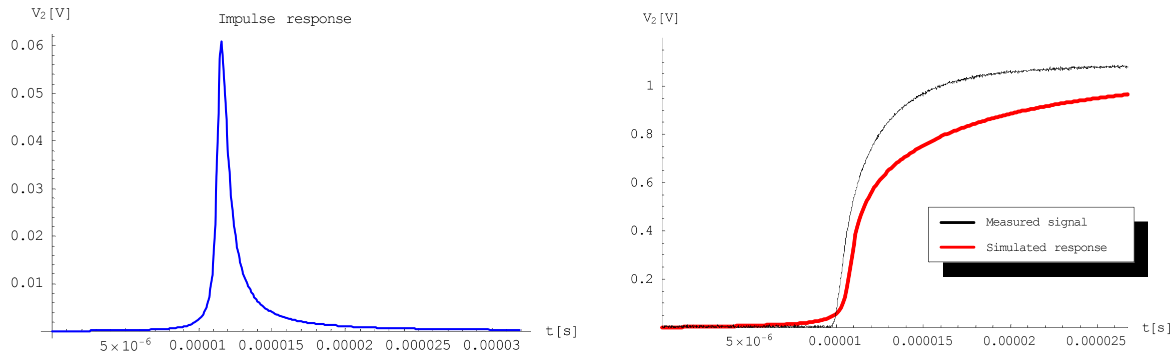

Fig. 5.8 Impulse and step response according to the model in Eq. 5.30 after 1.8 km. Left: Impulse response. Right: The measured step response is compared with the simulated one.

Thus the model derived in section 5.2 seems to be not appropriate for a time domain analysis. For a better understanding of the loss mechanisms, they are divided into skin effect and dielectric loss. Moreover, the transfer function is reduced to a phase minimum system by neglecting the time delay of the cable, which is $e^{-j\sqrt{L'C'}z}$. With Eq. 5.30, the transfer function only due to the skin effect is

$$V_S = e^{-\frac{R'_{ac}(\sqrt{\omega})}{2Z_0}(1+j)\cdot z} \tag{5.36}$$

while the transfer function due only because of the dielectric loss reads

$$V_D = e^{-\frac{G'_{ac}(|\omega|)Z_0}{2}\cdot z}. \tag{5.37}$$

The DC attenuation is not taken into account in the above equations. It would be a constant factor and can be added afterwards. The impulse and step response due to the skin effect and the dielectric loss are now calculated separately.

Skin effect only

To simplify Eq. 5.36, $(1+j)$ is substituted by $\sqrt{2j}$ and the correlation $s = j\omega$ between the Laplace and the Fourier transform is used:

$$V_s = e^{-\frac{R'_{ac}(\sqrt{s})}{\sqrt{2}Z_0}\cdot z} \propto e^{-A\sqrt{s}}. \tag{5.38}$$

The impulse response is found by the inverse Laplace transform using the formulas [Gar-87], [Rie-70]

$$e^{-A\sqrt{s}} \longleftrightarrow \frac{Ae^{-\frac{A^2}{4t}}}{2\sqrt{\pi}t^{\frac{3}{2}}} \tag{5.39}$$

and the ideal step response is

$$\frac{1}{s}\cdot e^{-A\sqrt{s}} \longleftrightarrow \mathrm{erfc}(\frac{A}{2\sqrt{t}}) \tag{5.40}$$

which describes a complementary error function. Thus the step response of a cable considering only the skin effect leads to a physical, real signal. Figure 5.9 shows the impulse and step response of a 1.8 km long NG18. The step response is compared with the measured signal.

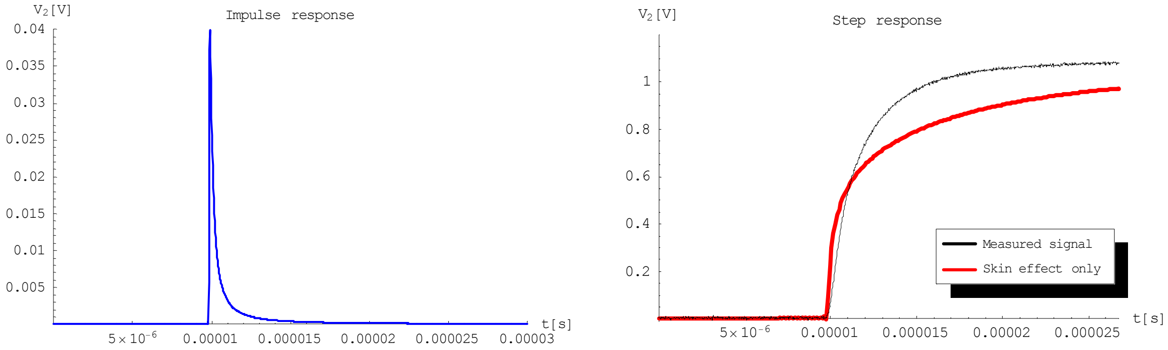

Fig. 5.9 Impulse and step response only due to the skin effect after 1.8 km. Left: The impulse response is causal. Right: Comparison of the measured and the calculated step response.

The step response shows a faster rise than the measured signal because the attenuation regarding only the skin effect is less than the real attenuation of the cable. The deviation at longer time intervals is quite large. This is mainly because of the limited validity of the used model. The skin effect was derived from a high-frequency approximation – which doesn't describe the behavior of a line at low frequencies. Nevertheless, the skin effect leads to a causal model, which was expected since it can be derived directly from Maxwell's equations. Thus if the dielectric loss can be neglected, which is often the case, the output signal of a terminated cable can be found from Eq. 5.38. However, the accuracy at low frequencies has to be verified. Regarding the attenuation plot of the NG18, the dielectric loss must not be neglected, thus it is examined more thoroughly.

Dielectric loss only

In section 5.2.2 the dielectric loss was modeled as a linear function of ω, which lead to a noncausal response. There are two reasons for this behavior. First, no causal network can have an attenuation that increases equal or faster than $e^{-k|\omega|}$, which corresponds to the attenuation due to the dielectric loss (Eq. 5.37). This would violate the Paley-Wiener criterium [Cur-85]. The second reason is the Hermitian character of a real, causal transfer function. A pure real transfer function $e^{-k|\omega|}$ can't result in a real time domain response. One might argue that the division into skin effect and dielectric loss is only a simplification – which is true – but even considering the exact wave propagation in Eq. 5.11 and the exact expression for γ in Eq. 5.7, will not eliminate the noncausality. In order to solve this dilemma, [Cur-85] developed a causal model. The authors claim that the function $e^{-k|\omega|}$ only describes the real part of a complex transfer function. The real and imaginary part of a transfer function are related through the Hilbert transform. Thus if one part is known, either the real or the imaginary part, the other one can be calculated by the Hilbert transform. Moreover, the impulse response $h_D(t)$ can be found only by the real part with the Fourier cosine transform, which leads to

$$h_D(t) = \frac{2}{\pi} \int_0^{\infty} e^{-k|\omega|} \cdot \cos(\omega t)\, d\omega = \frac{2k/\pi}{k^2 + t^2} u(t) \tag{5.41}$$

and by convolving $h_D(t)$ with the unit step function $u(t)$ the step response is

$$v_D(t) = \int_{-\infty}^{t} h_D(t-\tau)\, d\tau = \frac{2}{\pi} \arctan(\frac{t}{k})\, u(t). \tag{5.42}$$

The same result could be found by applying the Fourier sine transform on the imaginary part of the transfer function. In order to describe the complete step response due to skin effect and dielectric loss, the step response due to the skin effect has to be convolved with the impulse response in Eq. 5.41. Figure 5.10 shows the measured step response after 1.8 km of NG18 compared with the step response from Fig. 5.9 and with the response, including the dielectric loss according to Eq. 5.41 (see appendix B.4).

Taking the dielectric loss into account leads to a better description at high frequencies. At low frequencies, however, the deviation is too large. In addition, the description according to [Cur-85] lacks in terms of a correct, physical model of the dielectric loss, thus further investigations have been made.

The key point is that the linear dependence of the dielectric losses of ω seems to be false. A more detailed description of the conductivity in dielectric materials is presented by [Gar-87].

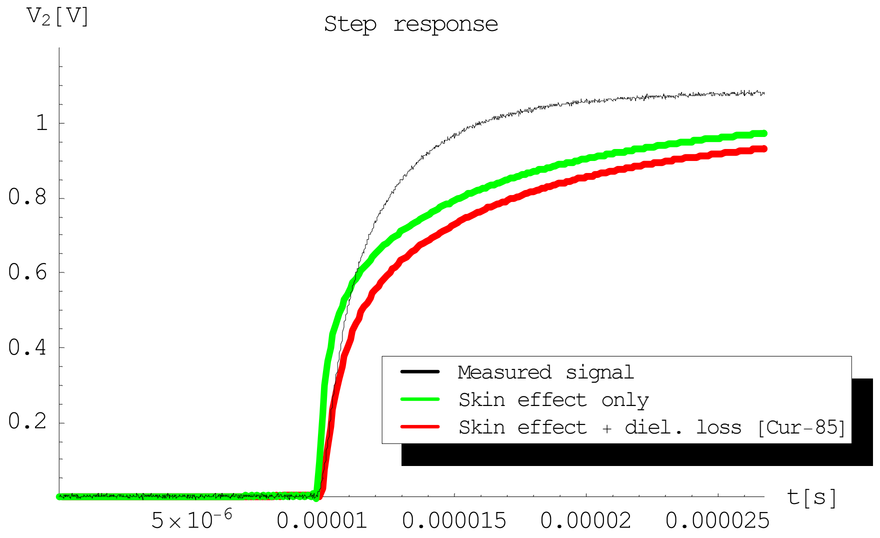

Fig. 5.10 Step response after 1.8 km taking the dielectric loss into account, according to [Cur-85].

Similar to the relation between the real and imaginary part of a transfer function (Hilbert transform), the real and imaginary part of the dielectric permittivity, $\varepsilon(\omega)'$ and $\varepsilon(\omega)''$, are connected by the so called Kramers-Kronig relations. According to these equations, a constant real part $\varepsilon(\omega)'$ must lead to an imaginary part that is a function of $1/\omega$ – and not constant as assumed until now . Therefore, the dielectric model must be refined to obtain a causal behavior. In [Jon-77] different loss mechanisms are described and a 'universal law of dielectric response' is presented. According to that theory, the imaginary part of the dielectric susceptibility $\chi''(\omega)$ follows

$$\chi''(\omega) \propto \omega^{m-1} \quad \text{with } m < 1 \tag{5.43}$$

where the exponent m depends on the material and lies between 0.5 and 1, a typical value is 0.8. The model of [Jon-77] was picked up by [Vei-88] and [Vir-91] who included it into APLAC, a object-oriented analog circuit simulator at the Helsinki University of Technology. The following formulas rely on their work.

The remarkable property of Eq. 5.43 is, that according to the Kramers-Kronig relations, the real and imaginary part of $\chi(\omega)$ – and $\varepsilon(\omega) = \chi(\omega) + 1$ – are of the same form. Hence the dielectric permittivity is

$$\varepsilon(\omega) = \varepsilon(\omega)' - j\varepsilon(\omega)'' \propto (j\omega)^{m-1} \tag{5.44}$$

and the dielectric loss admittance can be expressed as

$$Y_D(j\omega) = G_{dc} + C_D(j\omega)^m \tag{5.45}$$

where G_{dc} equals the DC conductance and C_D is a normalized capacitance. As a further assumption, G_{dc} will be neglected since it is much smaller than the frequency dependent dielectric loss. Now the loss angle $\tan\delta$ is incorporated into Eq. 5.45 and length related units are used

$$Y'_D(j\omega) = j\omega C' \cdot \tan\delta \cdot (j\omega\tau)^{m-1} \tag{5.46}$$

with the distributed cable capacitance C' and a normalized time constant τ. This time constant can be found by comparing the real part of Eq. 5.45 with the conventional loss admittance in Eq. 5.29 at a certain frequency $\omega = \omega_t$, resulting in

$$\tau^{m-1} = \frac{{\omega_t}^{1-m}}{\cos(\frac{m\pi}{2})}. \tag{5.47}$$

which ensures the correct attenuation at $\omega = \omega_t$ – a statement which leaves some questions open. Nevertheless, the same result is also presented by [Cur-85] who cites the original work, done by [Nah-62]. Finally, the admittance of a transmission line, according to Fig. 5.4 can be written as

$$Y' = j\omega C' + \underbrace{(j\omega)^m C' \tan\delta\, \tau^{m-1}}_{G'(j\omega)} \tag{5.48}$$

which leads to a wave propagation factor γ of

$$\gamma = \sqrt{(R' + j\omega L') \cdot (j\omega C' + G'(j\omega)}. \tag{5.49}$$

The computation of τ^{m-1} and $\tan\delta$ is shown in appendix B.3. The cable attenuation is plotted in Fig. 5.11 to compare the measured attenuation with the above model and the conventional loss model in section 5.2.2. The modified loss model shows an excellent agreement with the measured attenuation.

Again, the impulse and step response due to the propagation factor in Eq. 5.49 are calculated for a 1.8 km long NG18 (see appendix B.4) and are presented in Fig. 5.12. The picture shows a causal behavior and a good approximation at high frequencies. Unfortunately, at longer time intervals the deviation becomes quite large. Thus the derived model is not suitable to describe a step response but could be envisaged to describe modulated signals with a limited lower bandwidth, such as Manchester Code. All presented models showed a large deviation at low frequencies. To resolve this problem a refined, mathematical description would be needed. This would go beyond the scope of this thesis, thus a more practical model was derived.

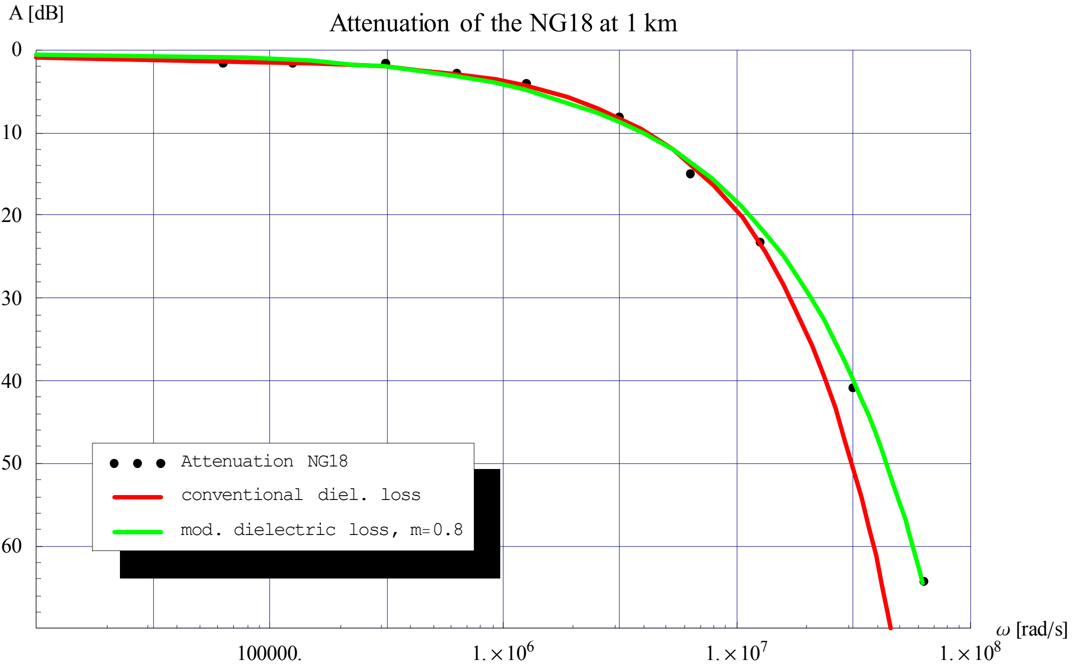

Fig. 5.11 Attenuation with modified dielectric loss. The conventional dielectric loss assumes $V_D \propto e^{-k|\omega|}$, while the modified dielectric loss uses $V_D \propto e^{-k(j\omega)^m}$.

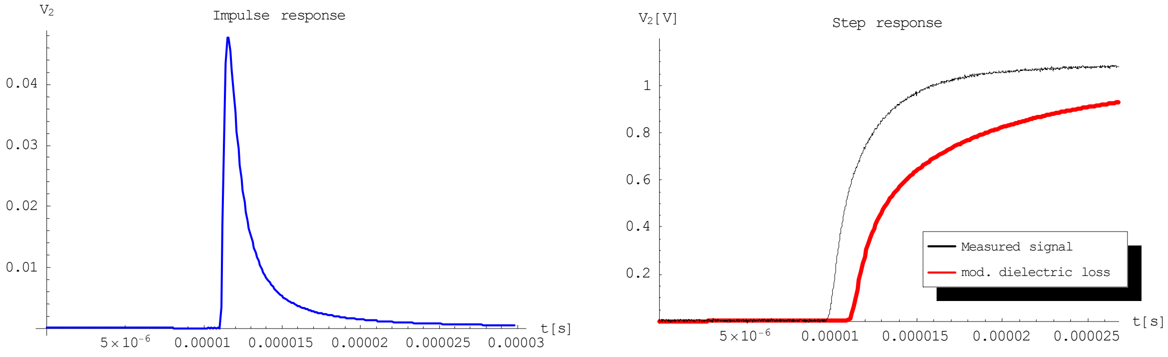

Fig. 5.12 Causal time domain model of a transmission line with modified dielectric loss after 1.8 km. Left: Impulse response. Right: The simulated step response is compared with the measured one. The calculated time delay is slightly larger than the measured delay.

Transfer Function with Nonlinear Fit

The above calculations of the time domain behavior of transmission lines revealed a sophisticated mathematical model. A more straightforward treatment of this topic is found in [Gru-81] and [Ngu-94]. The authors developed a transfer function approximation that fits the bode plot of the cable attenuation to compute the time domain response. The modulus squared of a rational function can be written as

$$|H(j\omega)|^2 = \frac{(\omega^2 + {z_1}^2)(\omega^2 + {z_2}^2)...(\omega^2 + {z_n}^2)}{(\omega^2 + {p_1}^2)(\omega^2 + {p_2}^2)...(\omega^2 + {p_n}^2)} \tag{5.50}$$

where z_n describes the zeros and p_n the poles of $H(j\omega)$. Consequently, the attenuation of the cable is approximated by $|H(j\omega)|$. For that task, the nonlinear least square algorithm of Mathematica was used (see appendix B.2). The accuracy of the fitted transfer function greatly depends on the number of zeros and poles as well as on the appropriate choice of the start values for the algorithm. A long cable shows a steep fall off at high frequencies, demanding a larger number of poles. If the cable is shorter, the attenuation declines much slower and needs pole-zero pairs to generate a slope more flat than -20 dB per decade.

Another important point is the stability and the time delay of the transfer function. The stability of the system allows only poles in the left half of the s-plane. Since the zeros and poles in Eq. 5.50 are squared, these constraint can easily be achieved by using only the negative solutions. The attenuation plot doesn't take the time delay of the cable into account. Thus it has to be added manually by $e^{-j\sqrt{L'C'}z}$.

Again, a 1.8 km long NG18 was taken to calculate the time domain response. Figure 5.13 shows the measured attenuation versus frequency compared with the fitted rational function. Four poles were sufficient to approximate the attenuation accurately. The fit function is not stated in the pole-zero form but with the cut-off frequencies for each pole:

$$H(j\omega) = A_{DC}\frac{1}{(1+j\frac{\omega}{\omega_{p1}})(1+j\frac{\omega}{\omega_{p2}})(1+j\frac{\omega}{\omega_{p3}})(1+j\frac{\omega}{\omega_{p4}})} \tag{5.51}$$

where A_{DC} is the DC attenuation. The modulus can be obtained by

$$|H(j\omega)| = A_{DC}\sqrt{\frac{1}{(1+(\frac{\omega}{\omega_{p1}})^2)(1+(\frac{\omega}{\omega_{p2}})^2)(1+(\frac{\omega}{\omega_{p3}})^2)(1+(\frac{\omega}{\omega_{p4}})^2)}}. \tag{5.52}$$

The fit was performed with Mathematica and results in the following cut-off frequencies:

$$\begin{aligned} \omega_{p1} &= 9.089 \cdot 10^5 \text{ rad/s}, \ \omega_{p2} = 9.342 \cdot 10^6 \text{ rad/s}, \\ \omega_{p3} &= 9.389 \cdot 10^6 \text{ rad/s}, \ \omega_{p4} = 9.391 \cdot 10^6 \text{ rad/s}. \end{aligned} \tag{5.53}$$

The impulse and step response in Fig. 5.14, after 1.8 km NG18, are computed with a numerical Fourier transform (see appendix B.4) but could also be found by an analytical inverse Laplace transform with the help of partial fractions. The delay of 10.6 μs is also taken into account. The right picture illustrates the influence of the nonideal step. An ideal step leads to a remarkable deviation from the measured curve (blue curve). Taking the real step into account, yields to accurate results (red curve).

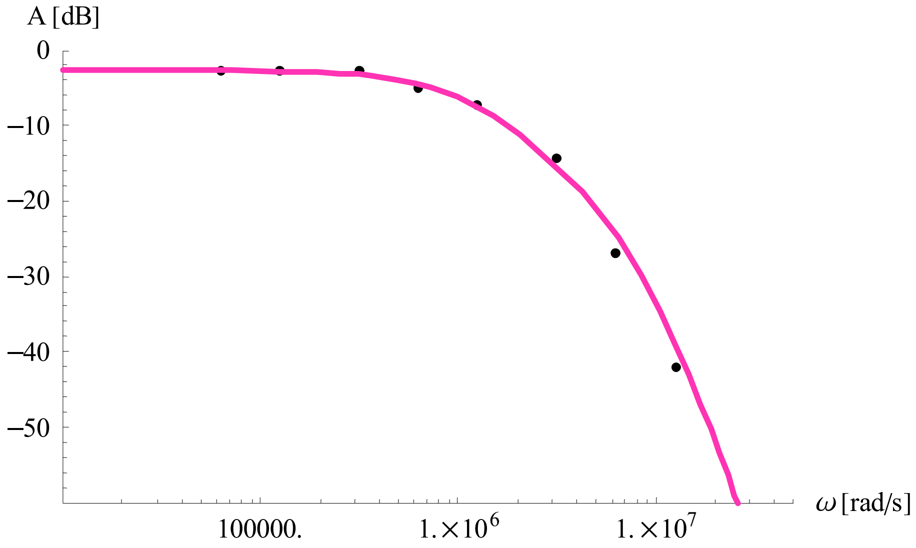

Fig. 5.13 Nonlinear lest square fit of the cable attenuation after 1.8 km with a rational transfer function.

The transfer function approximation leads to a simple mathematical model of the cable and less calculation effort. Because of the good results it is used in the further optimization of the signal transmission.

Scaling Laws

Very often, the rise time of a signal has been measured at a certain cable length and predictions have to be made, if the length or the data rate is modified or if the wire size is changed. This can be done without going again through the calculations by considering some scaling laws. The major fact is that the rise time of a signal depends on the attenuation coefficient $\alpha(\omega)$, which can be written similar to Eq. 5.30a as

$$\alpha(\omega) = (\frac{R'_{ac}}{2Z_0}\sqrt{\omega} + \frac{G'Z_0}{2}\omega^m) \cdot z \tag{5.54}$$

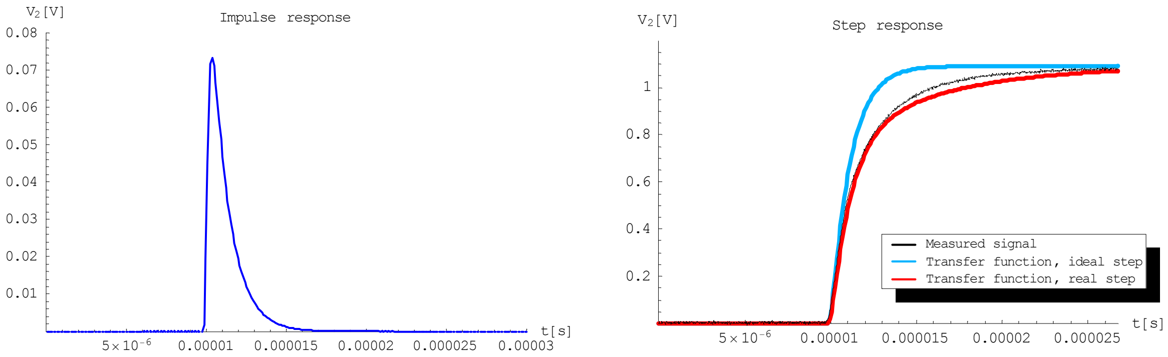

Fig. 5.14 Impulse and step response due to the transfer function approximation after 1.8 km. Left: Impulse response. Right: Comparison of the simulated step response with the measured one. The influence of the nonideal step is shown, by comparing the blue (ideal step) and the red curve (nonideal step).

where G' represents now the real part of $G'(j\omega)$ in Eq. 5.48 with the frequency ω^m stated explicitly. If the cable is dominated by the skin effect, the attenuation coefficient is proportional to $\sqrt{\omega}$. Thus if the length z is doubled, the frequency ω must be decreased by four to keep $\alpha(\omega)$ unchanged. Therefore the rise time (= data rate) is proportional to $\frac{1}{z^2}$. If the attenuation is mainly due to the dielectric loss, which is proportional to ω^m, the rise time would be degraded by a factor of $\frac{1}{2^{1/m}}$. At $m = 0.8$ the rise time would be reduced to 42% compared with the 25% at skin effect. For the NG18, the attenuation is mainly due to the dielectric loss, thus the rise time is a function of $\frac{1}{z^{1/m}}$.

The characteristic impedance also affects the attenuation. A larger Z_0 reduces the attenuation of the skin effect but increases the attenuation due to the dielectric loss. Anyway, this value is fixed for the cable installation to $Z_0 = 110\ \Omega$.

If Eq. 5.17 is rearranged, one will find that the AC resistance R_{ac} is proportional to the square root of the DC resistance $R_{ac} \propto \sqrt{R_{dc}}$, thus doubling the diameter of a wire, would decrease the rise time by the same factor. However, a larger diameter means higher cable costs and more space for the installation. So it is commonly not appreciated to push up the data rate just by increasing the diameter.

To determine the influence of the line length on the data rate, a square wave was transmitted over the cable at different length. The frequency was adjusted to obtain a peak-peak amplitude of 200 mV at the receiver side. Figure 5.15 depicts the results, while the measurement setup was the same as in Fig. 5.2.

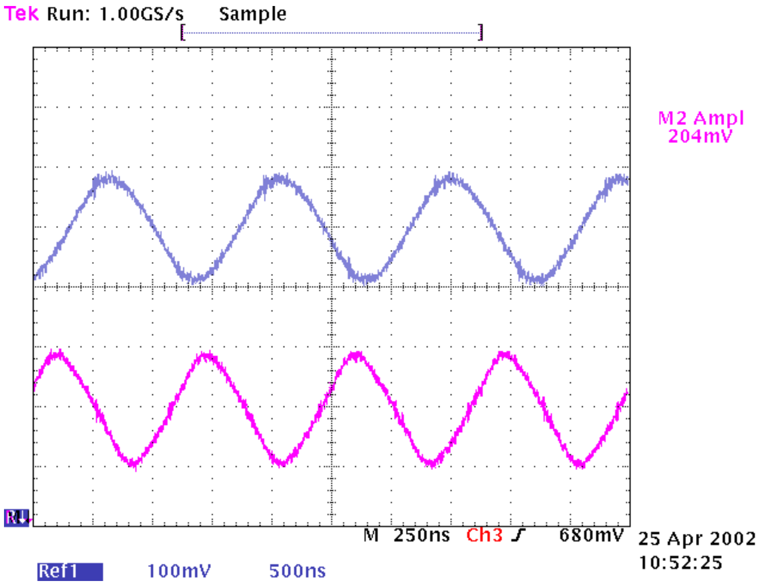

Length	f_{max}
1800 m	700 kHz
1400 m	950 kHz
1000 m	1.6 MHz

Fig. 5.15 Influence of the cable length on the signal amplitude and rise time. Left: The max. frequency for 200 mV_{pp} is 700 kHz at 1800 m (top, 500 ns/div) and 1.6 Mhz at 1000 m (bottom, 250 ns/div). Right: Frequency to gain 200 mV_{pp} at different cable lenghts.

The ratio of the maximum frequency after 1000 m and 1800 m is 2.29, while the length differ only by a factor of 1.8. The ratio of the maximum frequency (data rate, rise time) Δn and the corresponding ratio of length Δz are related by the following equation (according to the theoretical model in Eq. 5.54):

$$\Delta n = \frac{1}{\Delta z^x} \tag{5.55}$$

The measured values of Fig. 5.15 for 1000 m and 1800 m lead to

$$x = -\frac{\ln \Delta n}{\ln \Delta z} = -\frac{\ln(1.6/0.7)}{\ln(1/1.8)} = 1.41. \tag{5.56}$$

The maximum data rate of a 2 km long cable can be calculated if only a length of 1.8 km is available. With $x = 1.41$, the ratio in data rate between 1.8 km and 2 km is

$$\frac{1.8}{2}^{1.41} = 0.86. \tag{5.57}$$

This value will be used in the following section.

5.4 Signal Transmission Techniques

The performance of a data transmission system doesn't only depend on the properties of the cable but also on other facts, such as

- Data en- and decoding
- Driver / receiver combination
- Cable termination
- Crosstalk and other external interference
- Line equalization
- Data synchronization

A block diagram of a typical digital data transmission system is shown in Fig. 5.16. However, it need not contain all the elements that are illustrated. A multiplexer transforms several data channels into one single channel. Often, the data is encoded into a more suitable form for the transmission. It will be shown that the appropriate encoding not only increases the data rate but also helps to avoid transmission errors. In some cases, equalizers are used to shape the signal, which is distorted and attenuated by the transmission medium. They can be installed at the transmitter and/or the receiver side. As mentioned in section 5.2, a terminated cable behaves like an ohmic resistor equal to its characteristic impedance. In order to drive that low impedance load, a line driver is used. It has a high bandwidth to amplify the signal without distortion and is able to supply a high output current. A receiver amplifies the attenuated signal and performs additional functions, such as the substraction of differential signals at balanced transmission. The regenerator, often a simple treshold comparator, restores the fast edges of the digital data. There are also many cases where driver and receiver are not synchronized. The synchronizer aligns the received data to the local clock. Some codes, such as Manchester Code, even contain the clock information in the data pattern itself. A decoder creates the original digital bit pattern and the demultiplexer extracts the particular channels.

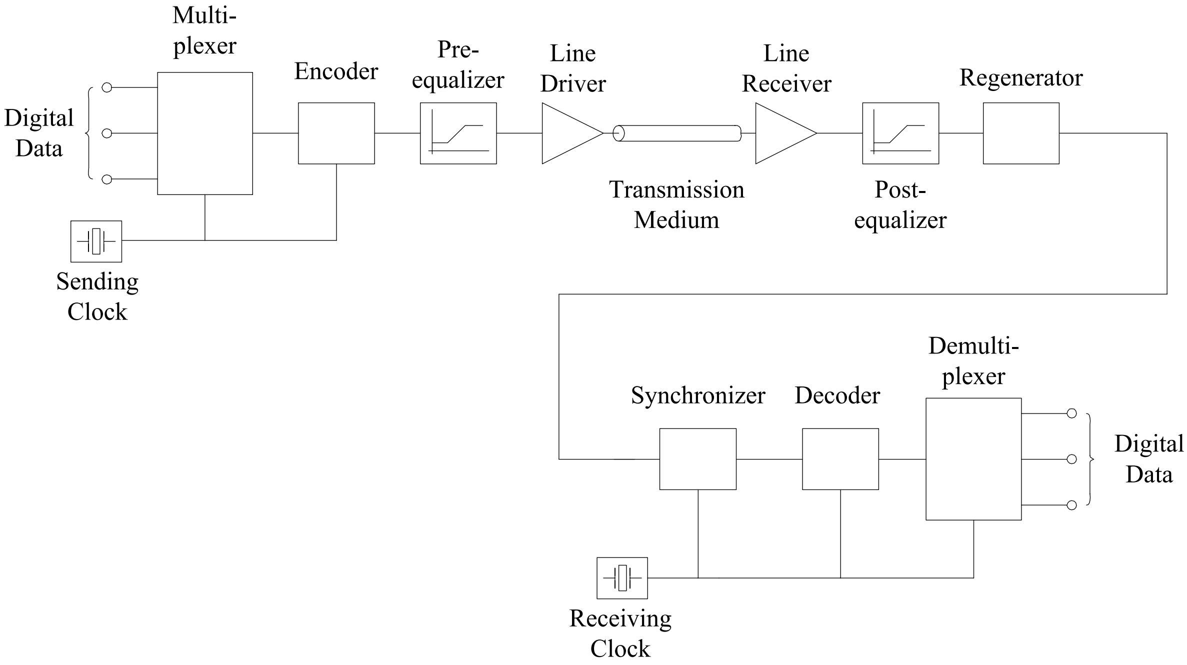

Fig. 5.16 Block schematic of a typical digital data transmission system.

The data transmission system for the readout electronics of the beam loss monitors is very similar to that in Fig. 5.16. The driver side is presented in Fig. A.5, while the receiver side is shown in Fig. A.6.

5.4.1 Data encoding and multiplexing

Encoding the signal is not only necessary to increase the amount of information which can be transmitted but also to avoid transmission errors. A normal digital bit sequence will be distorted like in Fig. 5.17 a). Aside the degradation of the rise time, the average value of the signal will change in dependence of the duty cycle. To regenerate the digital data, a comparator is used. If its treshold V_{Th} is set to 50% of the amplitude, as it is often done, the worst case would be a long period of consecutive zeros or ones like in Fig. 5.17 b). Here the treshold is not reached at the first two pulses after a long period of zeros. Therefore, DC-free codes or codes with a constant DC value are aspired.

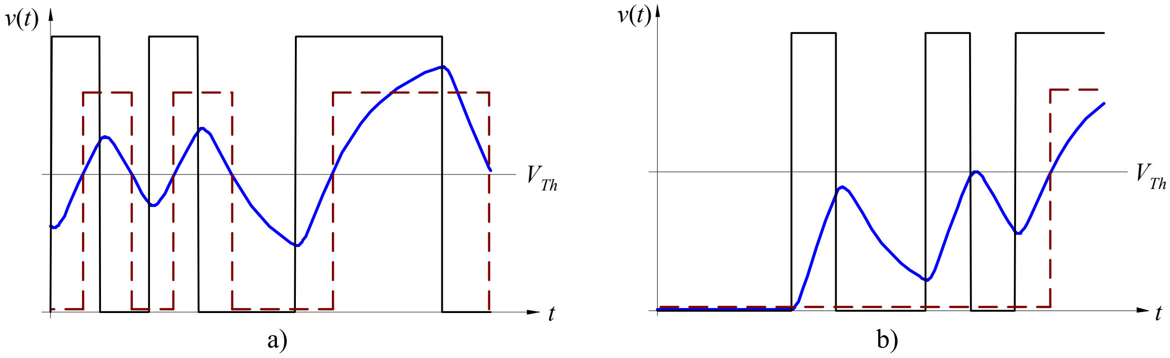

Fig. 5.17 Signal distortion at different duty cycles: a) The signal is distorted but hits the treshold because of the high duty cycle. b) The same data rate but with a long period of leading zeros; the treshold is missed at the first two pulses.

Therefore, the Manchester Code in Fig. 5.18 a) was chosen. A logic one is encoded as a high-low transition, whereas a logic zero is encoded as a low-high transition. The advantage is that the number of zeros and ones are equal, independent of the binary information to transmit. Another useful property of this code is the possibility to detect errors. A correctly transmitted bit always contains a transition in the middle of the bit and might have a transition at the beginning or at the end, depending on the following and preceding logic state. This behavior can be used to implement an error detection. Unfortunately, the advanced performance of the Manchester Code is paid with twice the frequency that has to be transmitted compared to the pure logic signal. Figure 5.18 b) shows the same input signal as in Fig. 5.17 b) but now Manchester encoded. The long period of consecutive zeros or ones is not critical because the DC value is held constant at the treshold. However, the higher frequency of the Manchester Code states a problem. The signal needs a certain time to settle around the average value. This can be observed especially at the last transition of Fig. 5.17 b). Thus the data rate is limited, too.

The basic setup of the front end frequency evaluation has already been presented in section 4.3.2. Now, the realization of the circuit is shown. Six channels are multiplexed and transmitted serially over a twisted pair. The front end circuit is placed on a VME card in the tunnel. Figure 5.19 shows the proposed setup of a complete front end card. It comprises six front end channels, each equipped with a counter and a shift-register. Whenever the CFC is reset, the counter is incremented. One count equals the charge $Q_{ref} = I_{ref} \cdot \Delta T$. Thus from the number of reset pulses per time interval the average input current during this time interval

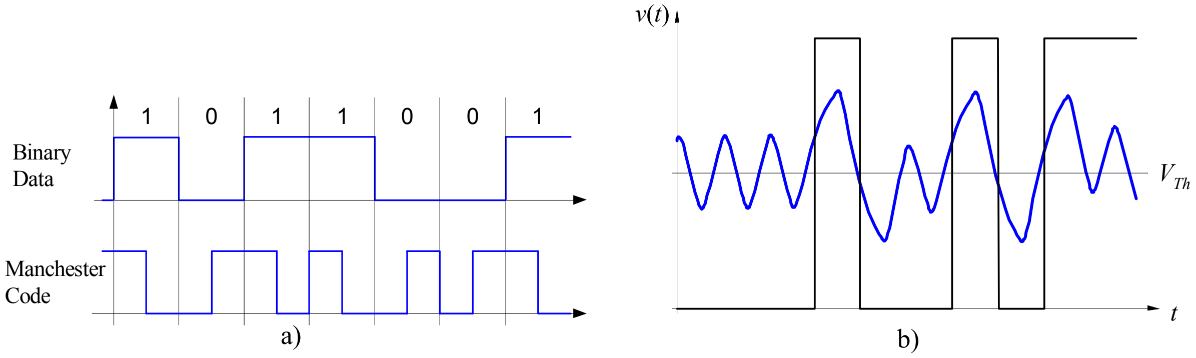

Fig. 5.18 Manchester Code offers a high duty cycle: a) Principle of the Manchester Code; a logic one is encoded as high-low transition and a logic zero as low-high transition. b) The same signals as in Fig. 5.17 b) but now in Manchester Code.

can be derived. According to section 2.3 the losses in the LHC need not to be acquired faster than one turn because of the trigger mechanism of the beam dump kicker magnet. However, the counters are read out every 40 μs (= 25 kHz), in order to get at least two acquisitions per turn. At the maximum nominal frequency of 5 MHz, the CFC produces 200 counts in 40 μs. Since the output frequency at overload is limited to 6 MHz, the maximum number of counts per readout interval is 240. Thus 8-bit counters are sufficient. The counters are never reset, so the difference between two consecutive counter values must be calculated to determine the actual beam loss. To transmit the data, the counter values are loaded into parallel-to-serial shift registers, which are connected in series. An additional register generates the frame alignment word (FAW) that marks the beginning of a new data frame (see Encoder Design). The encoder itself generates the Manchester Code and loads the counter values into the shift registers.

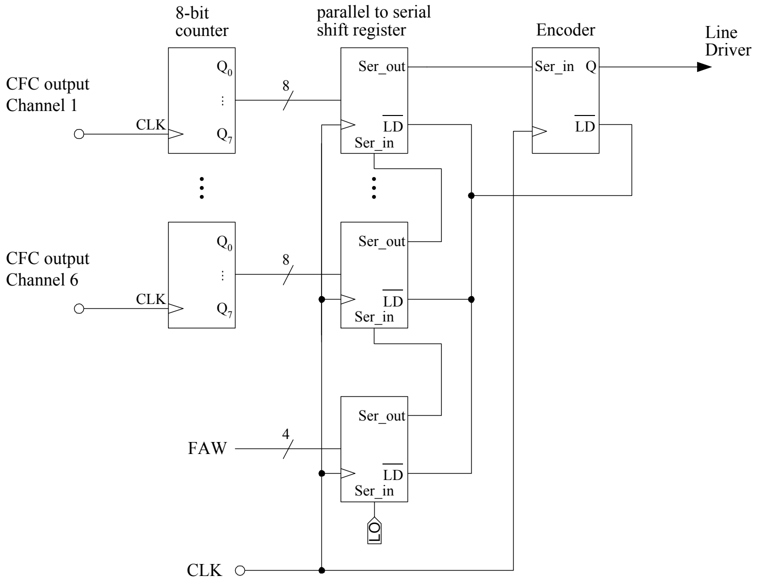

Fig. 5.19 Readout schematic of the CFC.

Finally, the Manchester encoded data is transmitted to the surface. One of the first things, which has to be figured out, is the structure of the bit stream. It has to be determined which kind of information will be transmitted, at which data rate and at which position will the corresponding bit be placed.

Encoder Design

Before the signal can be transmitted, it has to be encoded into Manchester Code and the FAW has to be attached. The data encoding itself seems to be straight-forward at the first sight, since the logic conjunction between the clock and the Manchester Code can be described by an exclusive or (XOR). Unfortunately, timing issues make the task a bit more complicated. Figure 5.20 a) shows the encoded signal with a simple XOR gate. At the change of a logic state, short spikes occur because of the finite rise and fall time of the data (and the clock). To avoid these spikes, the circuit in Fig. 5.20 b) is used. It runs with twice the nominal clock frequency and samples the output of the XOR gate in the first and third quarter of a bit, where the logic state is stable.

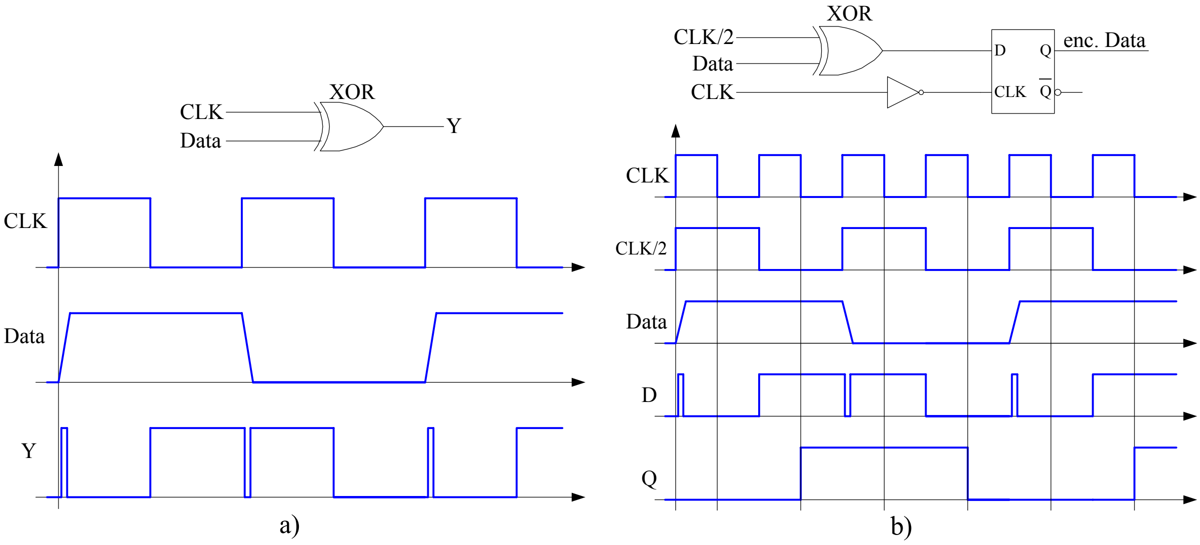

Fig. 5.20 Manchester encoder: a) Simple XOR gate introduces spikes. b) Improved circuit avoids the spikes but needs twice the clock frequency.

The second task is the selection of an appropriate FAW. It is used to synchronize the receiver and to mark the beginning of a new data frame. Once the FAW has been recognized, the following bits are evaluated according to the chronological built up of the data stream. After the six channels are transmitted, another FAW is sent. Unfortunately, the FAW can't be chosen uniquely, if it consists of an arbitrary bit pattern. There is a certain probability that it will occur in the data. Even if the FAW is checked again only after the predetermined number of bits is transmitted, a misalignment can't be excluded.

To overcome this problem, the property of Manchester Code is used to create an FAW that cannot occur in the data pattern. Even in the case of an external bit corruption, an exact reproduction would be so rare that the probability of misalignment was neglected. Figure 5.21 shows the FAW followed by arbitrary data. It consists of a 4-bit word, where the first two bits are high while the last two are low. However, the FAW is not encoded and the logic states are transmitted. Because of its structure, the DC level remains at 50%.

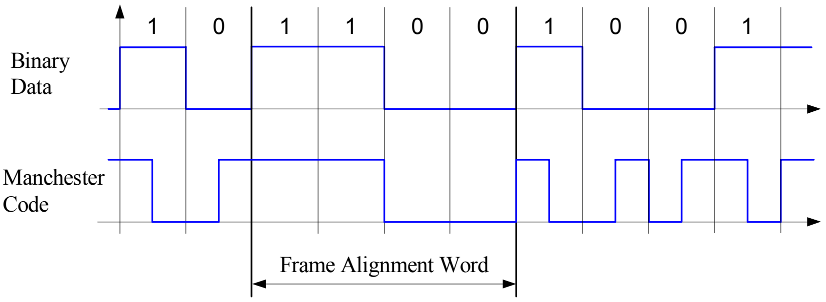

Fig. 5.21 The FAW – 1100 – is not encoded thus it can't occur in the data and doesn't change the DC average value.

The encoder and the readout command for the registers were implemented in a GAL20V8[15] as illustrated in Fig. 5.22. To simplify the development, only two channels were realized together with the FAW register. First the double clock must be divided by two with a D flip-flop, to generate the appropriate clock for the registers and the GAL. A state machine, consisting of a 5-bit counter, provides the parallel load command for the registers (/PL) and disables the encoding of the FAW (Dec_En). The total length of a frame is 20 bits ($= 2 \cdot 8 + 4$), hence the counter counts until 20 and loads the new counter values into the registers. Then, the first four bits (= FAW) are not encoded by setting Dec_En = 0. The encoding itself is done by an XOR conjunction between the clock and the serial data (Ser_Out). However, the output of the XOR gate (Pre_Code) contains undesired spikes. Thus the second D flip-flop removes these spikes as already shown in Fig. 5.20 b). The complete circuit of the encoder is presented in Fig. A.3.

The data rate is calculated by dividing the number of bits that are transmitted in one frame by the readout period of 40 μs. Considering six channels, each with eight bits, and the FAW,

---

[15] GAL = Gate Array Logic, further details can be read in the GAL20V8 datasheet from Lattice.

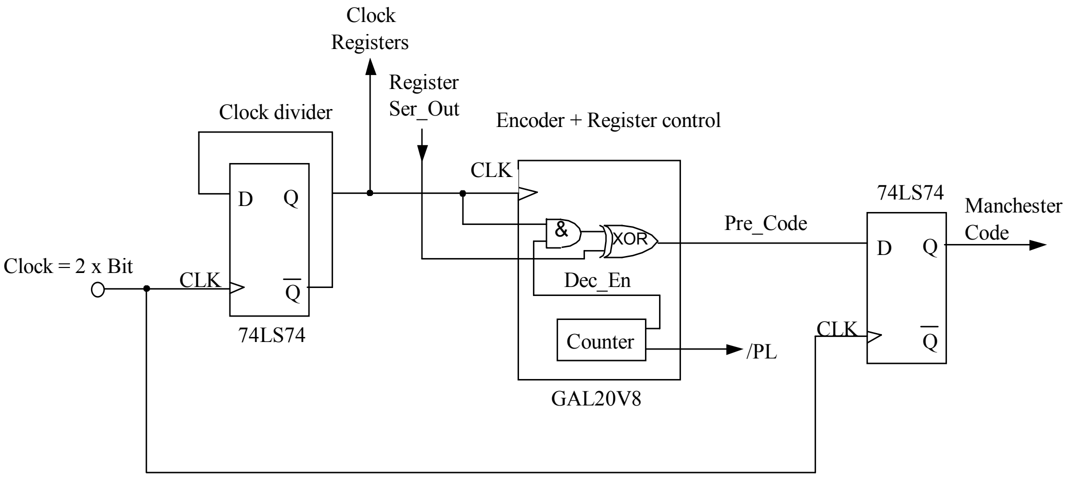

Fig. 5.22 Schematic of the encoder in the GAL20V8.

which has four bits, the total number of bits is $6 \cdot 8 + 4 = 52$ and the data rate would be

$$n = \frac{52 \text{ bit}}{40 \ \mu\text{s}} = 1.3 \text{ Mbit/s}.$$

In the future, this rate is likely to increase. One could imagine a checksum for an error detection or attach some bits to inform the system about the status of the front end. A framewidth of 68 bit is a reasonable estimate. It includes two status bits per channel and reserves eight bits for a checksum. This would lead to a data rate of

$$n = \frac{68 \text{ bit}}{40 \ \mu\text{s}} = 1.7 \text{ Mbit/s}.$$

The maximum cable length is 2 km but in the laboratory only 1.8 km were available. According to Eq. 5.57, the ratio in data rate between these two length is 0.86. Thus the prototype with a 1.8 km cable was designed for a data rate of 2 Mbit/s to ensure the functionality at the longer distance of 2 km.

5.4.2 Line driver / receiver

The line driver and receiver are preferable selected as a pair. The requirements for these components are

- High bandwidth
- Small harmonic distortion
- High slew rate
- High output current

A driver / receiver combination that fulfills these requirements is the EL2141 line driver and the EL2142 line receiver from Elantec. They are suited for high speed, differential data transmission over twisted pair cables. The basic circuitry for the line driver and receiver is shown in Fig. 5.23. The driver was set to a gain of two and equipped with 56 Ω output resistors to terminate the cable at the source. To avoid reflections the cable must be terminated with its characteristic impedance of 110 Ω at the receiver. The values of the feedback resistors are typical recommendations from the datasheets.

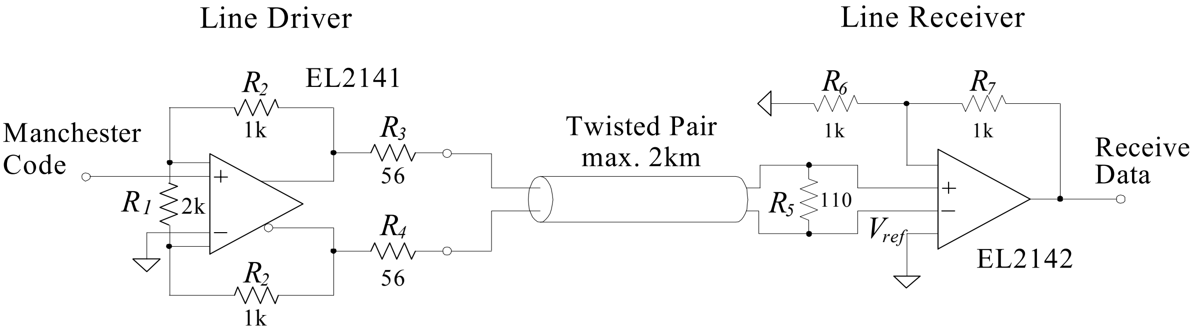

Fig. 5.23 Line driver and receiver circuit of the readout electronics.

After the receiver, the signal is highly distorted as presented in Fig. 5.18 b) and must be restored with a treshold comparator. The first prototype circuit uses the DS96173CN. It is a RS422 receiver but connected as a comparator. One problem that occurs is the treshold level. It should be set at 50% of the received, long-term signal amplitude to ensure an accurate signal restoration. However, this amplitude is determined by the DC attenuation of the cable, which varies with the length. Hence the treshold is also a function of the cable length. This is not preferable, thus the DC component of the signal is removed by coupling it via the highpass network C_2 and R_8. Consequently, the treshold is set to 0 V as shown in Fig. 5.24.

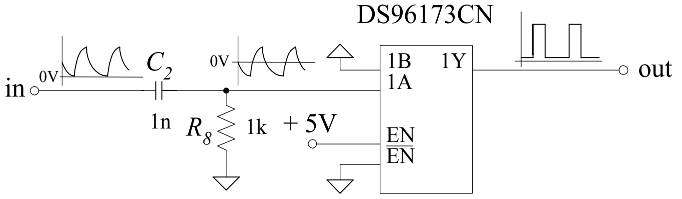

Fig. 5.24 Signal restoration with the DS96173CN.

5.4.3 Signal equalization

In section 5.4.1 a maximum data rate of 2 Mbit/s was calculated for a length of 1.8 km. The data is sent in Manchester Code, thus for the first calculation a pure square wave with a frequency of 2 MHz is used. It corresponds to a long period of consecutive zeros or ones. To calculate the signal distortion, the transfer function model of section 5.3.2 is taken. The signal $V_2(j\omega)$ at the end of a transmission line can be calculated with

$$V_2(j\omega) = V_1(j\omega) \cdot H(j\omega) \tag{5.58}$$

where $V_1(j\omega)$ is the input signal and $H(j\omega)$ corresponds to the transfer function of the cable. The magnitude of this transfer function was presented in Fig. 5.3, which showed a lowpass behavior. If the signal distortion should be reduced, the cut-off frequency must be increased, thus the cable attenuation has to be compensated. A line equalizer serves this purpose by a transfer function $G_1(j\omega)$ that is inverse to the cable transfer function $H(j\omega)$:

$$G_1(j\omega) = H^{-1}(j\omega). \tag{5.59}$$

The left part of Fig. 5.25 shows the receiver EL2142 with a frequency dependent feedback network, according to its data sheet. In the right part, the gain of the receiver versus frequency is drawn. At low frequencies, the gain is set by $(R_6 + R_7)/R_6$. As the frequency increases, the capacitor C_1 leads to a rise of 20 dB per decade until the gain saturates at $(R_7 + R_6 \| R_8)/R_6 \| R_8$. If the frequency is further increased, the gain is limited by the open loop gain of the receiver, which leads to a drop of 20 dB per decade. The cut-off frequencies are shown in the diagram. The calculation is presented in appendix B.5 and the complete circuit diagram is shown in Fig. A.6.

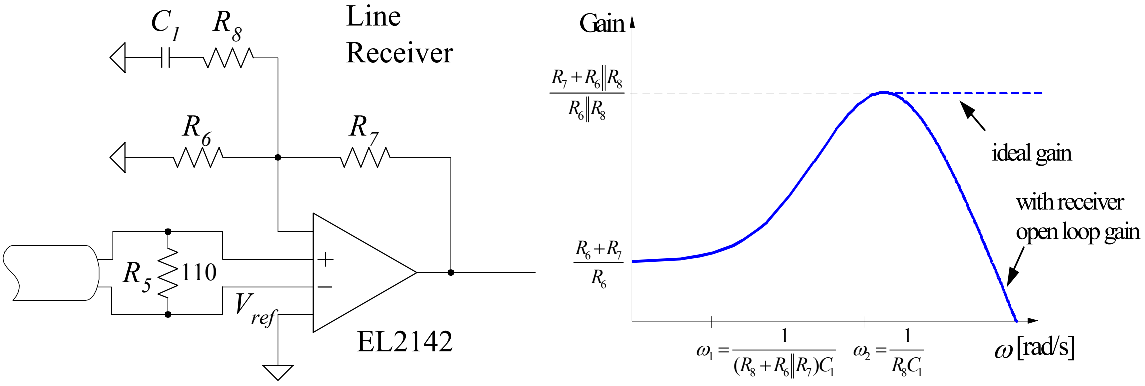

Fig. 5.25 Line receiver with gain compensating feedback network. Left: Circuit of the receiver. Right: Frequency dependent gain; the dotted line would be the ideal gain of the equalizing network. At high frequencies it is determined by the open loop gain of the receiver.

The optimization of the feedback network was performed with the approximated cable transfer function in Mathematica. For a 1.8 km long NG18 the transfer function was given in Eq. 5.51. It describes a lowpass with four real poles:

$$H(j\omega) = A_{DC}\frac{1}{(1+j\frac{\omega}{\omega_{p1}})(1+j\frac{\omega}{\omega_{p2}})(1+j\frac{\omega}{\omega_{p3}})(1+j\frac{\omega}{\omega_{p4}})}. \tag{5.60}$$

The lowest cut-off frequency in the above equation will be canceled by the first bend of the equalizer gain, which is

$$G_1(j\omega) = \frac{R_6+R_7}{R_6}\cdot\frac{1+s(R_8+R_6\,||R_7)\,C_1}{1+sR_8C_1} \tag{5.61}$$

as long as it is smaller than the open loop gain of the receiver (ideal gain, marked by the dotted line). First, the DC gain was set to two with $R_6 = R_7 = 1$ kΩ to have as much gain boost at high frequencies as possible. According to the solution in Eq. 5.53, the lowest cut-off frequency of the cable is $\omega_{p1} = 9.089\cdot 10^5$ rad/s. If R_8 is neglected, since it is assumed to be much smaller than $R_6\,||R_7$, the capacitor C_1 can be calculated with

$$\omega_{p1} \approx \frac{1}{R_6\,||R_7\,C_1} \rightarrow C_1 = \frac{1}{R_6\,||R_7\,\omega_{p1}} = \frac{1}{500\cdot 9.089\cdot 10^5} = 2.2 \text{ nF}. \tag{5.62}$$

The equalizer gain at high frequencies is determined by R_8. It introduces the second bend before the gain crosses the open loop function of the receiver, so no ringing will occur. Since R_8 also influences the exact value of the zero in Eq. 5.61, its value was derived graphically. The best results were obtained with $R_8 = 33\ \Omega$. Figure 5.26 a) compares the transfer function of the cable with and without equalizer as well as the equalizer gain itself. The picture in Fig. 5.26 b) shows the difference in the step response due to an ideal step.

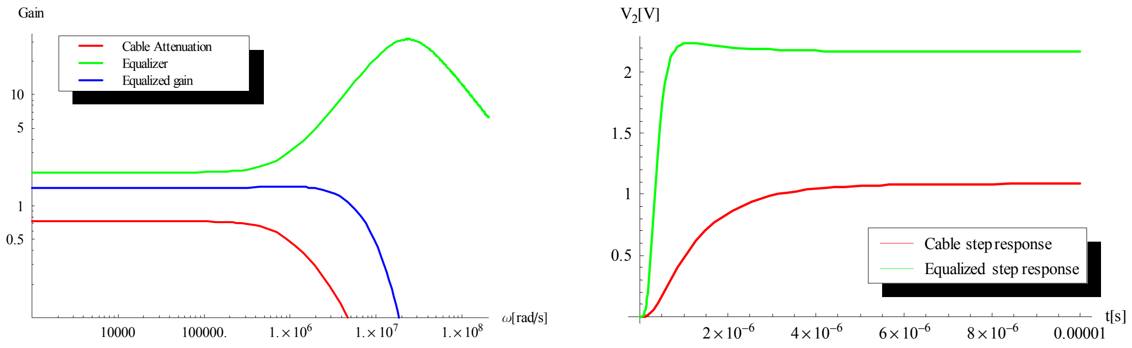

a) b)

Fig. 5.26 Improvement of the cut-off frequency of the NG18 cable by a line qualizer. a) The red curve shows the cable transfer function without and the blue curve with the equalizer. The green curve depicts the equalizer gain. b) Step response of the cable with and without equalizer.

With the line equalizer, the 3dB cut-off frequency is moved from $\omega_1 = 8.848 \cdot 10^5$ rad/s to approximately $\omega_2 = 5.066 \cdot 10^6$ rad/s, this is an improvement of a factor 5.73. Approximately the same improvement in the rise time is observed, which decreases from 2.47 μs to 0.41 μs (see appendix B.5).

Figure 5.27 a) compares the step response with and without the equalizer. In the first impression, the effect seems to be moderate regarding the long tail. However, this tail is due to the low-frequency behavior of the cable and doesn't really affect the maximum data rate. The initial rise, however, is much faster than the original step response. Fig. 5.27 b) shows a square wave of 2 MHz, which corresponds to the baseband of the Manchester encoded signal. The picture shows the improvement of the equalizer more clearly. At that frequency, the cable attenuation reduces the amplitude to approximately 16 mV$_{pp}$. Together with the small SNR ratio a reliable restoration is impossible. With the equalizer, the amplitude after 1.8 km is still 320 mV$_{pp}$ enabling a reliable signal restoration.

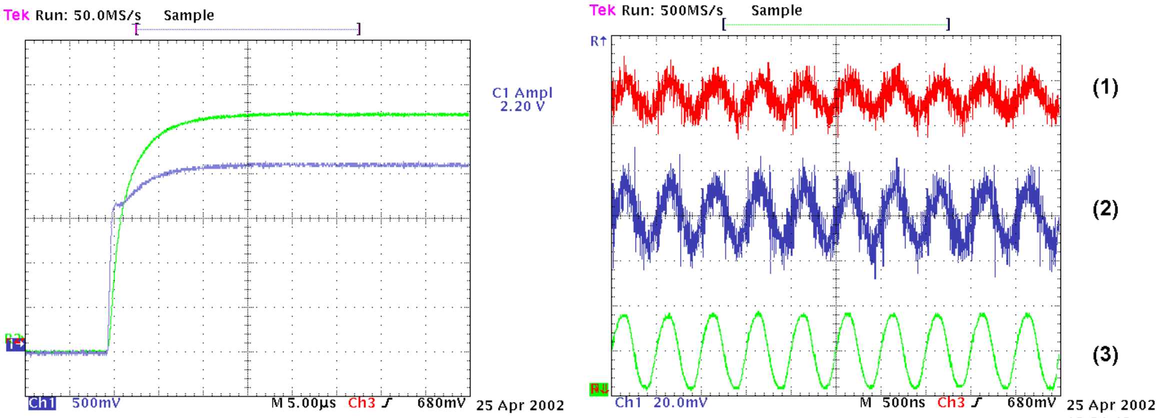

a) b)

Fig. 5.27 Improvement of the equalizer on the signal transmission: a) The step response without (green, 200 mV/div) and with the equalizer (blue, 500 mV/div). b) A 2 MHz square wave after 1.8 km. The top waveform (1) is the signal before the receiver. It is attenuated to 16 mV$_{pp}$. In the middle (2), the receiver operated at a gain of two, simply doubles the amplitude. The bottom waveform (3) shows the received square wave if the equalizing network is used. Here, the amplitude is 320 mV$_{pp}$.

The same signals are calculated with the transfer function model. The step response in Fig. 5.28 shows a deviation from the measured waveform, mainly due to the imperfections of the receiver and the fact that the line isn't terminated exactly.

Figure 5.29 a) compares a 2 MHz square wave after 1.8 km with the calculated transfer function model without the equalizer. The calculated amplitude is 22 mV and the transfer function model shows a good approximation. With the equalizer, the calculated amplitude is 512 mV as shown in Fig. 5.29 b). The model shows a larger deviation to the measured square wave. The reasons are uncertainties in the calculation, such as a nonideal receiver and errors in the calculated cable attenuation.

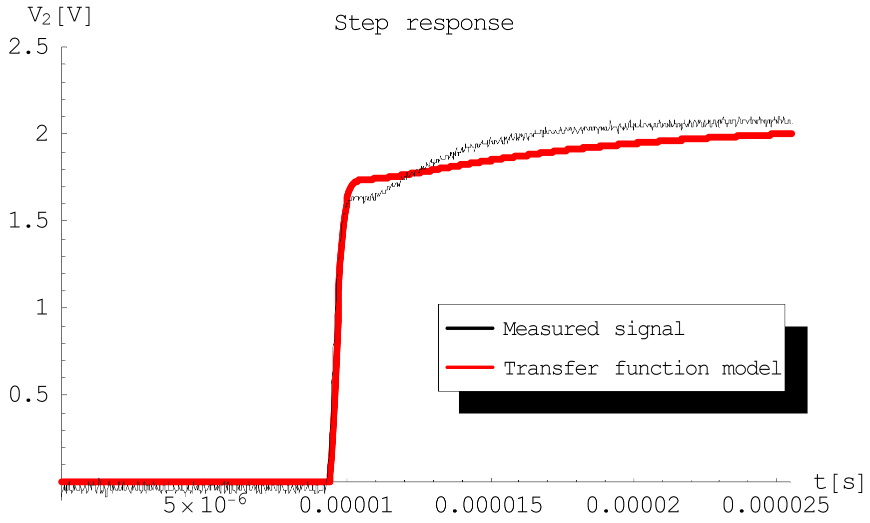

Fig. 5.28 Step response after 1.8 km with the equalizer. The measured signal is compared with the transfer function model.

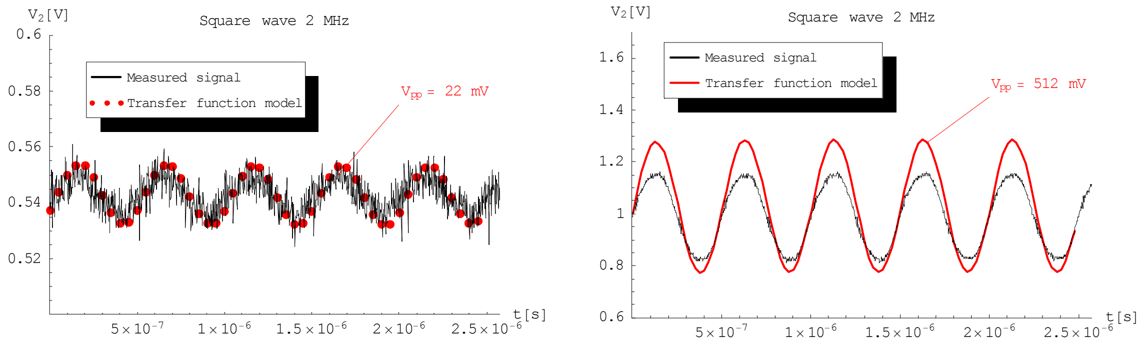

a) b)

Fig. 5.29 A 2 MHz square wave after 1.8 km. a): The large cable attenuation reduces the amplitude to 16 mV$_{pp}$ and the small SNR make a reliable restauration impossible. The simluated square wave with the transfer function model results in an amplitude of 22 mV. b): The same signal but with the line equalizer, the calculated amplitude is 512 mV$_{pp}$.

The next step is to examine a real Manchester encoded signal. Fig. 5.30 a) contains an arbitrary bit pattern together with the specified FAW (1100, not encoded). The code isn't a pure square wave but can be seen as a phase modulated signal. If a bit changes, the encoded logic state is twice as long as before, either zero or one. Thus the signal needs a certain time to settle around the average value, which is illustrated in Fig. 5.30. The dashed line illustrates the comparator treshold for the signal restoration. Obviously, the presented signal introduces a large jitter.

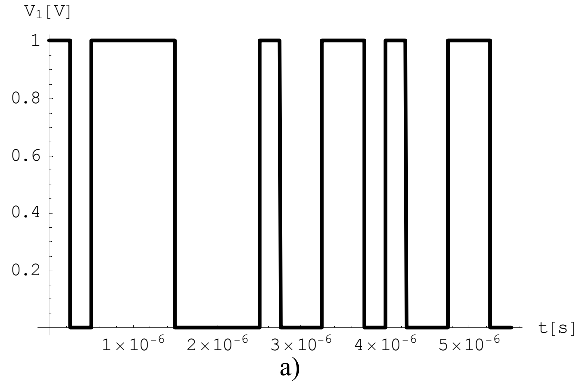

Fig. 5.30 Distortion of a Manchester encoded signal after 1.8 km with the equalizer. a) Input signal with the FAW. b) The output signal needs a certain time to settle around the average value (dashed line).

Therefore, a second equalizer was added as shown in Fig 5.31 a). It is placed after the receiver and uses only passive components. In contrast to the former circuit, this network attenuates the low frequencies instead of amplifying the higher ones. Again Mathematica was used to add a second transfer function $G_2(j\omega)$:

$$G_2(j\omega) = \frac{R_{10}}{R_9 + R_{10}} \cdot \frac{1 + sR_9C_3}{1 + s(R_9\,||R_{10})C_3}. \tag{5.63}$$

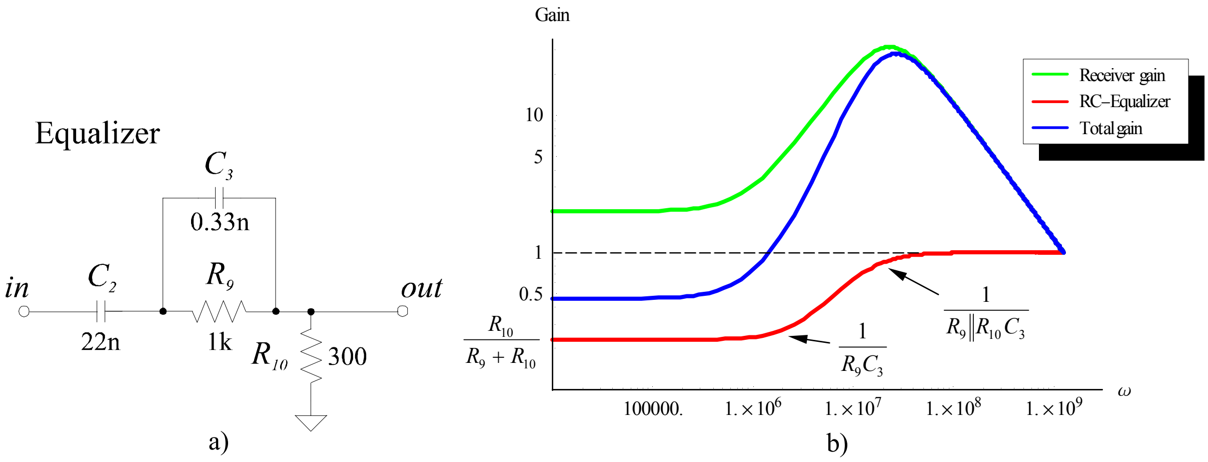

Fig. 5.31 The passive equalizer attenuates the low frequencies: a) Schematic of the circuit, with C_2 for AC-coupling. b) Transfer function of the cable after the second equalizer stage.

The component selection must consider two facts. First, the DC attenuation should not be too large and second, any change in the frequency characteristic above the bandwidth of the receiver doesn't improve the rise time because the gain falls down steeply. Thus the higher bend in the transfer function is placed around the maximum gain of the receiver as illustrated in Fig. 5.31 b). The DC attenuation was set to approximately 25%, using $R_9 = 1\ \text{k}\Omega$ and $R_{10} = 300\ \Omega$. The peak in the receiver gain is at $1.5 \cdot 10^7$ rad/s. With Eq. 5.63, the capacitor C_3 can be obtained as

$$C_3 \approx \frac{1}{1.5 \cdot 10^7 \cdot 300\,||1000} = 0.29\text{ nF}$$

the standard value $C_3 = 0.33$ nF was selected. The capacitor C_2 removes the DC value and makes the treshold independent of the cable length. This second equalizer further increases the bandwidth by a factor of 2.25. Figure 5.32 a) shows the transfer function of the cable compared with the transfer function using only the first and using both equalizers. The blue curve is the already known attenuation after the first equalizer. The green curve depicts the attenuation after the second equalizer. It shows a peak, which leads to ringing in the step response. Figure 5.32 b) compares the signal distortion after the first and the second equalizer. The same Manchester Code as in Fig. 5.30 b) is used. Although the average value is attenuated by four, the signal settles around the treshold very fast, which results in a more reliable restoration and less jitter.

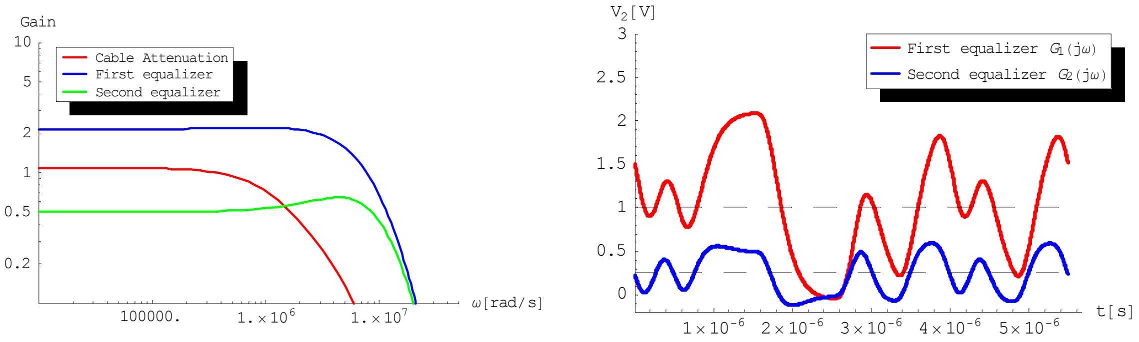

a) b)

Fig. 5.32 Further improvement of the signal bandwidth with the second equalizer $G_2(j\omega)$. a) The cable attenuation (red) is compared with the two equalized transfer functions. The blue curve is the already presented attenuation after the first equalizer and the green one after the second equalizer. b) The same Manchester encoded signal as in Fig. 5.30 is compared with the signal using both equalizers.

The final test of the equalizers is presented in Fig. 5.33. It shows the beam loss signal, which is transmitted over 1.8 km with 2 Mbit/s. Again, the benefit of the second equalizer can be clearly observed. The restored signal after 1.8 km is shown in the bottom waveform. It is Manchester encoded but the FAW can be easily recognized, since it is not encoded.

The presented equalization enables a high data rate for the signal transmission from the tunnel to the surface. However, the cable lengths are different at each front end in the tunnel. The frequency dependent gain of the equalizer was designed in a way that the frequency characteristic is flat up to the cut-off frequency and doesn't show a large resonance peak. At shorter cables, the gain of the equalizer will lead to ringing because the cable attenuation is less. The signals at different cable lengths are shown in Fig. 5.34. The top waveform depicts the signal

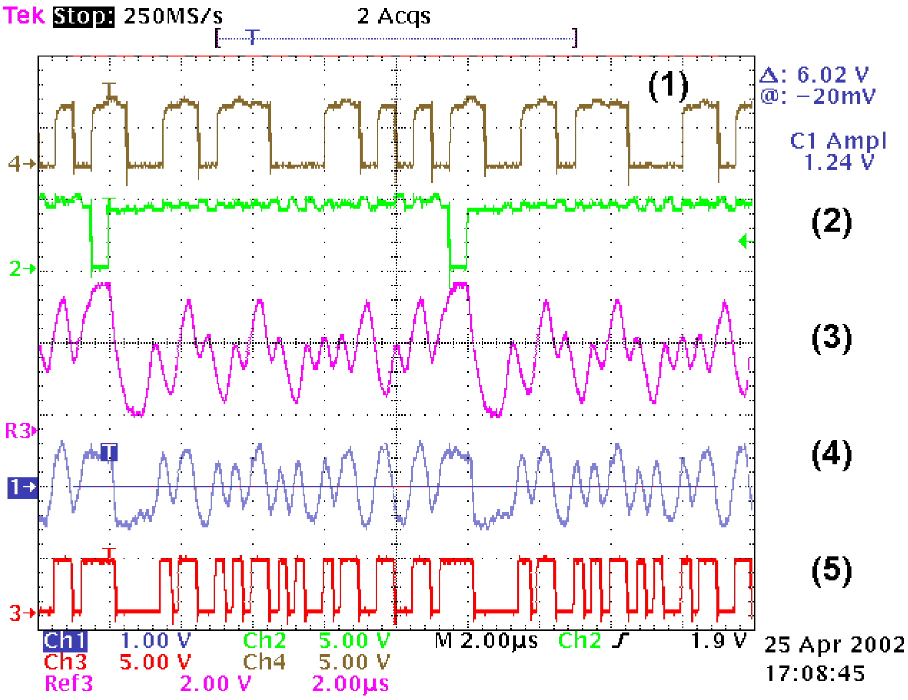

Fig. 5.33 Data transmission of the front end signal over 1.8 km at 2 Mbit/s. The serial data of the front end (1) is loaded into the shift registers; parallel load signal in (2). After the first equalizer (3) the signal amplitude is quite large but the signal needs a certain time to settle around the average value, which could result in missed pulses and leads to a high jitter. The second equalizer solves this problem. The amplitude has decreased (4) but the edges are steep and enable a clear signal restoration as illustrated in (5).

after 1.8 km. Below, the cable length is 1.4 km. Overshoots occur but don't lead to restrictions. The last two signals correspond to a line length of 1 km. At this length, the equalizer shows a large resonance peak and the overshoots affect the signal restoration. Fortunately, the attenuation is already small enough that the equalizers are not needed anymore, which is illustrated by the bottom waveform. At the final layout, the different cable length must be taken into account by disabling the equalizer(s), e.g. with jumpers. This constitutes the major disadvantage of the presented data transmission with fixed line equalizers.

5.4.4 Synchronization

Before the data can be evaluated, it must be synchronized to the local clock. Fortunately, Manchester Code makes the task easy since it contains the clock information in the data itself. A counter algorithm that is often used in point-to-point connections ensures an easy signal synchronization. The main principle is shown in Fig. 5.35 and the PSpice simulation is illustrated in Fig. A.4. In order to decode the data, it must be sampled at least twice a bit because the Manchester Code consists of two different logic states per bit. A receiving clock, which runs eight times faster than the data rate is used, i.e. for a data stream of 2 Mbit/s, the receiver

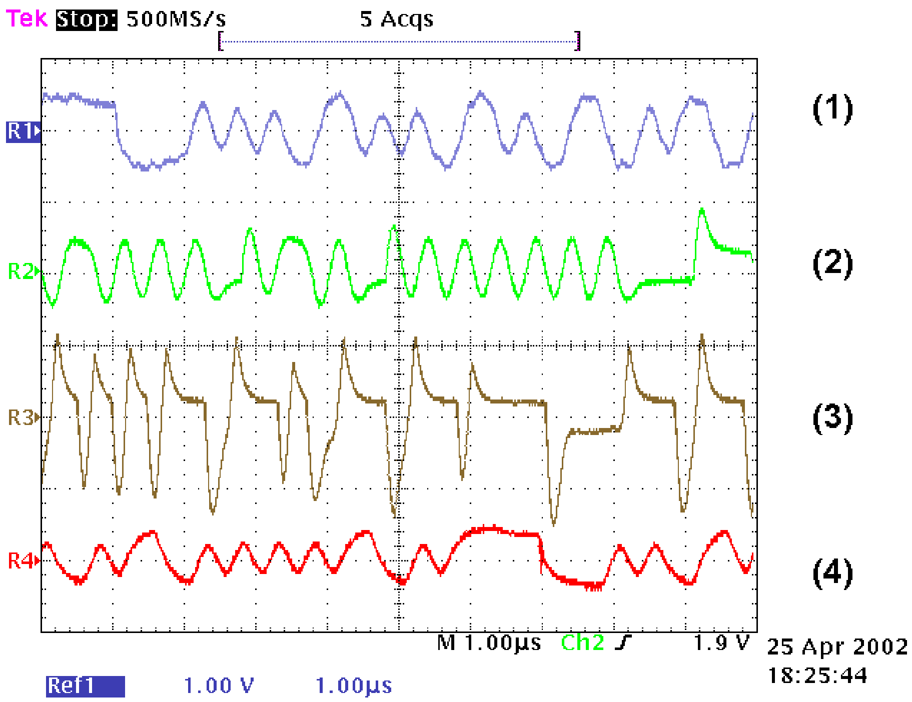

Fig. 5.34 Distorted signal after 1.8 km (1), 1.4 km (2) and 1 km (3) with both equalizers. The bottom waveform (4) shows the signal after 1 km without equalizer.

clock must have a frequency of 16 MHz. Whenever a logic transition occurs, the counter is reset (marked with R). Then it counts until two and the actual signal amplitude is sampled. After that, it is reset again and counts until four, where the next data is sampled. Hence the logic state of the encoded signal is sampled in the first and in the third quarter of the bit period. If no rising edge occurs, the counter will always count until four and the corresponding data values are sampled. At the next rising edge of the data it is reset again, and so on. In the worst case, the phase shift between the data and the receiving clock is one eighth of the receiver clock frequency. Hence the sample points can vary only one eighth of the bit period, i.e. 12.5 ns. Even in this case, the data will be evaluated correctly.

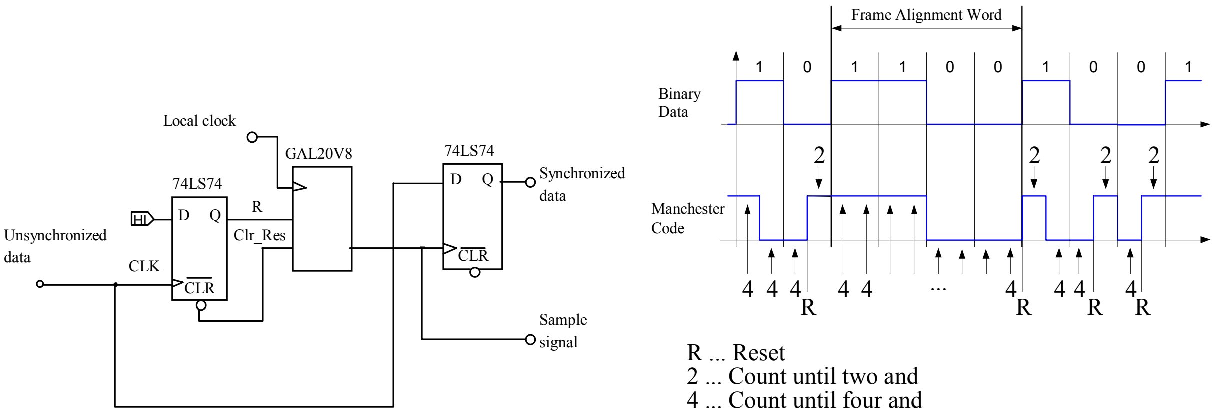

Fig. 5.35 Synchronizer: Left: Circuit diagram. Right: Principle of operation.

As shown in the left part of Fig. 5.35 a), the counter was programmed in a GAL20V8. Figure 5.36 illustrates the state diagram and the corresponding logic table of the counter. To program the GAL, the boolean expressions for the counter variables $z_{2..0}$ and the output variables Clr_Res and y must be found. This can be done with a Karnaugh diagram. The results are presented in appendix C.2. The boolean expressions are written in a text file and compiled into a JEDEC file, which is programmed into the GAL. One must distinguish the different options for the output variables. If the parameter ".r" is set, the value is stored in a flip-flop and set one clock cycle later. If the parameter ".o" is used, the corresponding output value is set immediately at the next clock cycle.

R = 1 leads to state 0/0 from any other state
Clr_Res = R, one clock cycle delayed

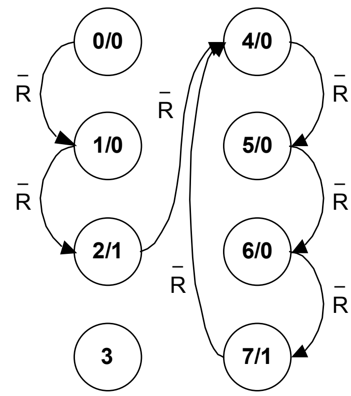

R	z_2	z_1	z_0	z'_2	z'_1	z'_0	Clr_Res.r	y.o
	0	0	0	0	0	1		0
	0	0	1	0	1	0		0
|	0	1	0	1	0	0	|	1
0	0	1	1	x	x	x	0	x
|	1	0	0	1	0	1	|	0
	1	0	1	1	1	0		0
	1	1	0	1	1	1		0
	1	1	1	1	0	0		1
1	x	x	x	0	0	0	1	0

Fig. 5.36 Realization of the synchronizer with a counter algorithm. Left: State diagram of the algorithm. Right: Corresponding logic table.

One fact must be emphasized: The received Manchester data can't be decoded to common binary data data immediately. This is because of the uncertainty of the code itself. A received 010101 can be interpreted as a consecutive series of zeros or ones because the phase uncertainty is 180°. In order to determine the border between the bits, a change in the logic state is needed at least once. However, the FAW can be used to determine the border because it is not encoded. Thus the data can only be evaluated after the first occurrence of the FAW or a logic transition – but this poses no problems.

At this point, a synchronized, Manchester encoded, serial data stream is available at the receiver side. The dump controller, a microcontroller or a DSP, will decode the data into the binary form code and the calculate the beam loss over different time intervals. If the losses exceed a certain treshold a beam dump will be triggered. The tresholds must be suited to the time interval and the actual beam energy. An interface to the beam interlock system must be programmed. The data evaluation constitutes one of the future tasks of the beam loss system but until now, no investigations have been made in that direction.

6 Summary

The thesis described the development and partly the realization of the readout electronics for the beam loss monitors of the LHC. The expected particle losses increase the temperature of the superconducting magnets of the accelerator. If the temperature exceeds a certain treshold, the magnet will quench, i.e. it will be driven into the normal conducting state. This leads to an undesired down-time of the LHC of some hours up to several weeks, if a magnet is damaged during such a quench. Therefore, the particle losses are measured and the beam has to be extracted safely (= dumped) before a quench occurs.

After a general introduction in the LHC and the expected particle losses, the structure of the readout chain was presented. Ionization chambers are installed to transform the particle loss rate into an electric current. This current covers a wide dynamic range of nearly 140 dB. Several possibilities to measure the current of the chamber were discussed. The current-to-frequency converter is a smart solution that is able to cover the wide dynamic range with low effort. It produces an output frequency proportional to the input current and simplifies the data transmission from the tunnel to the surface, where the beam loss signal is evaluated. Tests revealed an excellent linearity of the CFC. However, the big difference in the quench levels at 450 GeV and 7 TeV leads to a high operation frequency of the front end of 5 MHz, which makes the data transmission complicated. This problem was solved by reducing the actual acquisition rate to 25 kHz. Moreover, six channels are multiplexed and transmitted via a twisted pair cable. The distance between the front end location and the surface building, where the final data evaluation is performed, can be up to 2 km. This distance is too long for the calculated data rate of 1.7 Mbit/s. Therefore, the signal is transmitted in Manchester Code and line equalizers are used to increase the cable bandwidth, which ensures a reliable signal restoration and less jitter. The discussions about the data transmission over a cable lead to a detailed investigation in the frequency and time domain behavior of transmission lines. The results of these simulations agreed with the observed signals in the laboratory. Finally, the complete readout chain was presented and successfully operated in the laboratory.

The future will lead to excessive tests in terms of reliability and improvement of the different components. A calibration cycle is proposed to handle the offset error of the front end and to ensure its functionality. Status bits are foreseen, which indicate the actual state of the front end. These bits are already included in the data rate calculation of the signal transmission. The multiplexed transmission itself might pose a problem. The six channels, which form the data stream, contain all beam loss monitors of a whole magnet. If the transmission fails, a complete magnet is lost and can't be observed anymore. Thus improvements are foreseen, such as a second transmission system for redundancy. The final decision, whether the beam must be dumped or not, is done by the dump controller. It has to demultiplex the received data stream and to calculate the losses over different time intervals. A dump table will be provided, which includes the tresholds for the beam dump, dependent on the duration of loss and the beam energy. To trigger a dump, the controller must interface the beam interlock system, which finally triggers the kicker magnets to extract the beam.

The beam loss monitors of the LHC constitute a vital part of the machine. It has to be a reliable security installation, which is necessary to run the accelerator safely. Until now, only a first study with realizations in the laboratory are performed. The present work constitutes the basement for the beam loss system. Now it has to be improved, tested and made ready to go into production, to guarantee the successful operation of the world's largest particle accelerator – the LHC.

Acknowledgments

The very last chapter that has to be written are the acknowledgments and a friend told me that it is the most important one (because it is the most read section of a thesis). Anyway, it is the part I enjoyed most, since it allows me to look back on the work I did and the people who were related with that work.

The person, who was involved most in my subjects, was my supervisor Bernd. He always had time to listen to my complaints, questions, breakthroughs and never got tired explaining me all the details about the beam loss monitors and accelerator physics in general. The most important thing was that he always supported my work and motivated me. We also had a lot of fun because of our very cooperative relationship. Of course, I also want to thank my supervisor at the Fachhochschule Wiener Neustadt, Helmut Frais-Kölbl. His experience in electronics helped me a lot to make progress if I found myself in a dead end.

Beside my two supervisors, I always could get hints and advice from Gianfranco and especially Jan. Even he wasn't directly involved in the beam loss monitors – I made him to be. I don't think that the project would be at the present state without his help. Moreover, I enjoyed their punctuality in terms of coffee breaks, sometimes the most bright time at the day. I don't want to forget Edda. We had a nice time working together, maybe because of our both passion for chocolate or because we just had the same sense of humor. I will really miss our smalltalk during the day. Of course, I also want to mention the rest of the BI/PB section, who created a very familiar atmosphere. They supported me if I had questions or helped me with translations if my French was a big mess. Especially I want to thank Claudine for producing all my nice prototype circuits.

CERN isn't only a place to work but also to have fun. I remember nice parties, lunch breaks and skiing trips. Here I want to mention the big Austrian group and my Italian-Spanish friends. It would be a long list of names – but I'm sure the people know who is addressed.

I owe a lot to my family at home who supported me as good as they could. My parents, Franz and Regina, who always were there for me and encouraged me during my studies. Finally, I have to thank Andrea. It was a hard time being apart but I think we managed it very well. Thank you for being there.

List of Abbreviations

AC	alternating current
ADC	analog-to-digital converter
BLM	beam loss monitor
CERN	Conseil Européen pour la Recherche Nucléaire
CFC	current-to-frequency converter
DC	direct current
FAW	frame alignment word
GAL	gate array logic
(J)FET	(junction) field effect transistor
LHC	Large Hadron Collider
MIP	minimum ionizing particle
op amp	operational amplifier
SNR	signal-to-noise ratio
SPS	Super Proton Synchrotron
TEM	transverse electromagnetic mode
VME	Versa Module Europa

List of Figures

Fig. 2.1 Schematic view of the two beams of the LHC. 4

Fig. 2.2 Cross-section of an LHC dipolemagnet. 5

Fig. 2.3 Overview of CERN's accelerator complex. 6

Fig. 2.4 Different quench levels for 450 GeV and 7 TeV [Gsch-01]. 9

Fig. 3.1 BLM location at the quadrupoles. 10

Fig. 3.2 Picture of an SPS-type ionization chamber (left) and schematic structure inside the cylinder (right). 11

Fig. 3.3 Electrical connection of the ionization chamber. 12

Fig. 3.4 Quench level equivalent chamber current at 450 GeV and 7 TeV as a function of the loss duration. 14

Fig. 3.5 Circuit for the transient response measurement of the ionization chamber. 14

Fig. 3.6 Measurements of the ionization chamber current versus time. 15

Fig. 3.7 Schematic of the beam loss monitor readout chain. 16

Fig. 4.1 Overview of the different techniques to measure electric current. 19

Fig. 4.2 Direct Monitoring Techniques: a) Cascaded amplifier. b) Switched gain transimpedance amplifier. 20

Fig. 4.3 Principle of a switched integrator: a) Only with a reset switch, b) Improved circuit with additional hold switch. 22

Fig. 4.4 Principle of the charge balanced current-to-frequency converter. 23

Fig. 4.5 CFC characteristic and nominal maximum chamber current compared with the dump levels. The maximum current is illustrated by the horizontal green line. It corresponds to a duty cycle of 50%. The blue curve shows the one integration time of the CFC. It must stay below the dump levels. 25

Fig. 4.6 Pre-integrator: a) Circuit. b) Typical waveform. 27

Fig. 4.7 Analog integrator of the CFC. 28

Fig. 4.8 Treshold comparator. 29

Fig. 4.9 One-shot circuit. 30

Fig. 4.10 Typical output pulse width at capacitor values below 10 nF for different timing resistors (Philips Datasheet 74HCT123). 31

Fig. 4.11 PSpice simulation of an overload situation. 32

Fig. 4.12 Reference current source. 33

Fig. 4.13 Current switch. 34

Fig. 4.14 Evaluation of the CFC output frequency with a counter-register pair. 35

Fig. 4.15 Leakage currents of the CFC. 37

Fig. 4.16 Output voltage of the analog integrator due to the total leakage current. 38

Fig. 4.17 The error due to the external components is estimated by linearizing the pulse width characteristic, which equals $y = x^{0.4}$. 40

Fig. 4.18 Nonideal integration: a) Step response at short time intervals. b) Deviation from the ideal step response after long time intervals. 42

Fig. 4.19 Charge injection of the current switch. 43

Fig. 4.20 Analog output voltage of the integrator and the one-shot for a maximum current of 200 μA. 45

Fig. 4.21 Analog output of the CFC with a square wave input current from 30 nA to 100 nA. 45

Fig. 4.22 Analog output voltage of the integrator and the one-shot for a maximum current of 1 mA. 46

Fig. 4.23 CFC output frequency and linearity error versus input current. 47

Fig. 4.24 Measurement of the remanent beam dump radiation with 200 m of cable between the chamber and the front end. 48

Fig. 5.1 Measurement of the line parameters R’, L’ and C’. 50

Fig. 5.2 Measurement of the cable attenuation. 51

Fig. 5.3 Attenuation of different types of cables versus frequency. 52

Fig. 5.4 Equivalent circuit for an infinitesimal short symmetric transmission line. 54

Fig. 5.5 Skin resistance versus frequency. 58

Fig. 5.6 Attenuation of the NG18 due to skin effect and dielectric loss compared with the total attenuation. 61

Fig. 5.7 Actual input step of the NG18. 63

Fig. 5.8 Impulse and step response according to the model in Eq. 5.30 after 1.8 km. 64

Fig. 5.9 Impulse and step response only due to the skin effect after 1.8 km. 65

Fig. 5.10 Step response after 1.8 km taking the dielectric loss into account, according to [Cur-85]. 67

Fig. 5.11 Attenuation with modified dielectric loss. The conventional dielectric loss assumes $V_D \propto e^{-k|\omega|}$, while the modified dielectric loss uses $V_D \propto e^{-k(j\omega)^m}$. 69

Fig. 5.12 Causal time domain model of a transmission line with modified dielectric loss after 1.8 km. 69

Fig. 5.13 Nonlinear lest square fit of the cable attenuation after 1.8 km with a rational transfer function. 71

Fig. 5.14 Impulse and step response due to the transfer function approximation after 1.8 km. 71

Fig. 5.15 Influence of the cable length on the signal amplitude and rise time. 72

Fig. 5.16 Block schematic of a typical digital data transmission system. 74

Fig. 5.17 Signal distortion at different duty cycles. 75

Fig. 5.18 Manchester Code offers a high duty cycle. 76

Fig. 5.19 Readout schematic of the CFC. 76

Fig. 5.20 Manchester encoder avoids spikes in the signal. 77

Fig. 5.21 The FAW – 1100 – is not encoded thus it can’t occur in the data and doesn’t change the DC average value. 78

Fig. 5.22 Schematic of the encoder in the GAL20V8. 79

Fig. 5.23 Line driver and receiver circuit of the readout electronics. 80

Fig. 5.24 Signal restoration with the DS96173CN. 80

Fig. 5.25 Line receiver with gain compensating feedback network. 81

Fig. 5.26 Improvement of the cut-off frequency of the NG18 cable by a line qualizer. 82

Fig. 5.27 Improvement of the equalizer on the signal transmission. 83

Fig. 5.28 Step response after 1.8 km with the equalizer. The measured signal is compared with the transfer function model. 84

Fig. 5.29 A 2 MHz square wave after 1.8 km. 84

Fig. 5.30 Distortion of a Manchester encoded signal after 1.8 km with the equalizer. 85

Fig. 5.31 The passive equalizer attenuates the low frequencies. 85

Fig. 5.32 Further improvement of the signal bandwidth with the second equalizer $G_2(j\omega)$. 86

Fig. 5.33 Data transmission of the front end signal over 1.8 km at 2 Mbit/s. 87

Fig. 5.34 Distorted signal after 1.8 km (1), 1.4 km (2) and 1 km (3) with both equalizers. The bottom waveform (4) shows the signal after 1 km without equalizer. 88

Fig. 5.35 Synchronizer: Left: Circuit diagram. Right: Principle of operation. 89

Fig. 5.36 Realization of the synchronizer with a counter algorithm. 89

Fig. A.1 Schematic of the current-to-frequency converter. 100

Fig. A.2 Schematic for the PSpice simulation of the CFC. 101

Fig. A.3 Manchester encoder layout. 102

Fig. A.4 Data synchronizer. 103

Fig. A.5 Schematic of the driver board. 104

Fig. A.6 Schematic of the receiver board. 105

List of Tables

Table 2.1 LHC parameters. 5

Table 3.1 Simulated shower particles per lost proton and cm^2 11

Table 4.1 Front end specifiactions. 17

Table 4.2 Main specifications of the CFC. 26

Table 4.3 Specifiactions of the OPA627. 27

Table 5.1 Parameters of the CERN multiwire cable NG18. 50

Table 5.2 Attenuation of the NG18 at different cable lengths. 52

Table C.1 Logic table to load the counter values into the registers and to encode the data. 122

References

[Bos-97] J. Bosser and G. Ferioli, ”Measurements of the Relative Sensitivities between some Beam Loss Monitors: Part I”, CERN, SL/BI 97-01, PS/BD 97-08, Feb. 1997

[Bos-98] J. Bosser and G. Ferioli, ”Measurements of the Relative Sensitivities between some Beam Loss Monitors: Part II”, CERN, SL/BI 98-, PS/BD 98-, Feb. 1998

[Bra-86] R. N. Bracewell, The Fourier Transform and its Applications, McGraw Hill, USA, 2^{nd} ed., 1986

[Cur-85] H. Curtins and A. V. Shah, ”Pulse Behavior of Transmission Lines with Dielectric Losses”, *IEEE Trans. Circuits and Systems*, Vol. CAS-32, pp. 819-825, Aug. 1985

[Gar-87] F. E. Gardiol, *Lossy Transmission Lines*, Artec House Inc., USA, 1987

[Gru-81] A. J. Gruodis and C. S. Chang, ”Coupled Lossy Transmission Line Characterization and Simulation”, *IBM Journal Research and Development*, Vol. 25, Jan. 1981

[Gru-93] C. Grupen, *Teilchendetektoren*, Wissenschaftsverlag, Germany, 1993

[Gsch-01] E. Gschwendtner et al., ”LHC Beam Loss Monitors”, CERN, SL/BI 2001-27, 2001

[Har-00] R. Harlander, *Das Standardmodell der Elementarteilchenphysik*, http://quark.phy.bnl.gov/~rharlan/files/teilchen/, 15.12.2002

[Jea-01] B. Jeanneret, ”Measurement of the Beam Losses in the LHC Rings”, LHC Project Note

[Joh-89] H. W. Johnson and M. Graham, *High Speed Digital Design - A Handbook of Black Magic*, Prentice Hall, USA, 1993

[Jon-77] A. K. Jonscher, ”The universal dielectric response”, *Nature*, Vol. 267, pp. 673-679, June 1977

[LHC-95] The LHC Study Group, ”The Large Hadron Collider - Conceptual Design”, CERN, AC/95-05(LHC), Oct. 1995

[Nah-62] N. S. Nahman, ”A discussion on the transient analysis of coaxial cables considering high-frequency losses”, *IRE Trans. Circuit Theory*, pp. 144-152, June 1962

[Ngu-94] T. Nguyen, ”Efficient Simulation of Lossy and Dispersive Transmission Lines”, *Proceedings of the 31st Design Automation Conference DAC*, San Diego, USA, 1994, http://www.sigda.org/Archives/ProceedingArchives/Dac/Dac94/papers/1994/dac94/pdffiles/39_1.pdf

[Ree-96] H. Reeg and O. Keller, ”Linearer Strom-Frequenz-Konverter”, Patent No. DE 195 20 315, Deutsches Patentamt, 1996

[Ree-99] H. Reeg, ”A Current Digitizer for Ionization Chambers / SEMS with high resolution and fast response”, *Proceedings of the 4th Workshop on Diagnostics and Instrumentation in Particle Accelerators DIPAC*, Daresbury, UK, pp. 140-142, 1999

[Rie-70] H. Riege, ”High-Frequency and Pulse Response of Coaxial Transmission Cables with Conductor, Dielectric and Semiconductor Losses”, CERN, PS/70-4, Feb. 1970

[Sch-01] R. Schmidt et al., ”Machine Protection for the LHC: Architecture of the Beam and Powering Interlock Systems”, CERN, LHC Project Note

[Sha-70] E. G. Shapiro, ”Linear Seven Decade Current-to-Frequency Converter”, *IEEE Trans. Nuclear Science*, Vol. 17, pp. 335-344, 1970

[Sie-01] A. Siemko, ”Magnet Quench Process”, *Proceedings of the LHC Workshop Chamonix XI*, Chamonix, France, pp. 245-249, 2001

[Sim-89] K. Simonyi, *Theoretische Elektrotechnik*, VEB Deutscher Verlag der Wissenschaften, 1989

[Vei-88] T. Veijola and M. Valtonen, ”Dispersive Transmission Line Model for nonlinear time domain circuit analysis”, *IEEE International Symposium on Circuits and Systems*, Espoo, Finland, pp. 2839-2841, 1988

[Vir-91] J. Virtanen, *Modeling of lossy transmission lines in the time domain,* Master’s Thesis (in Finnish), Helsinki Technical University, 1991, http://www.aplac.hut.fi/publications/dt-jarmo/main.html

[Wup-96] H. Wupper and U. Niemeyer, *Elektronische Schaltungen 2*, Springer Verlag, 1996

A Schematics

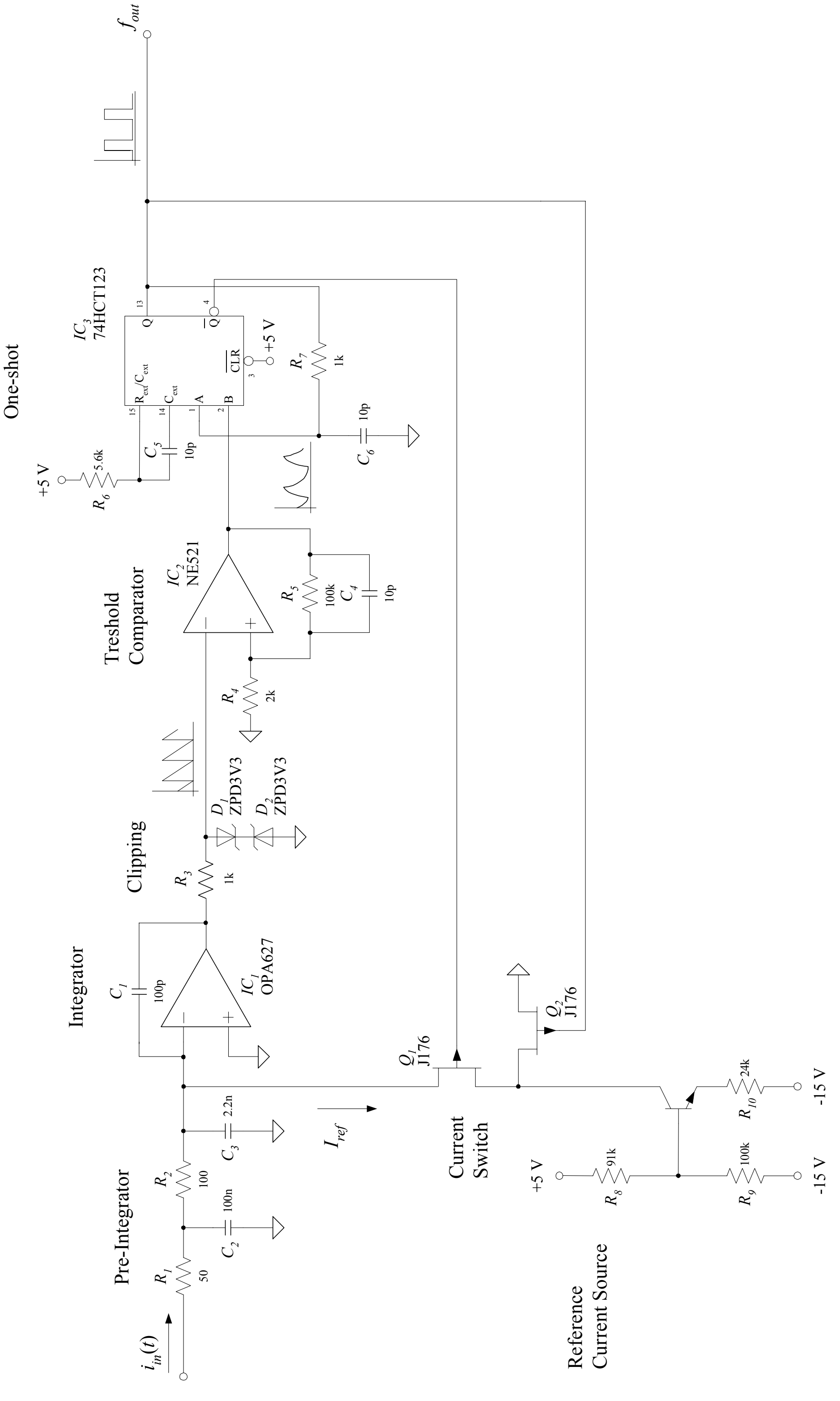

Fig. A.1 Schematic of the current-to-frequency converter.

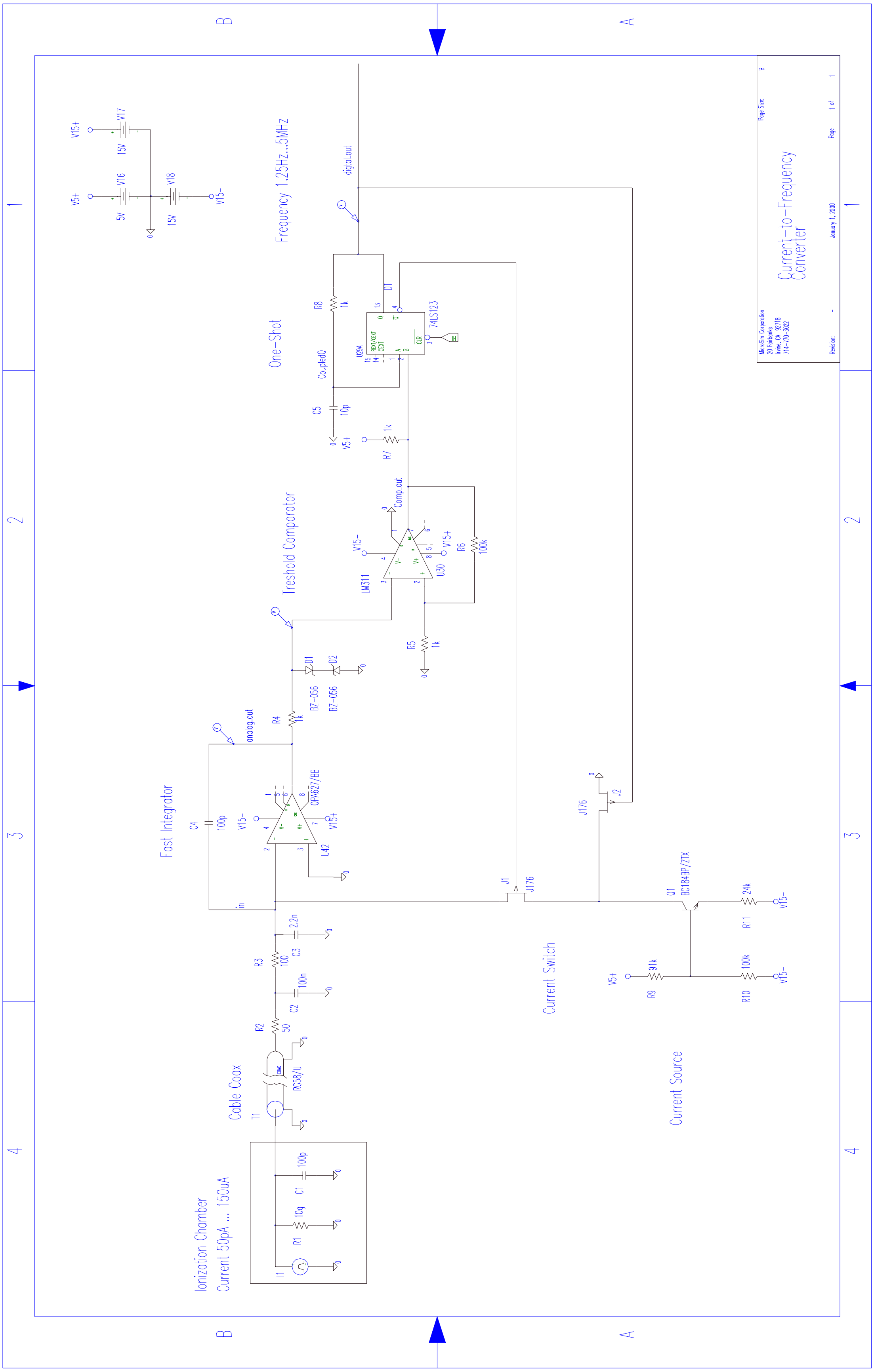

Fig. A.2 Schematic for the PSpice simulation of the CFC.

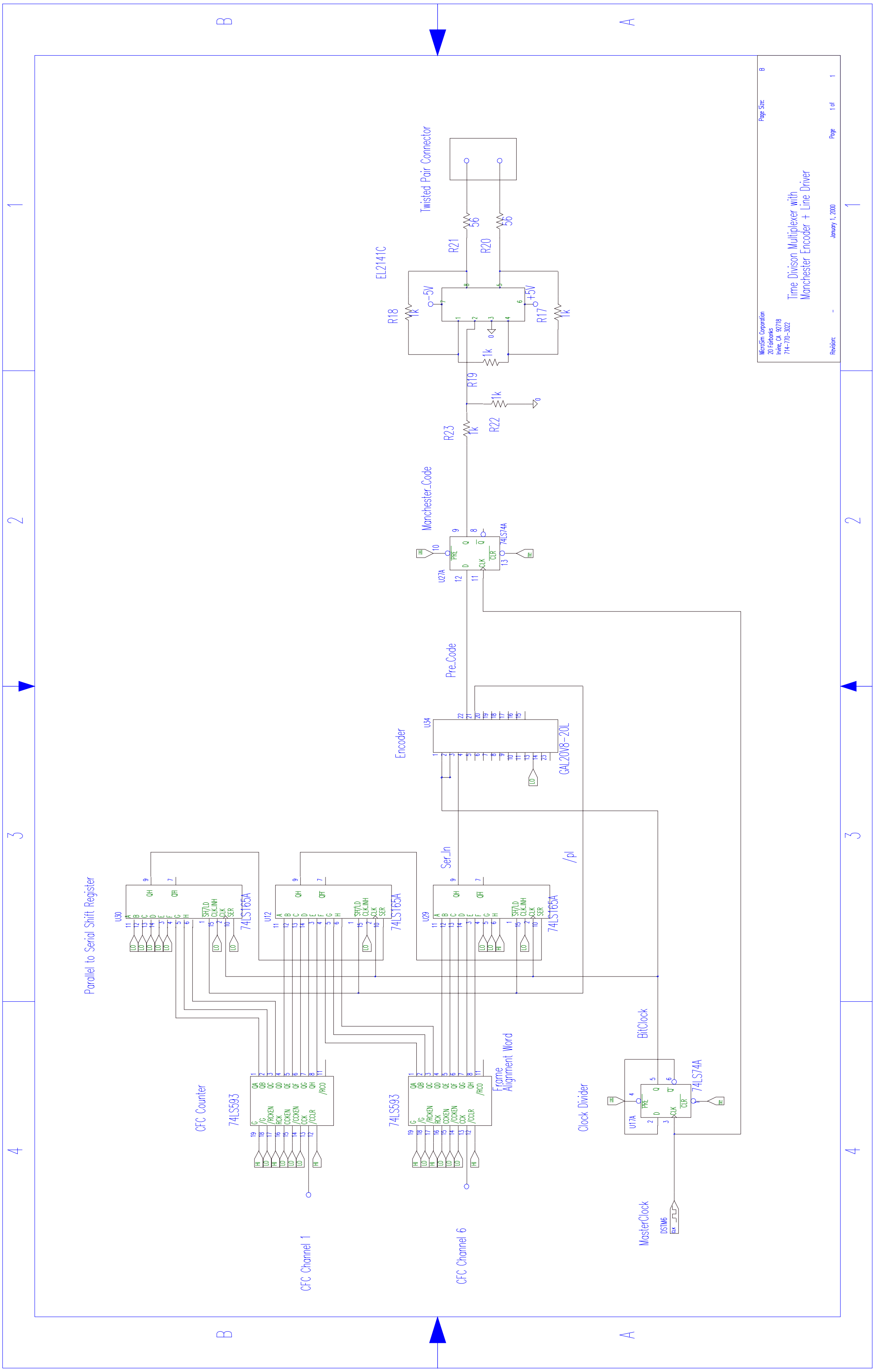

Fig. A.3 Manchester encoder layout.

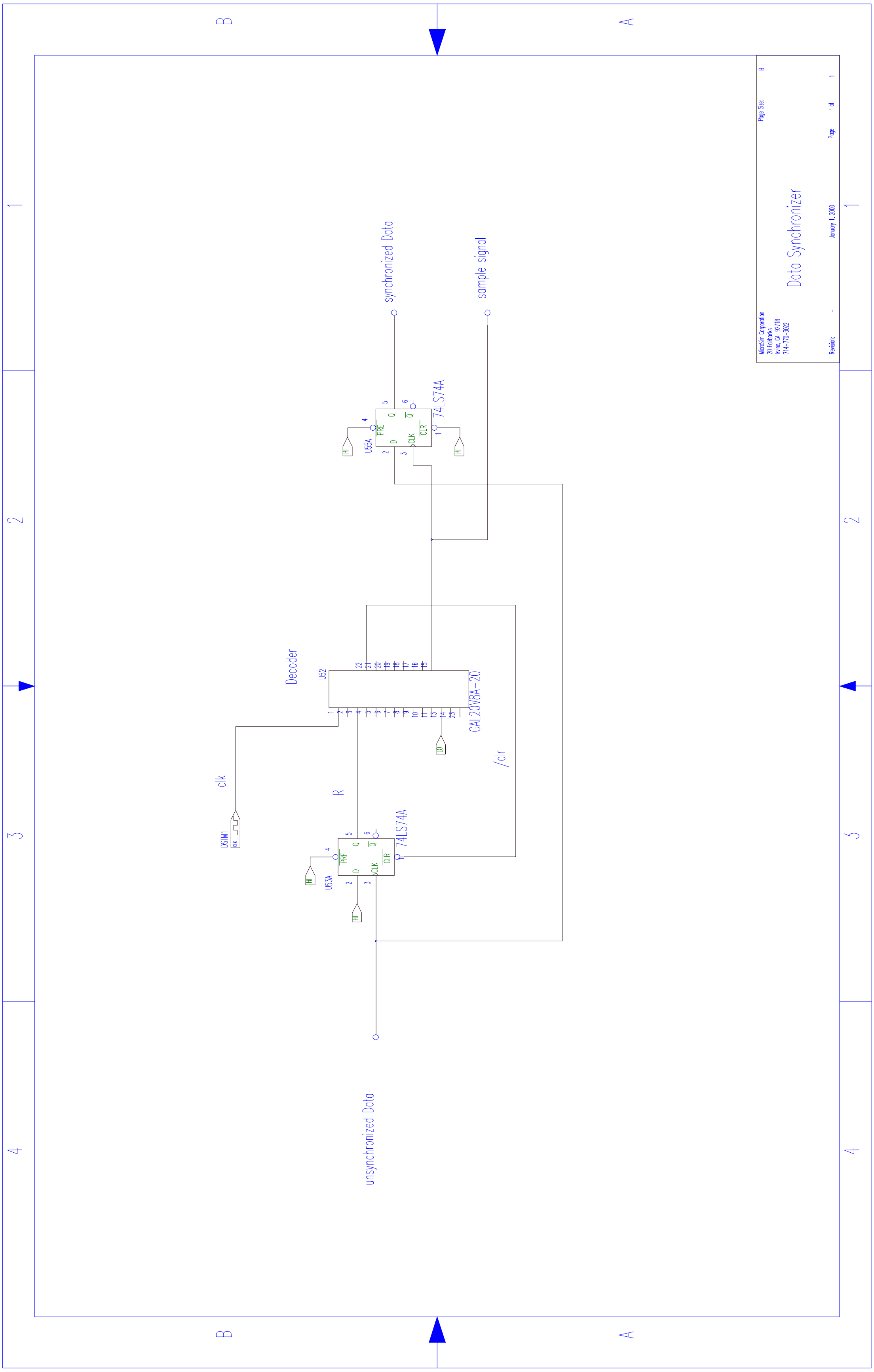

Fig. A.4 Data synchronizer.

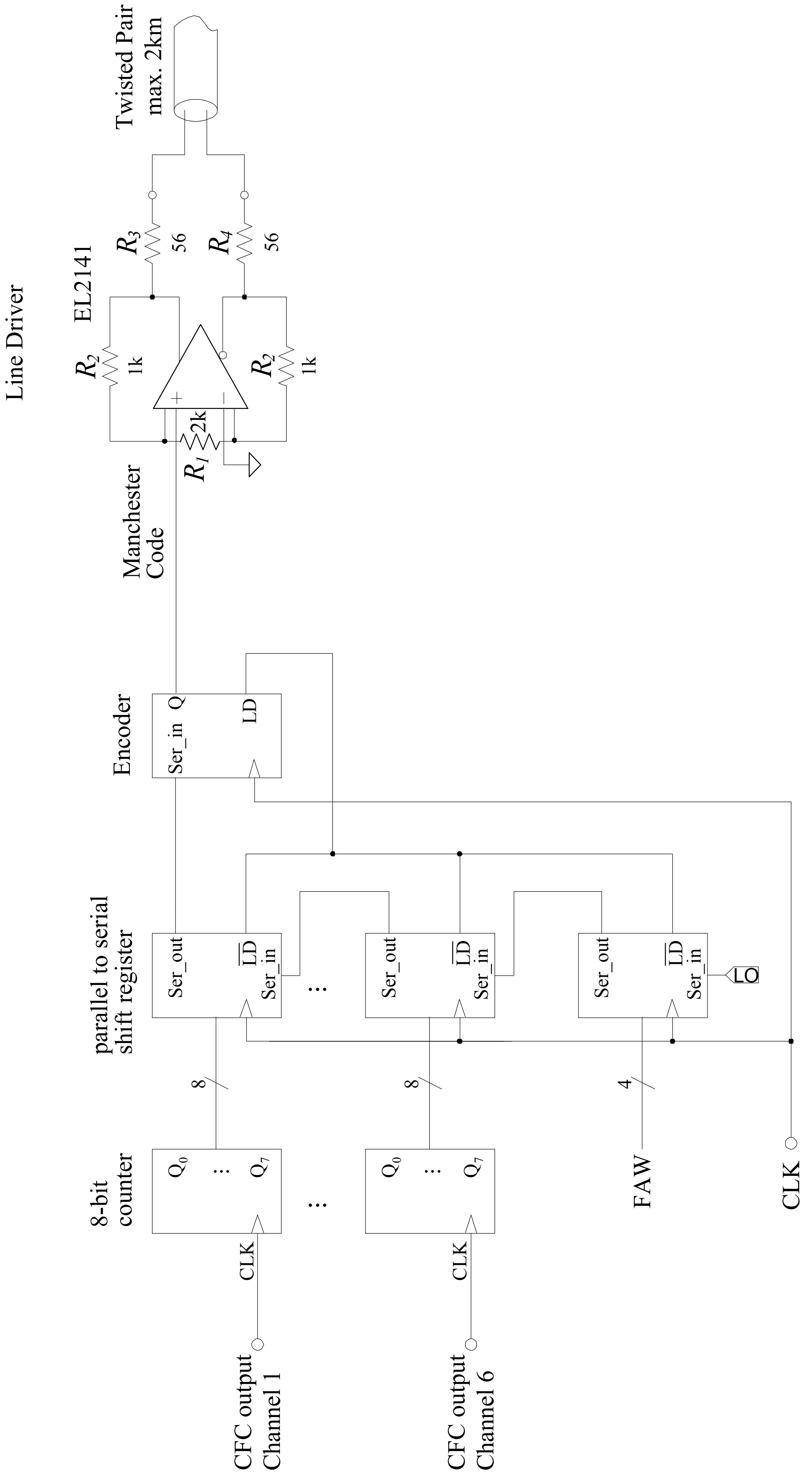

Fig. A.5 Schematic of the driver board.

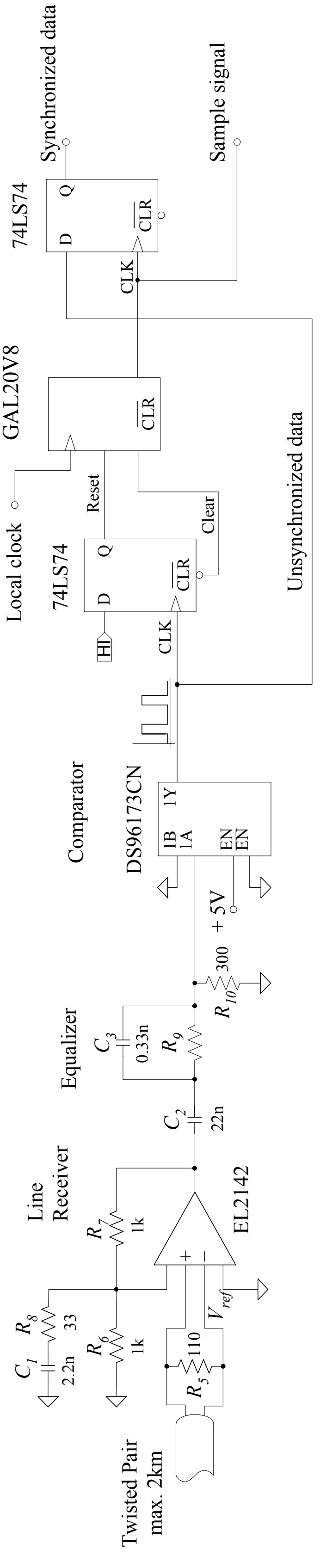

Fig. A.6 Schematic of the receiver board.

B Mathematica Files

B.1 Calculation of line parameters

The attenuation at two different frequencies is used to calculate R_{ac} and G_{ac} according to

$$|V_2| = e^{-\alpha \cdot z} \text{ with } \alpha = \frac{R}{2Z_0} + \frac{G_{ac}Z_0}{2} \tag{B.1}$$

$$R = \sqrt{{R_{dc}}^2 + {R_{ac}}^2} \tag{B.2}$$

where the line resistance also takes the DC resistance into account.

<<Graphics'Graphics'
(* Line parameters *)
Rdc = 37 10^{-3};
r = 0.564;
c = 53.1 10^{-12};
L = 0.653 10^{-6};
$\mathrm{Z}_0 = \sqrt{\frac{\mathrm{L}}{\mathrm{c}}}$
z = 1000;

Equation 5.22 is solved for the cable attenuation at 800 kHz and 1.2 MHz:

a1db = 11.56; ω1 = 2 Pi 800 10^3;
a2db = 15.67; ω2 = 2 Pi 1.2 10^6;

a1 = Log[$10^{a1db/20}$]/z;
a2 = Log[$10^{a2db/20}$]/z;

eq1 = a1 $== \frac{\sqrt{\mathrm{Rdc}^2+\mathrm{Rac}^2\ \omega 1}}{2\ \mathrm{Z}_0} + \frac{\mathrm{Gac}\ \omega 1\ \mathrm{Z}_0}{2}$;
eq2 = a2 $== \frac{\sqrt{\mathrm{Rdc}^2+\mathrm{Rac}^2\ \omega 2}}{2\ \mathrm{Z}_0} + \frac{\mathrm{Gac}\ \omega 2\ \mathrm{Z}_0}{2}$;
ans = Solve[{eq1, eq2}, {Rac, Gac}]

110.894
{{Gac→2.38056×10^{-12}, Rac→-0.0000639279},
{Gac→2.38056×10^{-12}, Rac→0.0000639279}}

Rac = (Rac /. ans[[2]]) (1 + I) $\sqrt{\omega}$
Gac = Gac /. ans[[2]] ω

The solutions for the characteristic impedance Z_0, R_{ac} and G_{ac} are

$$\begin{aligned} Z_0 &= 110.894\,\Omega \\ R_{ac} &= 6.393 \cdot 10^{-5} \cdot (1 + I) \cdot \sqrt{\omega}\ \Omega/\text{m} \\ G_{ac} &= 2.381 \cdot 10^{-12} \cdot \omega \text{ S/m} \end{aligned}$$

B.2 Transfer function approximation

In order to fit the attenuation of the NG18 to a rational function, the statistics package of Mathematica was used, which contains a nonlinear fit algorithm.

```
(* Cable attenuation @ 1.8 km *)
ω = 2*Pi*{0.001, 0.01, 0.02, 0.05, 0.1, 0.2, 0.5, 1, 2, 5, 10}*10^6;
AdB = {-0.15, -0.15, -0.15, -0.15, -0.28, -0.41, -0.80, -1.49, -2.33, -4.09, -6.43}*18;
Att = 10^(AdB/20);
ADC = 10^(AdB[[1]]/20);

(* Generation of a data list with attenuation / frequency pairs *)
data = {};
For[i = 1, i <= Length[ω], i++, data = Join[data, {ω[[i]], Att[[i]]}]]
data = Partition[data, 2];

(* Generation of a data list with attenuation in dB *)
datadB = {};
For[i = 1, i <= Length[ω], i++, datadB = Join[datadB, {ω[[i]], AdB[[i]]}]]
datadB = Partition[datadB, 2];

(* Nonlinear Fitting *)
<< Statistics‘NonlinearFit‘
(* A rational fit function with four poles *)
```

$$\text{fitfunc} = \text{ADC}^{*}\sqrt{\frac{1}{(1+\frac{x^2}{\omega p1})(1+\frac{x^2}{\omega p2})(1+\frac{x^2}{\omega p3})(1+\frac{x^2}{\omega p4})}};$$

```
(* Start values for the poles *)
p1 = 100 10^3; p2 = 500 10^3; p3 = 100 10^3; p4 = 100 10^3;

(* Nonlinear fit algorithm*)
fitcurve = NonlinearFit[data, fitfunc, x, {{ωp1, p1}, {ωp2, p2}, {ωp3, p3}, {ωp4, p4}}]
```

$$0.732825\sqrt{\frac{1}{(1+1.1339\times10^{-14}x^2)(1+1.1345\times10^{-14}x^2)(1+1.1459\times10^{-14}x^2)(1+1.2104\times10^{-12}x^2)}}$$

```
param = BestFitParameters /. NonlinearRegress[data, fitfunc, x,
{{ωp1, p1}, {ωp2, p2}, {ωp3, p3}, {ωp4, p4}}]

    {ωp1→9.3417×10^6, ωp2→-9.3886×10^6, ωp3→-908939, ωp4→-9.3911×10^6}

(* Fit curve *)
$TextStyle = {FontSize → 14};
Show[
dataplot = LogLinearListPlot[datadB, PlotStyle → PointSize[0.015], PlotRange → {{10^4, 5 10^7},
{-60, 0}}],
fitplot = LogLinearPlot[20*Log[10, fitcurve], {x,10^4, 5 10^7}, PlotRange → All, PlotStyle →
{{Thickness[0.008], RGBColor[1, 0.2, 0.7]}}], AxesLabel → {”ω[rad/s]”, ”A[dB]”},PlotLabel →
”Transfer function approximation”]
```

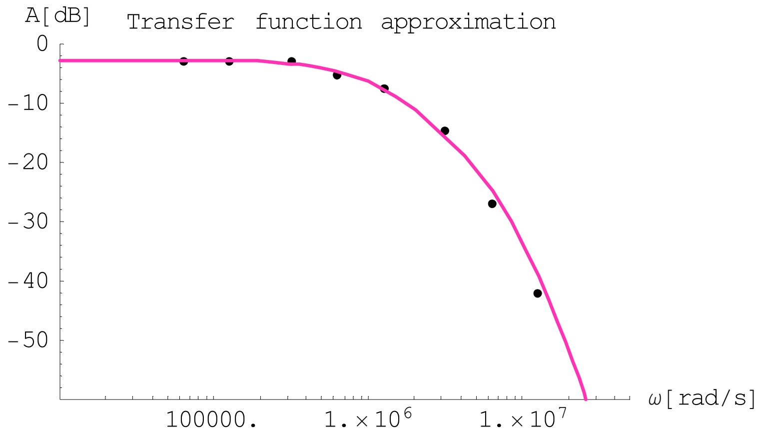

(* Extrating the fit parameters *)
$\omega 1$ = Abs[ωp1 /. param]; $\omega 2$ = Abs[ωp2 /. param]; $\omega 3$ = Abs[ωp3 /. param]; $\omega 4$ = Abs[ωp4 /. param];

$$\text{y} = \text{ADC}\,\frac{1}{(1\text{+I x}/\omega 1)\,(1\text{+I x}/\omega 2)\,(1\text{+I x}/\omega 3)\,(1\text{+I x}/1/\omega 4)};$$

(* Laplace Transfer Function I $\omega \longrightarrow$ s *)
H = y /. x $\longrightarrow$ s/I

$$\frac{0.7328251}{(1+1.0648\times 10^{-7}s)(1+1.0651\times 10^{-7}s)(1+1.0705\times 10^{-7}s)(1+1.1002\times 10^{-6}s)};$$

B.3 Cable attenuation with dielectric loss

The line paramters are taken from appendix B.1.

R=$\sqrt{\text{Rdc}^2+\text{Rac}^2}$;

(* conventional attenuation *)
$\gamma = \sqrt{(\text{R+I}\ \omega\ \text{L})*(\text{Gac} + \text{I}\ \omega\ \text{c})}$;
H = $e^{-\gamma\ \text{z}}$;
AttNG181 = 20*Log[10, Abs[H]];

(* skin effect and dielectric loss *)
AttSkin = 20*Log[10, Abs[$e^{\sqrt{(\text{R} + \text{I}\ \omega\ \text{L})\ \text{I}\ \omega\ \text{c}}\ \text{z}}$]];
Attdiel = 20*Log[10, Abs[$e^{\sqrt{\text{I}\ \omega\ \text{L}\ (\text{Gac} + \text{I}\ \omega\ \text{c})}\ \text{z}}$]];

(* modified dielectric loss *)
tanδ = Gac/c;

0.0448316

m = 0.8;
τ' = (2 Pi 10^6)$^{(1-m)}$/Cos[m*Pi/2];

74.0719

Hpol = ADC*$e^{-\sqrt{(\text{Rac} + \text{I}\ \omega\ \text{L})*((\text{I}\ \omega)^m\ \text{tand}\delta\ \tau'\ \text{c} + \text{I}\ \omega\ \text{c})}*\ \text{z}}$;

```
AttMod = 20*Log[10, Abs[Hpol]];
```

The measured data from appendix B.2 is taken but the attenuation was calculated for a length of 1 km.

```
dataplot = LogLinearListPlot[data, PlotStyle → PointSize[0.01], PlotRange →
{{10^4, 10^8}, {-70, 0}}, AxesLabel → {"ω[rad/s]", "A[dB]"}]
```

The attenuation can be plotted for different models. In this case, the measured data is compared with the conventional attenuation and the modified dielectric loss.

```
graphs = Show[
NG18Calc = LogLinearPlot[{AttNG181, Attmod}, {ω, 1000, 2 Pi 10^7}, PlotStyle →
{{Thickness[0.005], RGBColor[1, 0, 0]}, {Thickness[0.005], RGBColor[0, 1, 0]},
{Thickness[0.005], RGBColor[0, 0, 1]}}, PlotRange → {-60, 0}, GridLines → Automatic,
AxesLabel → {"ω[rad/s]", "A[dB]"}], PlotLabel → StyleForm["Attenuation of the NG18 at 1 km",
TraditionalForm, FontSize → 18]],
dataplot]

ShowLegend[graphs,
{{{Graphics[{RGBColor[0, 0, 0], PointSize[0.2], Point[{0, 0}], Point[{0.5, 0}], Point[{1, 0}]}],
StyleForm["Attenuation NG18", TraditionalForm, FontSize → 12]},
{Graphics[{RGBColor[1, 0, 0], Thickness[0.1], Line[{{0, 0}, {1, 0}}]}],
StyleForm["conventional diel. loss", TraditionalForm, FontSize → 12]},
{Graphics[{RGBColor[0, 1, 0], Thickness[0.1], Line[{{0, 0}, {1, 0}}]}],
StyleForm["mod. dielectric loss, m=0.8", TraditionalForm, FontSize → 12]}}, LegendPosition →
{-0.8, -0.4} , LegendSize → {0.7, 0.2}, LegendTextSpace → 4.5}]
```

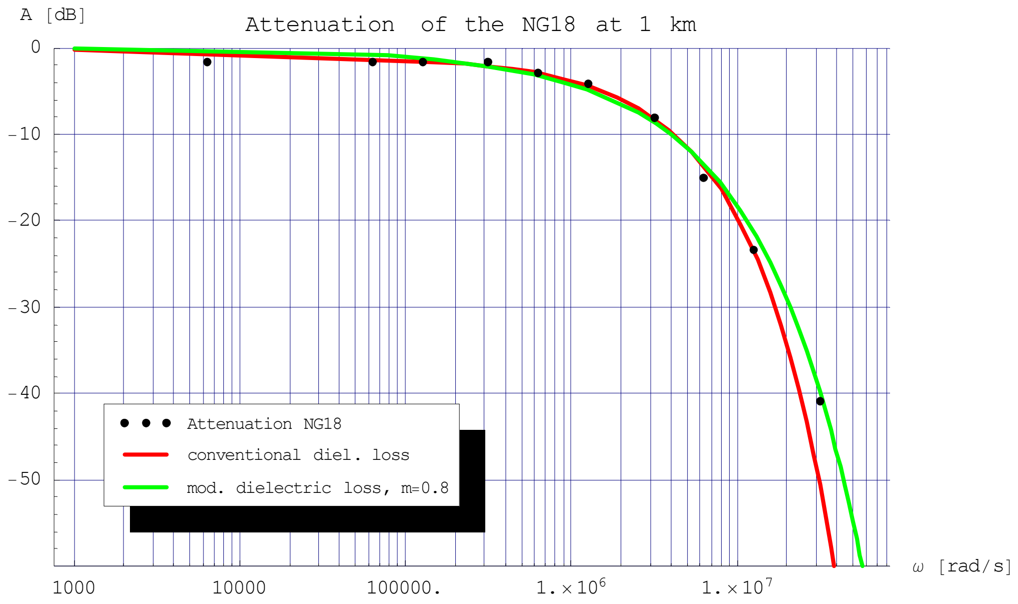

B.4 Calculation of the impulse / step response

The step response was calculated numerically with the inverse Fourier transform. The line parameters were taken from appendix B.1, the modified dielectric loss model was take from appendix B.3 and the transfer function model from appendix B.2.

(* Cable length *)
z = 1800;

(* to fit the measured data, the DC attenuation and driver gain must be taken into account *)
Gain = 1.48;
ADC = Gain*0.732825;

(* some models don't consider the delay of the cable thus it must be added manually *)
td = 9.8 10^{-6};

(* Analytic step response, according to [Rie-70] and [Cur-85] *)
(* Skin effect only *)
A = $\frac{\text{Rac}}{\sqrt{I\omega}2Z_0}$ z;
Hskin = ADC $e^{-A\sqrt{s}}$

$0.732825\ e^{-0.000733734\sqrt{s}}$

hskin = InverseLaplaceTransform[Hskin, s, t];
uskin = Simplify[InverseLaplaceTransform[Hskin/s, s, t]]*UnitStep[t] /. t → t - td

$1.48\ (0.732825 - 0.732825\ \text{Erf}[\frac{0.000366867}{\sqrt{-1/100000+t}}])\ \text{UnitStep}[-\frac{1}{100000}+t]$

(*Dielectric Loss*)
B $= \frac{\text{Gac}\ Z_0}{2}$;
Hdiel = $e^{-B\ \omega\ z}$;

hdiel = $\sqrt{\frac{2}{\pi}}$ InverseFourierCosTransform[Hdiel, ω, t];
udiel = Integrate[hdiel /. t → t - x, {x, 0, t}]

0.63662 ArcTan[4.20891 × 10^6 t]

(* Conventional Dielectric Loss *)
Hconv = ADC*$e^{-\sqrt{(\text{Rac} + \text{I}\ \omega\ \text{L})*(\text{Gac} + \text{I}\ \omega\ \text{c})}*\ z}$;

The following procedure calculates the input bit pattern. It will be used throughout the rest of the simulations.

(* Input bit pattern *)
x = {1, 1, 1, 1, 1, 1, 1, 1, 1, 1};
Tb = 5 10^{-6};
dp = 100;
Ts = Tb/dp;
T = Tb*Length[x];

u = {};

$TextStyle = {FontSize → 14};
For[n = 0, n < Length[x], n++; u = Join[u, Table[x[[n]], {a, 1, dp}]]];

```
V1 = ListPlot[Table[{b/Length[u]*T, u[[b + 1]]}, {b, 0, Length[u] - 1}],
PlotJoined → True, AxesLabel → {"t[s]", "V₁"}]
u1 = Delete[u, Length[u]];
```

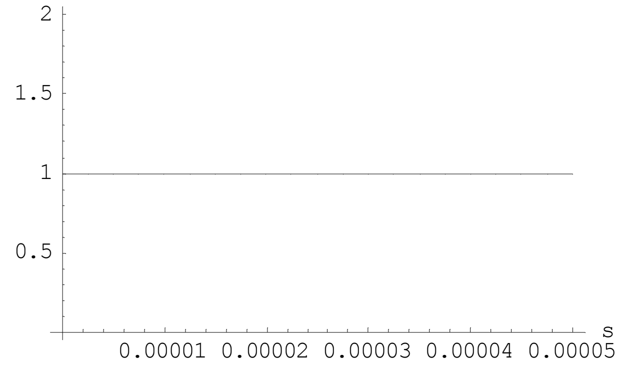

The real input step is modeled as a step to 80% of the final value and a superposed exponential function with a time constant of 8 μs.

```
(* The input voltage isn't an ideal step. *)
time = Table[a, {a, 0, T - 2*Ts, Ts}];
badstept = (1 - 0.2 e^(-t/(810^-6)))*UnitStep[t] /. t → time;

badplot = ListPlot[Table[{b/Length[u]*T, badstept[[b + 1]]}, {b, 0, Length[u] - 2}],
PlotRange → {0, 1}, PlotStyle → {RGBColor[0, 0.7, 1]}, AxesLabel → {"t[s]","V₁[V]"},
PlotLabel → "Real input step", PlotJoined -> True]]
```

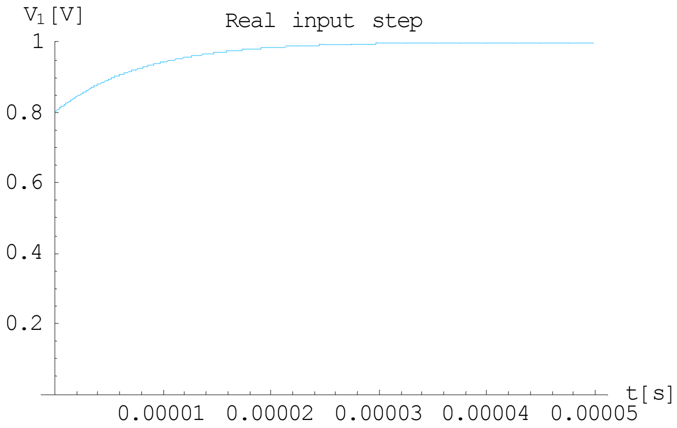

The step response is derived numerically by an inverse Fourier transform. This algorithm is also used for the calculation of the response to an arbitrary signal. In the following example. the step response of the transfer function model is calculated. If the response of another model (skin effect only, modified dielectric loss) is desired, the respective transfer functions (Hskin, Hpol) must be used.

```
(* Discrete Fourier transform *)
(* Replacing Htf by Hskin or Hpol leads to the step response due to skin effect or due to
the modified dielectric loss *)
Hjω = Htf*e^(-s td) /. s → I ω;

fsample = 1/Ts;
```

```
sp = dp*Length[x];
freq = Table[fsample/2*a/(sp/2), {a, 0, sp/2 - 1}];
Hd = Hjω /. ω → 2 π freq;
Hd = Join[Hd, Reverse[Conjugate[Hd]]];
Hd = Delete[Hd, Length[Hd]];
ListPlot[Abs[Hd]];
```

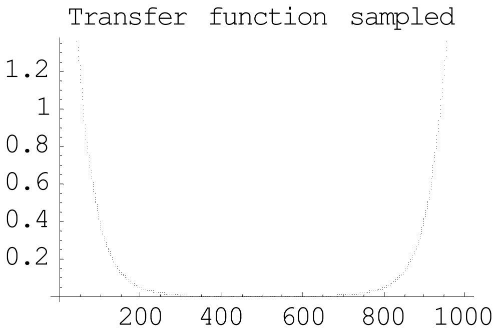

```
(* Impulse Response *)
imp = InverseFourier[Hd, FourierParameters → {1,- 1}];
ListPlot[Table[{b/Length[u]*T, imp[[b + 1]]}, {b, 0, Length[u] - 2}],
(PlotStyle → {Thickness[0.005], RGBColor[0, 0, 1]}, AxesLabel → {”t[s]”, ”V2[V]”},
PlotRange → {{0, 30 10^-6}, {0, 0.08 }}, PlotLabel → ”Impulse response”, PlotJoined → True]
```

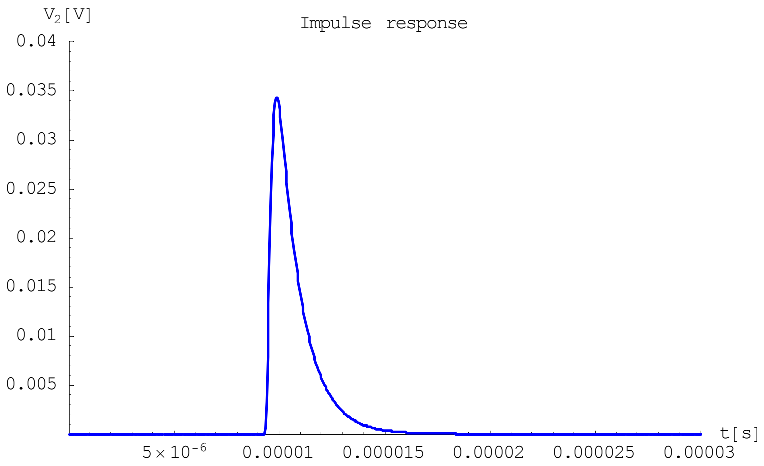

```
(* Inverse Fourier with zero padding to examine the transient respons, see [Bra-86]*)
zeros = Table[0, {a, Length[Hd]}];
Hdz = Join[imp, zeros];

(* exchange badstept with u1 to simulate an ideal input step function *)
uz = Join[badstept, zeros];

(* The step response yfft is calculated, it will be used also later *)

yfft = InverseFourier[Fourier[Hdz]*Fourier[uz], FourierParameters → {-1, 1}];
CalcPlot = ListPlot[Table[{b/sp*T, yfft[[b + 1]]}, {b, 0, sp - 1, 1}],
PlotStyle → {RGBColor[1, 0, 1], Thickness[0.01], PointSize[0.02]}, PlotRange → {{0, T}, {0, 1}},
PlotJoined → True];

(* Measured Step Response *)
SetDirectory[”g:/CERN/mydocs/diploma thesis/scope/step response/”];
y = ReadList[”Step1800.csv”, Number, RecordSeparators → {”,”}];
xoffset = y[[1]];
```

```
yoffset = y[[2]];
For[i = 1, i <= Length[y], i = i + 2, y[[i]] = y[[i]] - xoffset]
For[i = 2, i <= Length[y], i = i + 2, y[[i]] = y[[i]] - yoffset]
y = Partition[y, 2];
MeasPlot = ListPlot[y, PlotRange → {{0, T/4}, {0, 1.4}}, PlotJoined → True]

graphs = Show[CalcPlot, MeasPlot, AxesOrigin → {0, 0}, AxesLabel →{"t[s]", "V2[V]"},
PlotLabel → "Step response"]

<< Graphics‘Legend‘
ShowLegend[graphs,
{{{Graphics[{RGBColor[0, 0, 0], Thickness[0.1], Line[{{0, 0}, {1, 0}}]}],
StyleForm["Measured signal", TraditionalForm, FontSize → 12]},
{Graphics[{RGBColor[1, 0, 0], Thickness[0.1], Line[{{0, 0}, {1, 0}}]}],
StyleForm["Transfer function, real step", TraditionalForm, FontSize → 12]}},
LegendPosition → {-0.05, -0.4} , LegendSize → {0.97, 0.2}, LegendTextSpace → 7}]
```

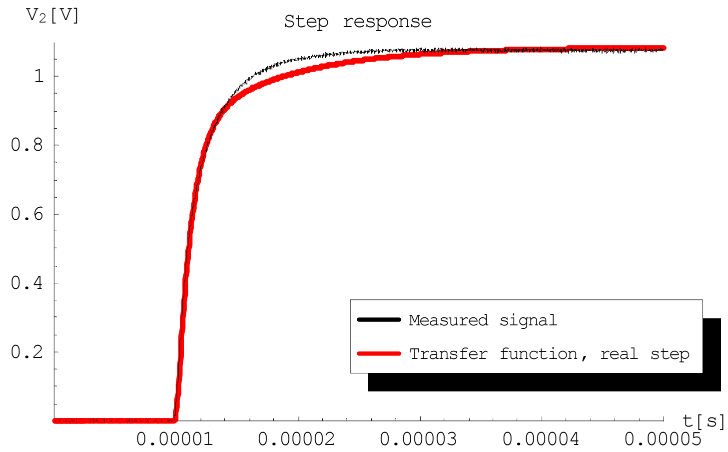

To calculate the step response according to [Cur-85] and [Rie-70], the impulse response due to the dielectric loss has to be convolved with the step response only due to the skin effect. Only small modifications in the above expressions are needed.

```
(* Htf is replaced by Hskin to calculate the step response yfft due to the skin effect *)
Hjω = Hskin*e^(-s td) /. s → I ω;

(* The discrete impulse response of the dielectric loss is calculated*)
hdield = hdiel /. t → time;

(* The step response of Hskin is convolved with hdield; however, the amplitude must be scaled *)
yconv = 1/1.2/10^7*Re[ListConvolve[yfft, hdield, {1, -1}, 0]];

CalcPlot1 = ListPlot[Table[{b/sp*T, yconv[[b]]}, {b, 1, sp - 1, 1}], PlotStyle → {RGBColor[1, 0, 0],
Thickness[0.01]}, PlotRange → {{0, T}, {-0.01, 1.2}}, PlotJoined → True];

graphs = Show[CalcPlot, CalcPlot1, SquareMeas, AxesLabel → {"t[s]", "V2[V]"}, PlotRange →
{{0, T/2}, {-0.01, 1.2}}];

ShowLegend[graphs,
{{{Graphics[{RGBColor[0, 0, 0], Thickness[0.1], Line[{{0, 0}, {1, 0}}]}], StyleForm["Measured
signal", TraditionalForm, FontSize → 12]},
{Graphics[{RGBColor[0, 1, 0], Thickness[0.1], Line[{{0, 0}, {1, 0}}]}], StyleForm["Skin effect
```

only", TraditionalForm, FontSize → 12]},
{Graphics[{RGBColor[1, 0, 0], Thickness[0.1], Line[{{0, 0}, {1, 0}}]}], StyleForm["Skin effect diel. loss [Cur-85]", TraditionalForm, FontSize → 12]}},
LegendPosition → {-0.2, -0.4} , LegendSize → {1.1, 0.2}, LegendTextSpace → 9}]

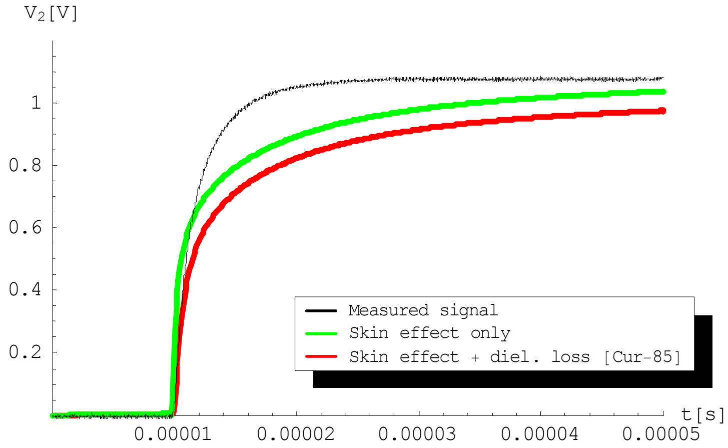

B.5 Line equalizer

To simulate the equalizer, the transfer function of the receiver was derived. Again, the line parameters were taken from appendix B.1, while the transer function model in appendix B.2 is used to describe the cable.

(* Transfer function of the receiver EL2142C *)
A0 = $10^{75/20}$;
ft = 200 10^6;
H0 = $\frac{\mathrm{A0}}{1+s/(2\,\pi\ \mathrm{ft/A0})}$;

(* Feedback elements *)
R8 = 33; C1 = 2.2 10^{-9}; R6 = 1000; R7 = 1000;
Z3 = R8 + $\frac{1}{\mathrm{sC1}}$;
Z1 = $\frac{\mathrm{R6\ Z3}}{\mathrm{R6+Z3}}$;
b = $\frac{\mathrm{Z1}}{\mathrm{R7+Z1}}$;
vs = b H0;
Heq = Simplify[$\frac{1}{\mathrm{b}}\ \frac{\mathrm{vs}}{1+\mathrm{vs}}$];

Eq = LogLogPlot[Abs[Heq/s /. s → ω/I], {ω, 2 π 1000, 2 π 200 10^6}, PlotRange → {{10^4, 2 10^9}, {0.1, 35}}, PlotStyle → {{Thickness[0.008], RGBColor[1, 0, 0]}, {Thickness[0.008], RGBColor[0, 1, 0]}, {Thickness[0.008], RGBColor[0, 0, 1]}}, PlotPoints → 1000, AxesLabel → {"ω[rad/s]", "Gain"}];

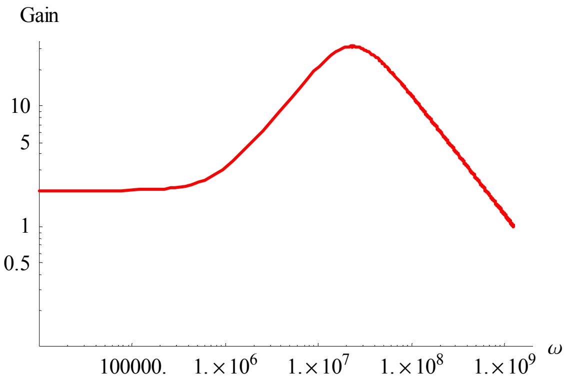

```
(* Improvement of the signal bandwidth with the equalizer *)
Hcable1 = Hcable /. s → ω/I;
Heq1 = Heq /. s → ω/I;

graph = LogLogPlot[{Abs[Hcable1], Abs[Heq1], Abs[Hcable1] Abs[Heq1]}, {ω, 2 π 10,
2 Pi 150 10^6}, PlotRange → {{1000, 200 10^6}, {0.1, 35}}, PlotStyle → {{Thickness[0.005],
RGBColor[1, 0, 0]}, {Thickness[0.005], RGBColor[0, 1, 0]}, {Thickness[0.005],
RGBColor[0, 0, 1]}}, PlotPoints → 1000, AxesLabel → {"ω[rad/s]", "Gain"}];

ShowLegend[graph,
{{{Graphics[{RGBColor[1, 0, 0], Thickness[0.1], Line[{{0, 0}, {1, 0}}]}], StyleForm["Cable
Attenuation", TraditionalForm, FontSize → 12]},
{Graphics[{RGBColor[0, 1, 0], Thickness[0.1], Line[{{0, 0}, {1, 0}}]}], StyleForm["Equalizer",
TraditionalForm, FontSize → 12]},
{Graphics[{RGBColor[0, 0, 1], Thickness[0.1], Line[{{0, 0}, {1, 0}}]}], StyleForm["Equalized gain",
TraditionalForm, FontSize → 12]}},
LegendPosition → {-0.8, 0.3} , LegendSize → {0.7, 0.2}, LegendTextSpace → 2.7}];
```

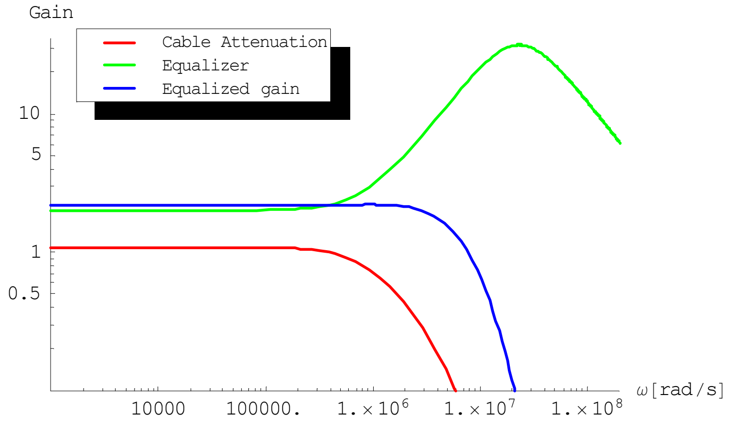

```
(* Calculation of the cut - off frequencies *)
eq1 = Abs[Hcable1] == ADC/√2;
ω1 = ω /. FindRoot[eq1, {ω, 1000, 10^4}]

    884752.

eq2 = Abs[Hcable1 Heq1] == (Abs[Hcable1Heq1]/.ω→0)/√2;
```

```
ω2 = ω /. FindRoot[eq2, {ω, {5 10^6, 10^7}}]
```

```
      5.06606 × 10^6
```

```
ω2/ω1
```

```
      5.72596
```

```
(* Step response with the equalizer *)
utf = InverseLaplaceTransform[Hcable/s, s, t];
ueq = Re[InverseLaplaceTransform[Hcable*Heq/s, s, t]];

Plot[{utf, ueq}, {t, 0, 10 10^-6}, PlotStyle → {{Thickness[0.007], RGBColor[1, 0, 0]},
{Thickness[0.007], RGBColor[0, 1, 0]}, {Thickness[0.005], RGBColor[0, 0, 1]}},
AxesLabel → {"t[s]", "V2[V]"}];
```

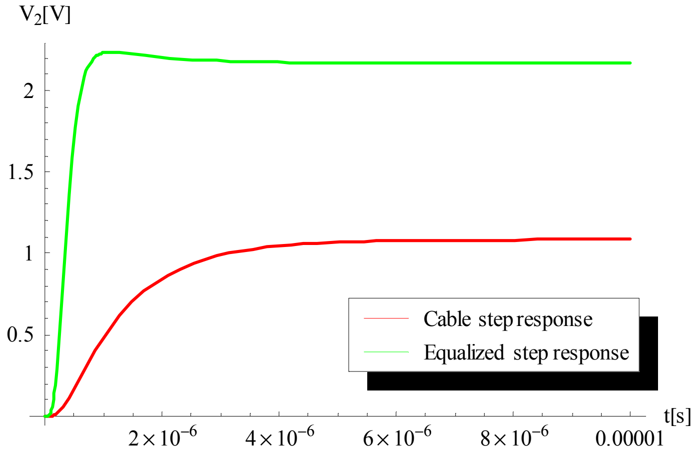

```
(* Calculation of 10% - 90% rise time *)
(* no equalizer *)
eq10 = utf == (0.1 utf /. t → 1);
t10 = t /. FindRoot[eq10, {t, 10^-6}];
eq90 = utf == (0.9 utf /. t → 1);
t90 = t /. FindRoot[eq90, {t, 10^-6}];
Tfrise = t90 - t10
```

```
      2.47366 × 10^-6
```

```
(* with equlizer *)
eq10 = ueq == (0.1 ueq /. t → 1);
t10 = t /. FindRoot[eq10, {t, 4 10^-7, 5 10^-7}];
eq90 = ueq == (0.9 ueq /. t → 1);
t90 = t /. FindRoot[eq90, {t, 4 10^-7, 5 10^-7}];
Eqrise = t90 - t10
```

```
      4.09006 10^-7
```

```
(* Improvement in rise time *)
Tfrise/Eqrise
```

```
      6.04798
```

(* Calculation of the rise time from the cut - off frequency
$t_r \approx \frac{2.2}{\omega_{3dB}} = \frac{0.35}{f_{3dB}}$, only exact for a single pole transfer function *)

```
(* Transfer function *)
```

```
2.2/ω1

    2.48657 10^-6

(* Equalizer *)
2.2/ω2

    4.34263 10^-7
```

The equalized step response is compared with the measured one. To fit the long-term amplitude of the step response, the equalizer gain has to be mulitplicated by 0.95. Again, the same steps are performed as in appendix B.4.

```
(* Comparison with measured step response *)
(Hjω = Htf*0.95*Heq*e^-s td /. s → I ω;
```

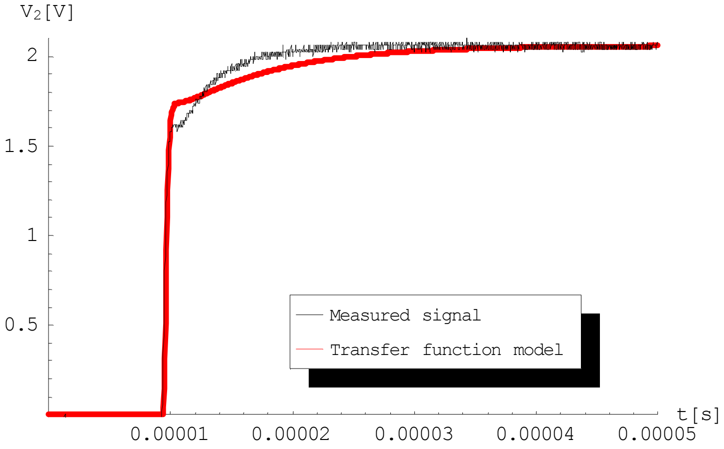

Now the influence of the second equalizer is examined.

```
(* RC Equalizer *)
R9 = 1000; R10 = 300; C3 = 0.33 10^-9;
Z3 = 1/s/C3;
Z2 = R9 Z3/(R9 + Z3);
G2 = Simplify[R10/(R10 + Z2)];
G21 = G2 /. s → ω/I;

Eq2 = LogLogPlot[Abs[G21], {ω, 2 Pi 1000, 2 Pi 200 10^6}, PlotRange → {{10000, 15*200*10^6},
{0.1, 2}}, PlotStyle → {{Thickness[0.008], RGBColor[0, 0, 1]}, {Thickness[0.008],
RGBColor[0, 1, 0]}}, PlotPoints → 1000, AxesLabel → {"ω","Gain"}]

graph = LogLogPlot[{Abs[Hcable1], Abs[Hcable1]*Abs[Heq1],
Abs[Hcable1]*Abs[Heq1]*Abs[G21]},
{ω, 2 Pi 10, 2 Pi 150 10^6}, PlotRange → {{1000, 200*10^6}, {0.1, 35}}, PlotStyle →
{{Thickness[0.005], RGBColor[1, 0, 0]}, {Thickness[0.005], RGBColor[0, 1, 0]},
{Thickness[0.005], RGBColor[0, 0, 1]}, {Thickness[0.005], RGBColor[1, 0, 1]}},
PlotPoints → 1000, AxesLabel → {"ω[rad/s]", "Gain"}];

ShowLegend[graph,
{{{Graphics[{RGBColor[1, 0, 0], Thickness[0.1], Line[{{0, 0}, {1, 0}}]}], StyleForm["Cable
Attenuation", TraditionalForm, FontSize → 12]},
{Graphics[{RGBColor[0, 0, 1], Thickness[0.1], Line[{{0, 0}, {1, 0}}]}], StyleForm["First equalizer",
```

```
TraditionalForm, FontSize → 12]},
{Graphics[{RGBColor[0, 1, 0], Thickness[0.1], Line[{{0, 0}, {1, 0}}]}], StyleForm[”Second
equalizer”, TraditionalForm, FontSize → 12]}},
LegendPosition → {-0.8, 0.25} , LegendSize → {0.65, 0.2}, LegendTextSpace → 5}]
```

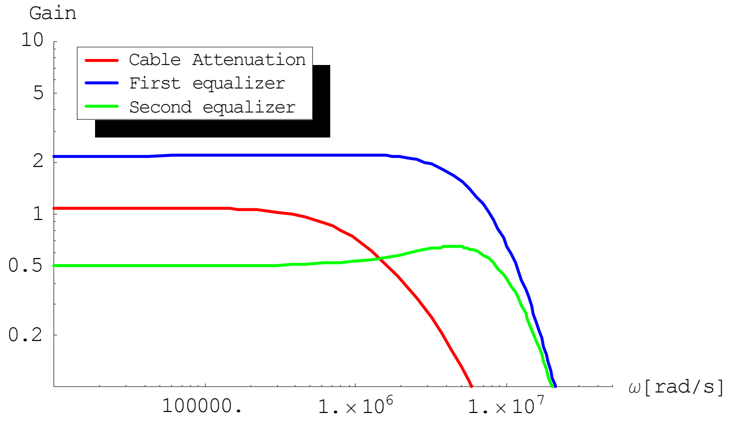

```
(* Cut - off frequency after the RC - equalizer *)
eq3 = Abs[Hcable1*Heq1*G21] == (Abs [Hcable1*Heq1*G21] /. ω → 0)/√2;
ω3 = ω /. FindRoot[eq3, {ω, {8*10^6, 10^7}}]
```

```
1.13737 × 10^7
```

```
(* Improvement of the cut-off frequency*)
ω3/ω2
```

```
2.24508
```

B.6 Calculation of a square wave / Manchester encoded signal

The calculations in appendix B.4 and B.5 are used to calculate the distortion of a square wave and an arbitrary Manchester encoded signal. The bit pattern is generated in the same way as in the calculation of the step response.

```
(* Input bit pattern, 2 MHz square wave *)
x = {1 ,0, 1, 0, 1, 0, 1, 0, 1, 0};
Tb = 0.25 10^-6;
```

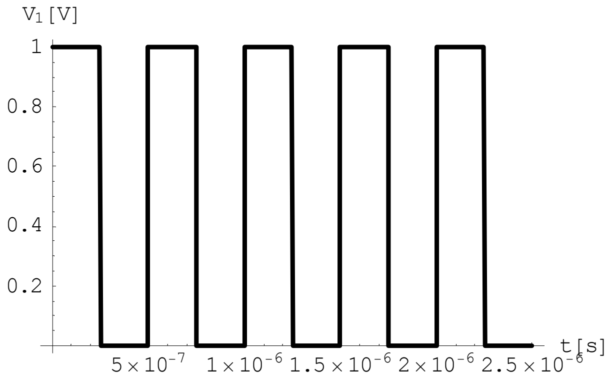

The measured square wave is compared with the transfer function model. To align the two curves, the delay time has to be adjusted.

```
(* Fourier transform *)
Hjω = Htf e^(+s 0.056 td) /. s → I ω;
```

Only the steady state solution should be examined. Therefore, neither the bit pattern nor the impulse response is padded with zeros [Bra-86].

```
V2 = InverseFourier[Fourier[u1]*Hd];
CalcPlot = ListPlot[Table[{b/sp*T, V2[[Length[V2] - b - 1]]}, {b, 0, sp - 1, 1}], PlotStyle →
{RGBColor[1, 0, 0], PointSize[0.02]}, PlotRange → {{0, 1.03 T}, {0.5, 0.6}}, PlotJoined → False];

{Max[V2], Min[V2], Max[V2] - Min[V2]}
    {0.55392, 0.531876, 0.0220445}

(* Measured square wave *)
SetDirectory["g:/CERN/mydocs/diploma thesis/scope/square wave/"];
y = ReadList["18_2M_noEq.csv", Number, RecordSeparators → {","}];
xoffset = y[[1]];
yoffset = -0.05 + 0*y[[2]];
For[i = 1, i <= Length[y], i = i + 2, y[[i]] = y[[i]] - xoffset]
For[i = 2, i <= Length[y], i = i + 2, y[[i]] = y[[i]] - yoffset]
y = Partition[y, 2];

SquareMeas = ListPlot[y, PlotRange → {{0, T}, {0.5, 0.6}}, PlotJoined → True]

graphs = Show[CalcPlot, SquareMeas, AxesOrigin → {0, 0.5}, AxesLabel → {"t[s]", "V2[V]"},
PlotLabel → "Square wave 2 MHz", Epilog → {RGBColor[1, 0, 0], Line[{{2 10^-6, 0.575},
{1.65 10^-6, 0.55}}], Text["Vpp = 22 mV", {2 10^-6, .58}, {-1, 0}]}]

<< Graphics`Legend`
ShowLegend[graphs,
{{{Graphics[{RGBColor[0, 0, 0], Thickness[0.1], Line[{{0, 0}, {1, 0}}]}], StyleForm["Measured
signal",
TraditionalForm, FontSize → 12]},
{Graphics[{RGBColor[1, 0, 0], PointSize[0.2], Point[{0.3, 0}], Point[{0.4, 0}], Point[{0.5, 0}]}],
StyleForm["Transfer function model", TraditionalForm, FontSize → 12]}},
LegendPosition → {-0.7, 0.2}, LegendSize → {0.8, 0.2}, LegendTextSpace → 6}]
```

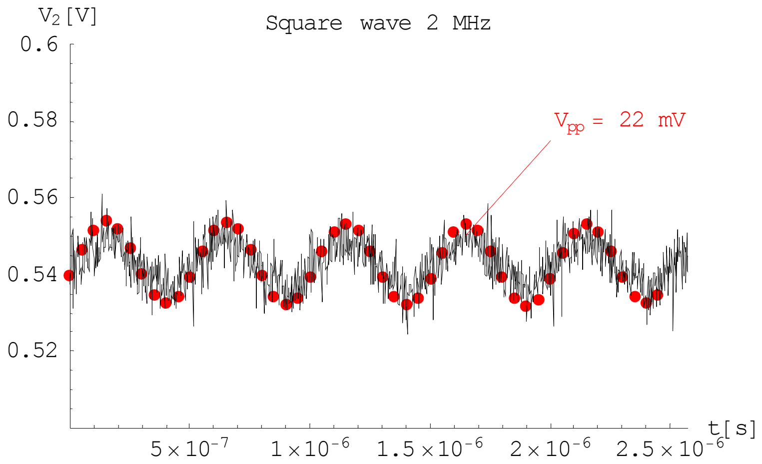

A square wave can be tested with the equalizer can be done by inserting the transfer function of the equalizer as it was already shown in the calculation of the equalized step response.

$$Hj\omega = Htf{*}0.95{*}Heq{*}e^{+s\,0.056\,td}\ /.\ s \rightarrow I\,\omega;$$

The calculation of a Manchester encoded signal uses the same steps as the square wave calculation. The input bit pattern was chosen to represent an arbitrary encoded signal, including the FAW (1100 – not encoded).

```
(* Calculation of a Manchester encoded signal *)
(* Input bit pattern, Manchester Code *)
x = {1 , 0, 1, 1, 1, 1, 0, 0, 0, 0, 1, 0, 0, 1, 1, 0, 1, 0, 0, 1, 1, 0};
```

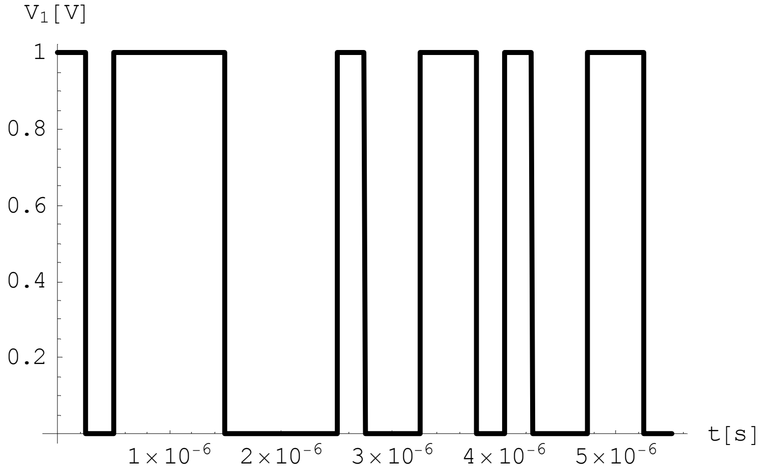

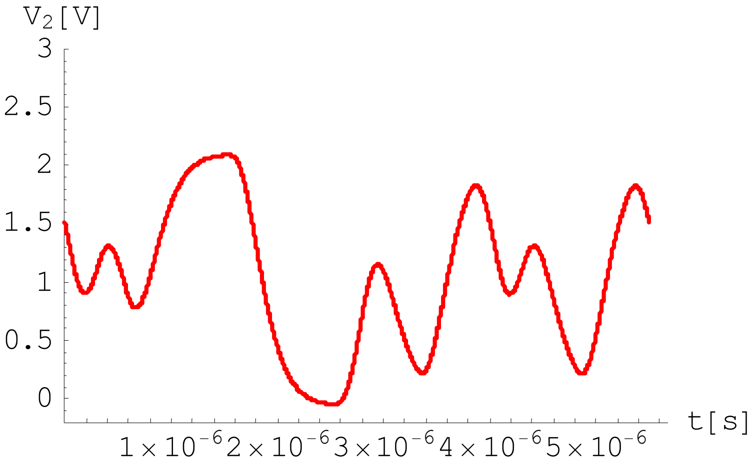

Adding the second equalizer $G_2(j\omega)$ reduces the amplitude but avoids a long settling time.

Hjω = Htf*0.95*G2*Heq /. s → I ω;

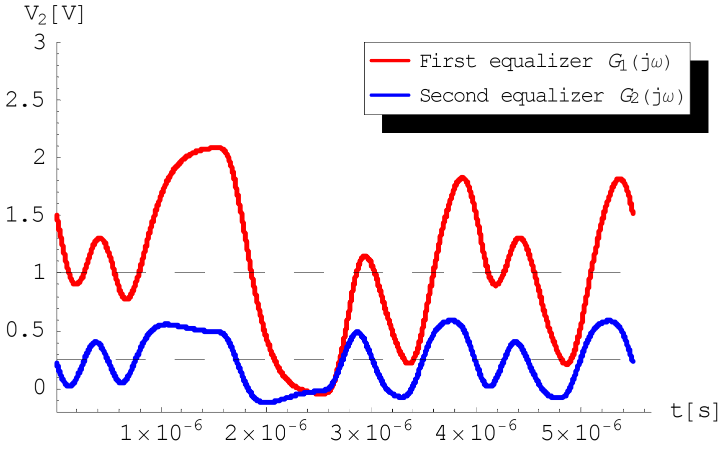

C GAL Files

C.1 Encoder

The encoder loads the counter values into the registers and produces the Manchester Code. Since the prototype board consists of 2 × 8-bit channels and one 4-bit FAW, a 5-bit counter that counts until 20 is sufficient. The load command $\overline{\text{PL.r}}$ is set 1 at counter = 18 and the registered output is set one clock cycle later at counter = 19. To avoid an encoding of the FAW, the output Dec_en.r is used. As long as it is 0 the data is not encoded. Table C.1 shows the logic table for the counter.

Table C.1 Logic table to load the counter values into the registers and to encode the data

No.	z_4	z_3	z_2	z_1	z_0	z'_4	z'_3	z'_2	z'_1	z'_0	/PL.r	Dec_En.r
0	0	0	0	0	0	0	0	0	0	1	0	0
1	0	0	0	0	1	0	0	0	1	0	0	0
2	0	0	0	1	0	0	0	0	1	1	0	1
3	0	0	0	1	1	0	0	1	0	0	0	1
4	0	0	1	0	0	0	0	1	0	1	0	1
5	0	0	1	0	1	0	0	1	1	0	0	1
6	0	0	1	1	0	0	0	1	1	1	0	1
7	0	0	1	1	1	0	1	0	0	0	0	1
8	0	1	0	0	0	0	1	0	0	1	0	1
9	0	1	0	0	1	0	1	0	1	0	0	1
10	0	1	0	1	0	0	1	0	1	1	0	1
11	0	1	0	1	1	0	1	1	0	0	0	1
12	0	1	1	0	0	0	1	1	0	1	0	1
13	0	1	1	0	1	0	1	1	1	0	0	1
14	0	1	1	1	0	0	1	1	1	1	0	1
15	0	1	1	1	1	1	0	0	0	0	0	1
16	1	0	0	0	0	1	0	0	0	1	0	1
17	1	0	0	0	1	1	0	0	1	0	0	1
18	1	0	0	1	0	1	0	0	1	1	1	0
19	1	0	0	1	1	0	0	0	0	0	0	0
20	1	0	1	0	0	x	x	x	x	x	x	x

To generate the Manchester Code, an XOR conjunction is needed. It is also programmed into the GAL. The output Pre_code contains spikes, which are removed by a D flip-flop as shown in Fig. A.3. The boolean expressions for the counter variables $z_{2..0}$ and the output variables Dec_en.r and $\overline{\text{PL.r}}$ are written into a text file. After compiling it to a JEDEC file, it is programmed into the GAL.

```
Manchester Encoder for two 8-bit channels + 4-bit FAW

*IDENTIFICATION enc2x8;

*TYPE GAL20V8;

*PINS

% Input %
CLK = 2,
Ser_In = 3,

% Output %
Pre_Code.o = 22,
/pl.r = 21,
z4.r = 20,
z3.r = 19,
z2.r = 18,
z1.r = 17,
z0.r = 16,
Dec_En.r = 15;

*BOOLEAN-EQUATIONS
z4 = /z4 & z3 & z2 & z1 & z0 + z4 & /z1 + z4 & /z0;
z3 = /z4 & /z3 & z2 & z1 & z0 + z3 & /z2 + z3 & /z1 + z3 & /z0;
z2 = z2 & /z1 + z2 & /z0 + /z4 & /z2 & z1 & z0;
z1 = z1 & /z0 + /z1 & z0;
z0 = /z0;

pl = z4 & /z3 & /z2 & z1 & /z0;
Dec_En = z3 + z2 + /z4 & z1 + z4 & /z1;
```

```
Pre_Code = /Ser_In & CLK & Dec_En + Ser_In & /CLK + Ser_In & /Dec_En;

*END
```

C.2 Synchronizer

A counter algorithm is used to synchronize the received data to the local clock. The principle is shown in section 5.4.4, thus only the text file to program the GAL is presented.

```
Syncronizer

*IDENTIFICATION Decoder;

*TYPE GAL20V8;

*PINS

% Input %
r = 3,

% Output %
/clr_res.r = 22,
z2.r = 21,
z1.r = 17,
z0.r = 16,
y.o = 15;

*BOOLEAN-EQUATIONS
z2 = /r & z2 + /r & z1;
z1 = /r & z0 & /z1 + /r & z2 & /z0 & z1;
z0 = /r & /z0 & /z1 + /r & z2 & /z0 & z1;
clr_res = r;

y = z0 & z1 + /z2 & z1;

*END
```